Politecnico di Torino

ScuDo
Scuola di Dottorato ~ Doctoral School
WHAT YOU ARE, TAKES YOU FAR

Doctoral Dissertation
Doctoral Program in Energy Department (35^{th}cycle)

Development of Innovative Methodologies to Support the Design of Connected and Electrified Vehicles

By

Luca Pulvirenti

******

Supervisor(s):
Prof. Luciano Rolando, Supervisor
Prof. Federico Millo, Co-Supervisor

Doctoral Examination Committee:
Prof. Nicolò Cavina, Università di Bologna
Prof. Giorgio Rizzoni, Ohio State University
Prof. Marcello Canova, Ohio State University
Prof. Daniela Misul, Politecnico di Torino
Prof. Robert Prucka, Clemson University

Politecnico di Torino
September 14, 2023

Declaration

I hereby declare that the contents of this dissertation constitute my own original work and do not compromise in any way the rights of third parties, including those relating to the security of personal data.

Luca Pulvirenti
September 14, 2023

* This dissertation is presented in partial fulfillment of the requirements for **Ph.D. degree** in the Graduate School of Politecnico di Torino (ScuDo).

To my parents

Abstract

In the context of a growing demand for sustainable transportation worldwide, Electrified Vehicles (xEVs) represent a valuable solution to improve efficiency and reduce pollutant emissions of the current vehicle fleet. In parallel with the electrification trend, the synergistic benefits provided by the growing vehicle connectivity level and the exploitation of Artificial Intelligence (AI) techniques may transform the transportation sector in several dimensions with important societal and economic impacts: reduced energy consumption, enhanced traffic flow, and improved road safety are among them. In this framework, it is essential to develop multidisciplinary techniques and algorithms that can assess the increased opportunities for energy-efficient driving with the deployment of connected and electrified vehicles. Therefore, this dissertation constitutes, by means of numerical simulation, a feasibility study on some innovative methodologies to support the design of these types of vehicles, by presenting two relevant case studies and the assessment of some innovative methodologies on them. The first case study is a plug-in Hybrid Electric Vehicle (pHEV): an extensive experimental campaign provided the data used to reverse engineer its control strategy and build its digital twin without having direct access to its EMS. The virtual test rig was then used to assess the theoretical benefits that the introduction of Vehicle-to-Everything (V2X) communication can have in terms of energy and time savings in a real-world route. The vehicle's digital twin was later used to assess the potentialities of an advanced energy management strategy that can exploit V2X information. The second case study is a state-of-the-art mid-size electric SUV: Battery Management System (BMS) data from daily driving were analyzed in order to generate on-the-fly Performance Indicators (PI), that can be easily extracted from real-world driving and charging events and linked to battery health. The results proved that the proposed approaches may be key enablers in supporting the development of connected and electrified vehicles.

Contents

List of Figures

List of Tables

List of Symbols

Acronyms

AI	Artificial Intelligence
AT	Automatic Transmission
A-V2X-ECMS	Adaptive V2X connectivity-based ECMS
AWD	All-Wheel Drive
BEV	Battery Electric Vehicle
BMEP	Brake Mean Effective Pressure
BMS	Battery Management Systems
BSFC	Brake Specific Fuel Consumption
CAN	Controller Area Network
CAV	Connected and Automated Vehicle
CD	Charge Depleting
CNN	Convolution Neural Network
CPU	Central Processing Unit
CS	Charge Sustaining
C-V2X	Cellular Vehicle-to-Everything
DC	Direct Current
DFN	Doyle-Fuller-Newman
DP	Dynamic Programming
DSRC	Dedicated Short Range Communications
DTV	Differential Thermal Voltammetry
DV	Differential Voltage
ECM	Equivalent Circuit Model
ECMS	Equivalent Consumption Minimization Strategy
ECU	Electronic Control Unit
EDS	Energy Dispersive Spectrometry

EIS	Electrochemical Impedance Spectroscopy
EM	Electric Machine
EMS	Energy Management System
EoL	End of Life
ESPM	Enhanced Single Particle Model
ETA	Expected Time of Arrival
FFT	Fast Fourier Transform
GHG	Greenhouse Gas
HEV	Hybrid Electric Vehicle
HPCU	Hybrid Power Control Unit
HPPC	Hybrid Pulse Power Characterization
HV	High Voltage
IC	Incremental Capacity
ICE	Internal Combustion Engine
ITS	Intelligent Transportation Systems
JRC	Joint Research Centre
K-NN	K-Nearest Neighbors
LAM	Loss of Active Material
LCO	Lithium Cobalt Oxide
LIB	Lithium-Ion Battery
LFP	Lithium iron -Fe- Phosphate
LLI	Loss of Lithium Inventory
LMO	Lithium Manganese Oxide
LPM	Load Point Moving
LSTM	Long Short-Term Memory
LV	Low Voltage
ML	Machine Learning
MPC	Model Predictive Control
NCA	Nickel Cobalt Aluminum oxide
NEDC	New European Driving Cycle
NMC	Nickel Manganese Cobalt oxide
NN	Neural Network
OBD	On-Board Diagnostic
OCP	Open Circuit Potential
OCV	Open Circuit Voltage
OCV	Optimal Operating Line
PCA	Principal Component Analysis

PDE	Partial Differential Equations
PEMS	Portable Emissions Measurement System
PI	Performance Indicator
PID	Proportional-Integral-Derivative
PM	Permanent Magnet
PMP	Pontryagin's Minimum Principle
P2D	Pseudo-Two-Dimensional
RB	Rule Based
RDE	Real Driving Emissions
ReLU	Rectified Linear Unit
RESS	Reversible Energy Storage System
RNN	Recurrent Neural Network
RT	Real-Time
RUL	Remaining Useful Life
SDP	Stochastic Dynamic Programming
SEI	Solid-Electrolyte-Interphase
SEM	Scanning Electron Microscopy
SPM	Single Particle Model
SoC	State of Charge
SoE	State of Energy
SoH	State of Health
SPaT	Signal Phase and Timing
TC	Torque Converter
V2I	Vehicle-to-Infrastructure
V2P	Vehicle-to-Pedestrian
V2V	Vehicle-to-Vehicle
V2X	Vehicle-to-Everything
VGDP	Variable Grid Dynamic Programming
WLTP	Worldwide Harmonized Light-duty vehicles Test Procedures
xEV	Electrified Vehicle
XRD	X-Ray Diffractometry

Definitions

Chapter 1

CO_2	Carbon Dioxide

Chapter 2

b	NN Bias Vector
b_i	LSTM Bias Vector
c_t	LSTM Cell State
C_6	Graphite
f	LSTM Forget Gate
$f(.)$	NN Activation Function
h_t	LSTM Output State
I	Current
i	LSTM Input Gate
MO_2	Metal Oxide
o	LSTM Output Gate
Q	Capacity
Q_n	Nominal Capacity
R	Resistance
R_i	LSTM Recurrent Weight
R_n	Nominal Resistance
$\sigma(.)$	LSTM Activation Function
t	Time
V	Voltage
x_i	NN Input
x_t	LSTM Input at time t
y	NN Output
W_i	LSTM Input Weight
w_i	NN Input Weight

Chapter 3

$f(.)$	Function
J	Cost Function
$H(.)$	Hamiltonian Function
$L(.)$	Instantaneous Cost
$G(.)$	Instantaneous Contraint
k	Discrete Time Index
m	Consumed Mass
$\dot{m}$	Instantaneous Mass Flow
$\dot{m}_{el}$	Electrical Istantaneous Fuel Consumption
$\dot{m}_{f,eq}$	Equivalent Istantaneous Fuel Consumption
$\dot{m}_f$	Engine Istantaneous Fuel Consumption
P_{batt}	Battery Power
Q_{LHV}	Fuel Lower Heating Value
s	Equivalence Factor
t	Time
t_0	Initial Time of the Optimization Horizon
t_f	Final Time of the Optimization Horizon
$\mathscr{U}$	Control Space
u	Control Variable
u_k	Discrete Control Variable
$\mathscr{X}$	State Space
x	State Variable
x_k	Discrete State Variable
λ	Co-state
μ	Sequence of Policies
π	Control Policy
$\phi(.)$	Terminal Cost
$\psi(.)$	Terminal Condition
Ω_x	Set of Admissible States
*	Relative to the Optimal Solution

Chapter 4

A_f	Vehicle Frontal Area
$a_{s,j}$	Specific Interfacial Surface Area
C	Capacitance
C_d	Aerodynamic Drag Coefficient
C_i	Coast-Down Coefficient
C_i	Lithium-ion Concentration
c_i	Rolling Resistance Coefficient
c_{roll}	Rolling Resistance Coefficient
$c_{s,j}$	Electrode Lithium-ion Concentration
$D_{e,j}^{eff}$	Electrolyte Phase Effective Diffusion Coefficient
$D_{s,j}$	Diffusion Coefficient
F	Faraday Constant
F_{aero}	Aerodynamic Resistance
F_{brk}	Braking Force
F_{grade}	Resistant Force due to Road Slope
$F_{inertia}$	Inertial Force
F_{pwt}	Tractive Force
F_{roll}	Rolling Resistance
g	Gravitational Acceleration
$j \in [p,n]$	Electrode
$i_{int,j}$	Intercalation Current
$\kappa_{D,j}^{eff}$	Diffusional Conductivity
κ_j^{eff}	Effective Ionic Conductivity
M_{veh}	Vehicle Mass
P_{elec}	Electrical Power
P_{loss}	Power Loss
P_{mech}	Mechanical Power
R	Resistance
R_j	Radius of the Spherical Particle
r	Radial Coordinate
t	Temporal Coordinate
t_0^+	Transference Number
v	Vehicle Speed
V	Voltage
V_{OC}	Open Circuit Voltage

c	Cartesian Coordinate
α	Road Slope Angle
η	Efficiency
ρ_{air}	Air Density
$\sigma_{eff,i}$	Effective Electronic Conductivity
$\phi_{s,j}$	Solid Phase Potential
$\phi_{e,j}$	Electrolyte Phase Potential

Chapter 1

Introduction

In the last decades, the risks connected to climate change and the depletion of natural resources have become strikingly evident and, as a consequence, public awareness concerning environmental issues has dramatically raised. Worldwide, policymakers have been brainstorming to define global frameworks and agreements to curb the current trend of increasing Greenhouse Gas (GHG) emissions and mitigate the detrimental effect of global warming. Focusing on Europe, the European Commission has pledged its commitment to this cause by adopting the European Green Deal: a proposal aimed at transforming the EU into a modern, resource-efficient, and competitive economy, ensuring, among the targets, zero net emissions of GHGs by 2050 [6]. In this framework, on July 14, 2021, the EC put forward the “Fit for 55" regulatory proposals intended to secure an EU economy-wide GHG reduction of at least 55% by 2030, compared to 1990 levels. Since transport is one of the most energy-intensive sectors (it accounts for 35% of the worldwide energy consumption [7]), one of the regulatory proposals lowers the current 2030 CO_2 targets, from -37.5% to -55% for new passenger cars and from -31% to -50% for new vans, both relative to 1990 levels. In addition, the proposal introduces an even more challenging target for new cars and vans starting from 2035: a 100% reduction of CO_2 emissions.

In the light-duty vehicle sector, electrified mobility solutions featuring Li-ion batteries represent the best option for automakers to achieve compliance with the current legislation targets. The joint effects of an increased offer along with the incentives and benefits provided for buying or owning an Electrified Vehicle (xEV) [8] have led to an unprecedented growth of xEV sales in the European market. The number of new xEVs registrations has seen a steady increase from 2010 to 2020 (from 600 to about 1.061.000 units - 11% of new registrations) but has surged in 2021

when it reached 18% of newly registered passenger cars [9], and kept rising in 2022 [10]. Similar trends can also be observed in the other two big world players, i.e., the United States and China, where new xEV registrations have more than doubled and nearly tripled in 2021, respectively [10].

Among the xEVs, the popularity of Battery Electric Vehicles (BEVs) is constantly on the rise, but substantial improvements are still needed in terms of performance, cost, and longevity for ensuring parity with conventional vehicles. The limited range of BEVs, as well as the long recharging times, and the inadequate infrastructure, still make Hybrid Electric Vehicles (HEVs) and plug-in Hybrid Electric Vehicles (pHEVs) the preferred solution in a mid-term scenario [11], since they can combine the desired features of an electric and a conventional powertrain. However, HEV fuel economy is highly dependent on the cooperation between the Internal Combustion Engine (ICE) and the Electric Machines (EMs) installed on board and the inappropriate energy management of the hybrid powertrain could jeopardize the benefits of powertrain electrification. The Energy Management System (EMS) is in charge of judicious control of the power actuators optimizing their power split [12], and computer-aided software tools, allowing the virtual simulation of the powertrain behavior, are widely adopted for energy optimization. A remarkable amount of research into EMS has been conducted over the last decades [13] and the current trend is towards the quest for finding real-time implementable and optimal strategies [3].

One critical need of all xEVs featuring Li-ion batteries is the accurate estimation of the State of Health (SoH) to forecast the battery lifetime and degradation under various operating conditions. This particularly rings true for BEVs, where the battery SoH strongly affects the available driving range but plays a pivotal role also in the energy management of HEVs and pHEVs since battery aging affects energy efficiency [14]. Thus, if available, battery SoH indicators could also be included in the cost function of the EMS in order to penalize actions that could undermine battery health. However, monitoring battery health in the field through the signals tracked by the Battery Management System (BMS) such as current, voltage, and temperature is a multifaceted challenge and remains an open research conundrum. Not to mention that the looming cobalt supply chain issues [15], the dependence on critical earth materials [16], and the immaturity of the recycling infrastructure [17] call for more emphasis on the judicious monitoring and usage of Li-ion batteries.

In parallel to the electrification trend, in recent years, research on vehicular networks and communications has received a great deal of attention globally, and several car companies and government institutions are making huge investments

in this area. In the frame of the Intelligent Transportation System (ITS) [18], the adoption of Connected and Automated Vehicles (CAVs) could lead to a major technological revolution in the mobility sector that can effectively enhance safety [19], traffic efficiency [20], and energy savings [21]. HEVs and pHEVs can benefit the most from embedding them in an ITS since the powertrain control system can gain access to relevant information on the future route and traffic conditions [22, 14]. Vehicle-to-Everything (V2X) communication along with cloud computing adoption [23] may enable a change of paradigm of the energy management problem: from an instantaneous optimization to globally minimizing it over the entire driver route by jointly optimizing the speed trajectory and powertrain torque split [24].

Finally, in the midst of the so-called "Intelligence Revolution" [25], which is deeply remodeling the fabric of our society, Artificial intelligence (AI) could not leave untouched research in xEVs. The sharp increase in CPU processing capacity, in addition to the possibility of scaling up computations on cloud platforms, has led to increasing interest in the exploitation of Machine Learning (ML) techniques for the development of energy control strategies for HEVs [3]. Thanks to their ability to recognize high dimensional patterns in data, ML-based models have also shown success in predicting battery lifetime under various operating conditions [26], thus there has been plenty of research in devising models blending physical and data-inspired algorithms [27].

In this framework, it is essential to develop multidisciplinary techniques and algorithms that can assess the increased opportunities for energy-efficient driving with the deployment of connected and electrified vehicles. This dissertation constitutes a feasibility study on some innovative methodologies to support the design of these types of vehicles. Considering the complexity and vastness of this topic, this dissertation does not have the presumption to provide a comprehensive methodology taking into account all the possible facets but will try to provide an exhaustive overview of the state-of-the-art methodologies available in the literature along with the description of the technical details. Then, this work will show two relevant case studies and the assessment of some innovative methodologies on them.

The remainder of the dissertation is structured as follows:

- Chapter 2 provides a comprehensive overview of the theoretical background, by describing xEVs and how they can be classified, the operating principles and the aging of Li-ion batteries, the most common machine learning algorithms, and the main pillars of an ITS;

- Chapter 3 introduces the role and main features of energy management in HEVs. It formalizes the problem using optimal control theory and describes the most adopted model-based optimization techniques for the energy management of HEVs. Finally, the current trend is described providing some hints about future trends;

- Chapter 4 examines the numerical modeling of an xEV. The approaches for modeling a vehicle at a system level are described, followed by the typical approaches adopted for modeling the single components, i.e., ICE, EM, and Li-ion battery, giving particular emphasis to the latter;

- Chapter 5 presents the first case study on which some innovative methodologies for the energy management of HEVs are tested. The data gathered from an extensive experimental campaign performed on a commercially available pHEV are used to reverse engineer its control strategy and build a virtual test rig without having direct access to its EMS. The virtual test rig is then used to assess the theoretical benefits that the introduction of V2V and V2I communication can have in terms of energy and time savings in a real-world route. The vehicle digital twin is employed to assess the potentialities of an innovative Adaptive Equivalent Consumption Minimization Strategy (A-ECMS) algorithm: a Long Short-Term Memory (LSTM) deep learning model finds the optimal equivalence factor depending on information about the future vehicle driving patterns;

- Chapter 6 presents the second case study: BMS data from daily driving of an e-SUV are analyzed in order to generate on-the-fly Performance Indicators (PI), that can be linked to battery health and can be easily extracted from real-world driving and charging events. These indicators rely on simple mathematical operations, which are computationally inexpensive and easily implementable on a BMS, and can be used as features for ML models to complement current BMS strategies;

- Finally, Chapter 7 summarizes the conclusions, future work, and the intellectual merits of this dissertation.

Chapter 2

Theoretical Background

2.1 Electrified Vehicles

2.1.1 Introduction

Electrified Vehicles (xEVs) refer to a range of technologies that use electricity to propel a vehicle, replacing the components, that usually operate on a conventional energy source, with components that operate on electricity. In general, vehicle electrification refers to the powertrain and its auxiliary systems such as on-board and off-board charging systems, as well as wireless power transfer. Many other vehicle functionalities may be affected by electrification, such as power-assisted steering, stability program, traction control, light system, suspension, and more. In a Battery Electric Vehicle (BEV) the ICE is replaced by one or more Electric Machines (EMs) powered by a lithium-ion battery. Due to limited range, long recharging times, and inadequate infrastructure, it is challenging to completely replace a conventional powertrain with an electric one while still meeting all consumer demands [11]. Not to mention that, on the basis of the current electricity supply infrastructure and operation, widespread adoption of BEVs will not lead to a substantial positive impact on GHG emissions [28].

Hybrid Electric Vehicles (HEVs), combining the desired features of electric and conventional powertrains, may be the preferred solution, at least in a mid-term scenario. Thanks to the high energy density of fossil fuels, the ICE can guarantee long-range capability, while the introduced ancillary energy reservoir can help share the load with the ICE, shifting the engine working points towards more efficient or

less polluting areas. Moreover, in HEVs, the ICE can be shut down when not needed, and, with reference to a conventional vehicle, a smaller and less powerful engine can be coupled to the EMs to improve the fuel economy ("downsizing") without compromising on performance. The vehicle kinetic energy dissipated during braking can be partly recovered: the EMs can work as generators, recovering the kinetic energy and converting it into electricity to be stored in the battery ("regenerative braking").

2.1.2 Classification

Between a conventional vehicle, where no electrification is present (apart from the low-voltage battery) and only the ICE can deliver the power requested by the driver, and the BEV different levels exist. A classification of xEVs based on the sizes of the actuators is proposed in Figure 2.1. The bigger the EMs and battery sizes, the higher the level of electrification. In a conventional vehicle, no electrification is present (apart from the low-voltage battery): only the ICE can deliver the power requested by the driver. Micro Hybrids feature a small EM that can shut down and restart the ICE (reducing fuel consumption and emissions at idle). Mild hybrids and full hybrids feature bigger EM and battery allowing further advantages, such as regenerative braking and engine assist. In plug-in Hybrid Electric Vehicles (pHEVs), differently from HEVs, the battery can also be recharged by an external electric power source: they feature a bigger battery size that is usually designed for allowing the vehicle to travel long distances with little or no help from the ICE. Finally, electric vehicles can only rely on the EMs to deliver the power requested by the driver. The EM can be powered by a fuel cell or a battery.

HEVs can also be classified according to their powertrain architecture. The following three main categories can be identified:

- Series Hybrid:
  Only the EMs are physically connected to the wheels, and the traction motor is powered by a battery pack and/or a generator run by the ICE;
- Parallel Hybrid:
  Both the ICE and the traction motor can supply their mechanical power to the driven wheels, and the connection between ICE and EM is obtained by means of a gear set, a chain, a belt, or a clutch;

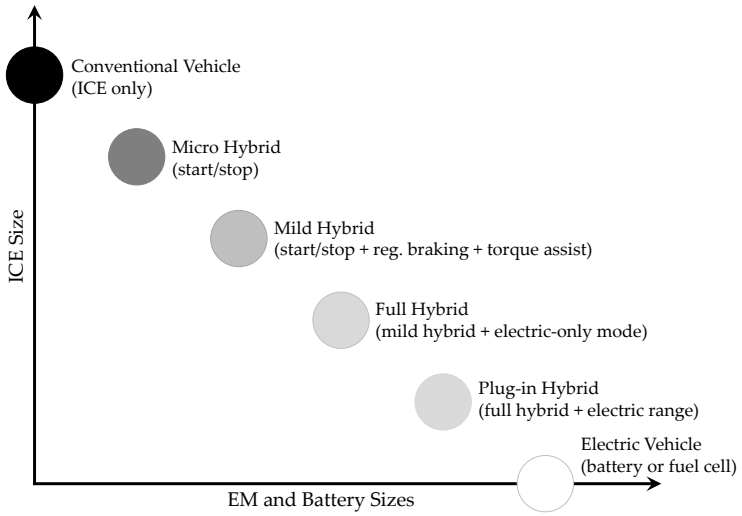

Fig. 2.1 Spectrum of vehicle electrification levels.

- Complex Hybrid:
  This architecture is characterized by the coexistence of a parallel path with a series one.

2.2 Electrochemical Batteries

2.2.1 Introduction

As already explained in Section 2.1, xEVs feature an electrochemical battery, i.e., an energy storage device that converts the chemical energy contained in the active materials directly into electrical energy. Lithium-Ion Batteries (LIBs) are the most common technology adopted as a Reversible Energy Storage System (RESS), thus particular emphasis will be given to them. Since first developed by Dr. John Goodenough et al. [29] and then commercialized by Sony in 1981 [30], they have played a key role in the field of consumer electronics devices, but, in the last decade, they also have become crucial in the electrification of conventional vehicles, thanks to their high energy and power densities, good efficiency, and long lifespan. While the term battery is often used inappropriately, it is important to note that the basic electrochemical unit is a cell. Cells are then electrically connected in series and/or parallel to compose a battery system. An electronic control unit, known as the Battery Management System (BMS), is connected to the battery system and is responsible

for the safe and reliable operation of the battery. It controls that the battery operates within specified voltage and current limits, prevents over-charging, over-discharging, and over-heating, performs cell balancing, and improves battery safety [31]. To optimize battery performance and prolong useful life, the BMS needs an accurate estimation of the battery State of Charge (SoC) and State of Health (SoH).

2.2.2 Operating Principles

As shown in Figure 2.2, a lithium-ion cell consists of five components, namely negative electrode (anode), positive electrode (cathode), electrolyte, separator, and current collectors. The separator is inserted between the two electrodes, while the whole cell is soaked with a liquid electrolyte in which lithium ions can be transported. The electrodes have porous structures to enlarge the surface area and reduce the diffusion distances [32].

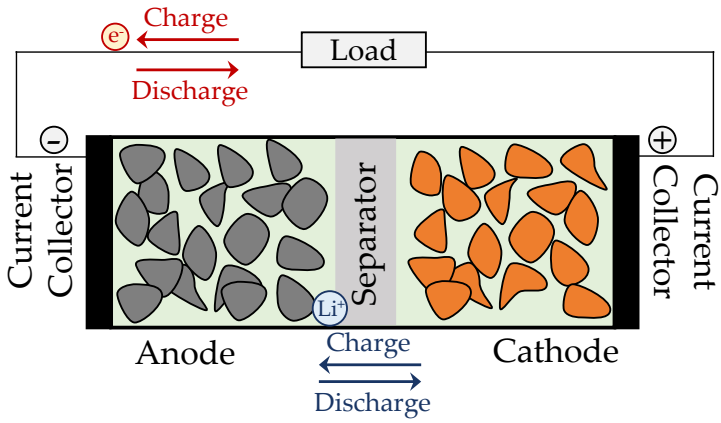

Fig. 2.2 Schematic diagram of a lithium-ion cell.

The lithium-ion cell is powered by redox reactions occurring at the surface of the electrodes resulting in a mechanism known as insertion or intercalation: this refers to a reversible reaction that includes a molecule between two other molecules. During discharge, the lithium ions are extracted from the anode and inserted into the cathode. More precisely, lithium atoms at the surface of the anode give up electrons - collected by the current collectors and conducted through the external circuit - and become positive lithium ions, Li^+, which dissolve into the electrolyte. Conversely, positive lithium ions close to the surface of the cathode receive the electrons coming from the external circuit, becoming charge-neutral lithium atoms that enter the crystal

structure of the cathode. Supposing that the active material in the cathode is a generic metal oxide (MO_2), the reactions taking place are:

$$Li_yC_6 \rightleftharpoons C_6 + yLi^+ ye^- \tag{2.1}$$

$$Li_{1-y}MO_2 + yLi^+ + ye^- \rightleftharpoons LiMO_2 \tag{2.2}$$

where Equation (2.1) is the anodic half-reaction and Equation (2.2) is the cathodic half-reaction. During charge, the process is reversed; thus, lithium ions pass back and forth between the electrodes during charging and discharging [33]. Presently, the vast majority of commercial lithium-ion cells use some form of graphite (LiC6) for the anode material, although lithium titanate and silicon have been used too [34]. There is much more variability in the choice of the metal oxides that are commonly used in cathodes. They can be classified into three groups based on their structure [35]:

- Ordered rock-salt, such as Lithium Cobalt Oxide (LCO), Nickel Cobalt Aluminum oxide (NCA), and Nickel Manganese Cobalt oxide (NMC);
- Spinel, such as Lithium Manganese Oxide (LMO);
- Olivine, such as Lithium iron -Fe- Phosphate (LFP).

A detailed comparison of the material properties of the different cathode materials can be found in [36, 37], while a summary of each cell chemistry's performance and specifications is given in [38]. Regarding the current collectors, copper and aluminum foils are typically used for anode and cathode, respectively.

A fundamental component of the controller for a vehicle featuring a Lithium-Ion Battery (LIB) is an algorithm that provides an estimate of the battery State of Charge (SoC), i.e., the available capacity (Q) expressed as a percentage of the nominal capacity (Q_n). In real-world applications, however, it is difficult to directly measure the battery SoC because of the complicated electrochemical reactions and the strong coupling characteristics. The most common approach to estimate the SoC is Coulomb counting which integrates the current (I) measurement, according to the following:

$$SoC(t) = SoC(t_0) + \int_{t_0}^{t} \frac{I(t)}{Q_n}\, dt \tag{2.3}$$

where Q_n is the nominal capacity, $SoC(t)$ and $SoC(t_0)$ are the SoC values at the time t and the initial instant t_0, respectively. In real-world applications, however, the noise affecting the current measurement and the variation of battery capacity under different aging levels may make Coulomb counting inaccurate. Therefore, the accurate estimation of the SoC in real-time is critical functionality for a BMS, which is attracting considerable research efforts, and a plethora of different techniques have been proposed in the literature [39] [40].

2.2.3 Aging Mechanisms

Degradation of the cells of a LIB is the result of a complex interplay of unwanted chemical side reactions and physical changes to the active materials. Aging is generally irreversible and eventually results in cell failure. Figure 2.3 illustrates some of the most commonly reported degradation mechanisms in Li-ion cells.

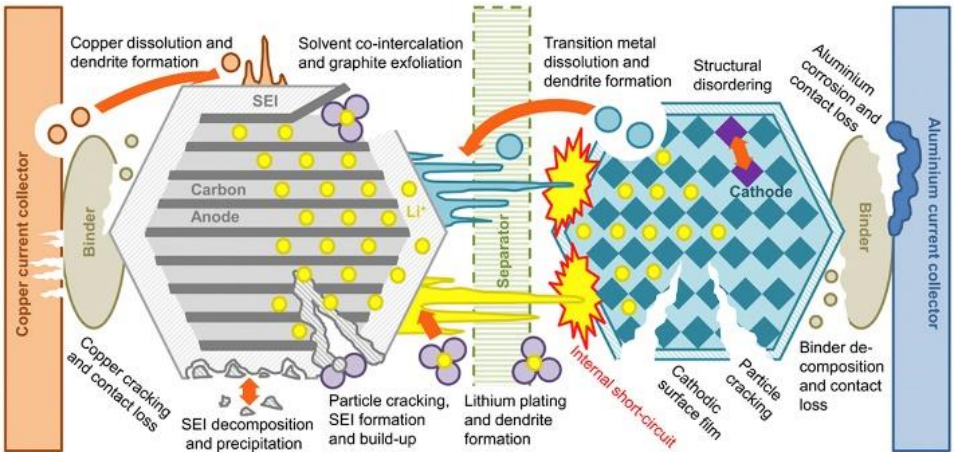

Fig. 2.3 Degradation mechanisms in Li-ion cells [1].

Degradation depends on a variety of aging mechanisms caused by different intrinsic and extrinsic factors [41, 42]. Inconsistencies in manufacturing procedures and in the materials used are intrinsic problems, however, they are now being reduced by advancements in quality control, production procedures, and battery designs. Extrinsic factors include inhomogeneous operating conditions, e.g., non-uniform current or temperature distribution within the battery pack. The most important aging effects occurring in LIBs are usually measured in terms of:

- Capacity fade:
  it refers to the loss in discharge capacity that a battery demonstrates over time (related to available driving range);

- Power fade:
  it is the decrease of the power capability caused by an increase in the internal resistance/impedance of the cell (related to available power).

LIB degradation presents a major concern in long-term, reliable applications, including xEVs, where long cycle life under demanding duty schemes is required. Indeed, different degradation phenomena in LIBs lead to different aging patterns and failure modes [43].

There are many different aging mechanisms that are commonly grouped into four different degradation modes:

- Loss of Lithium Inventory (LLI):
  Lithium ions are lost in parasitic reactions, such as surface film formation - e.g., growth of the Solid-Electrolyte-Interphase (SEI) - decomposition reactions, lithium plating, etc. [44]. LLI generally leads to direct capacity fade, but surface films may also cause power fade [1];

- Loss of Active Material (LAM) in the anode:
  Particle cracking, loss of electrical contact, and blocking of active sites by resistive surface layers make the active material in the anode no longer available for the insertion of lithium. This leads to both capacity and power fade [1];

- LAM in the cathode:
  Structural disordering, particle cracking, and loss of electrical contact make the active material in the cathode no longer available for the insertion of lithium. These processes can lead to both capacity and power fade [1];

- Conductivity Loss
  Degradation of the electronic parts of the battery such as current collector corrosion or binder decomposition leads to conductivity loss [45].

Figure 2.4 provides a more comprehensive list of degradation mechanisms, their causes, effects, and links to degradation modes. Within the literature, several techniques have been reported to identify and quantify the effects of degradation modes. These are often classified into in-situ and ex-situ electrochemical techniques [41]. The in-situ techniques are not-invasive, potentially suitable for real-time applications within a BMS. Some examples are Incremental Capacity (IC) and Differential Voltage (DV) [44, 46, 47], Electrochemical Impedance Spectroscopy (EIS) [48], and

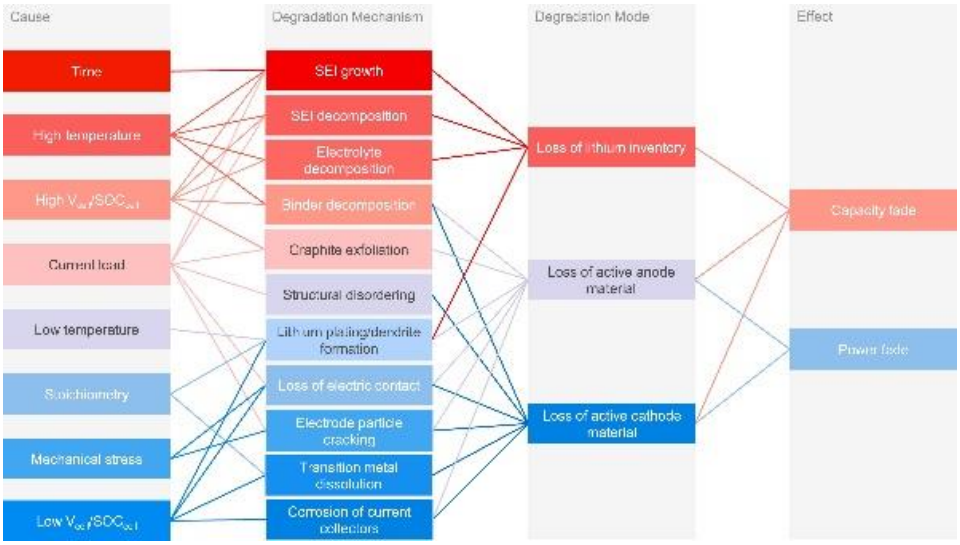

Fig. 2.4 Cause and effect of degradation mechanisms and associated degradation modes [1].

Differential Thermal Voltammetry (DTV) [49]. Ex-situ methods, on the contrary, study the cells internally by applying physicochemical and electrochemical invasive techniques. Some examples are Scanning Electron Microscopy (SEM), Energy Dispersive Spectrometry (EDS), and X-Ray Diffractometry (XRD) [50].

Incremental Capacity and Differential Voltage

DV and IC methods are used to identify and quantify changes in the electrochemical properties of the cell from changes in the capacity or cell voltage. The DV curve is computed as the derivative of V with respect to the charged or discharged capacity Q and is defined as follows:

$$DV = \frac{dV}{dQ} \tag{2.4}$$

The IC curve is defined as the inverse of Equation (2.4), i.e.,

$$IC = \frac{1}{DV} = \frac{dQ}{dV} \tag{2.5}$$

The coexistence of phases in positive and negative electrodes leads to constant chemical potentials resulting in a flat anode or cathode Open Circuit Potential (OCP) [51] [52]. This information can be obtained from the cell Open Circuit Voltage (OCV) since it derives from subtracting the OCP of the negative electrode from

the positive one. IC and DV methods allow the transformation of the cell voltage plateaus, corresponding to two-phase material regions, into valleys and peaks in DV and IC curves, respectively [53]. Since the IC curve computes the evolution of cell voltage versus capacity, voltage plateaus result in large capacity increments (dQ), which lead to the formation of peaks in the IC curve and valleys in the DV curves.

A change in the IC-DV curves can be correlated with the most pertinent aging mechanisms as suggested by [44]. Conductivity loss causes a shift of the curves toward lower voltages (IC) and constant capacity (DV); LLI causes both a decrease in the height of the peaks and a shift toward lower or higher voltages (IC) and a shift toward lower capacities (DV); LAM causes a decrease of the height of the peaks (IC) and a decrease of the depth of the valleys (DV) [44]. Since the shifting of the IC and DV curves can be correlated to battery health, these techniques have been extensively investigated in the literature to identify [47] and quantify [54] aging. According to [55], the height and the position of the peaks in the IC curves are also affected by temperature.

2.2.4 State of Health

One of the critical tasks of the BMS is monitoring the State of Health (SoH) of the LIB to enforce safe operating bounds and enable health-conscious control strategies. The SoH of a battery is a figure of merit to quantitatively assess the level of battery aging, but it is not directly measurable and still lacks a holistic definition. Two common definitions are conventionally used, in terms of capacity fade:

$$SoH = \frac{Q}{Q_n} \tag{2.6}$$

or in terms of internal resistance fade:

$$SoH = \frac{R - R_n}{R_n} \tag{2.7}$$

where Q and Q_n denote the actual and nominal capacity values, respectively, and R and R_n denote the actual and rated internal resistances, respectively. In automotive applications, the End of Life (EoL) is often specified as the point where measured capacity reaches 80% of the pristine cell capacity and/or the internal resistance reaches an increase of 100% (always with reference to the pristine cell resistance).

In a laboratory setting, which is the most investigated in the literature, battery aging tests are performed in well-controlled environments and the actual battery capacity or internal resistance can be periodically measured with high-accuracy instruments to assess the 'ground truth' battery health [39]. However, standardized test procedures conducted under laboratory conditions cannot reproduce what batteries actually experience in real-world applications. They do not take into account the variability induced in terms of electrochemical, thermal, and aging behavior between cells in a battery pack. Moreover, field data from real-world scenarios exhibit varying operating conditions, irregular cycling patterns, and path-dependent degradation mechanisms, making reliable predictions difficult. This makes the prediction of the Remaining Useful Life (RUL) even more challenging. In the field, future health should be inferred from partial charge/discharge cycles and the corresponding signals tracked by the BMS such as current, voltage, and temperature [56].

The most common health forecasting approaches are based on Physics-Based (PB) models (see Section 4.5.1) that compute the evolution of the internal states of the battery under an expected load and environment. While PB models can capture accurately the electrochemical cycling behavior, they have limited applicability for health forecasting. Recently, data-driven and Machine Learning (ML) - based models (see Section 4.5.2) have shown success in predicting the RUL of Li-ion cells under various load conditions. ML models operate by recognizing patterns in high-dimensional databases and are agnostic to the underlying physical processes but lack transferability to situations far beyond the available data on which they were trained [27].

Hybrid Pulse Power Characterization Test

Among the laboratory reference performance tests, the Hybrid Pulse Power Characterization (HPPC) Test is used for determining the dynamic power capability over the device's usable voltage range using a test profile that incorporates both discharge and charge current pulses [57]. The pulses must be sufficiently short to avoid heat generation and/or change of SoC. The voltage response curve corresponding to the change in current can be measured and used to compute the ohmic cell (high-frequency) resistance, by means of their fraction:

$$R = \frac{V(t_2) - V(t_1)}{I(t_2) - I(t_1)} = \frac{\Delta V}{\Delta I} \tag{2.8}$$

where $V(t_1)$ and $I(t_1)$ are the voltage and current values at the beginning of the pulse, $V(t_2)$ and $I(t_2)$ at the end of it. Since the voltage profile of the cell changes with the aging, by repeating the test at different stages of the cell life, the high-frequency resistance can be used to assess its aging [58]. However, laboratory tests (such as the HPPC) can only have limited validity for real-life applications since they require an ad hoc current profile and conditions far from what the battery experiences under real operation in an xEV.

2.3 Artificial Intelligence

2.3.1 Introduction

In recent years, the sharp increase in Central Processing Unit (CPU) processing capacity, in addition to the possibility of scaling up computations on cloud platforms, has led to increasing interest in the exploitation of Artificial Intelligence (AI) in the energy management of HEVs, and in predicting the RUL of Li-ion cells. AI lacks an agreed-upon definition, but an appropriate one could be the following:

> *"Artificial Intelligence is that activity devoted to making machines intelligent, and intelligence is that quality that enables an entity to function appropriately and with foresight in its environment" [59].*

Since first introduced for checkers playing by [60], Machine Learning (ML) has become a very important area of AI. In line with general scientific reasoning, most ML methods are based on inductive inferences, i.e., they construct hypotheses from data. Deductive inferences follow necessarily and logically from their premises, whereas inductive ones are hypotheses, which are always subject to falsification by additional data. This distinction can be better clarified by means of the following classical example: if a large set of data contains only instances of white swans and no instances of black swans, then an ML algorithm might make the inductive inference that all swans are white. This inference may be wrong because there may still be an undiscovered island of black swans. However, inductive inferences, based on large amounts of data, are extremely useful. This particularly rings true with the current abundance of data availability in all fields.

2.3.2 Classification

There is a considerable number of approaches that can be included in the ML family, and according to data scientists, there is no single one-size-fits-all type of algorithm that is best to solve a problem. The best-suited algorithm depends on the kind of problem to be solved, the number of variables, etc. Several classifications can be done among the ML techniques [61], but a commonly accepted classification can be outlined by identifying three general families [62]:

- Supervised Learning:
  These algorithms infer a function that maps an input (independent variables) to an output (dependent variable) based on labeled training data. The input dataset is usually divided into train and test datasets, and the algorithm must learn some kind of patterns from the training dataset and apply them to the test dataset for prediction or classification. Some examples of supervised learning are Regression, Decision Trees, Random Forests, K-Nearest Neighbors (K-NN), Logistic Regression, etc.;

- Unsupervised Learning:
  These algorithms infer hidden patterns or intrinsic structures from unlabeled data. Unlike supervised learning, there are no correct answers because there are no labeled training data. Some examples of unsupervised learning are K-Means Clustering, Apriori algorithm, etc.;

- Reinforcement Learning:
  In Reinforcement Learning (RL) a computer program interacts with an environment where it must perform a certain goal. The program receives feedback in terms of a numerical reward signal as it navigates its problem space: it must learn to maximize the reward signal. The learner is not told which actions to take but instead must discover which actions yield the most reward by trying them.

2.3.3 Neural Networks

Among the ML techniques, in the last decades Neural Networks (NNs) have received a great deal of attention because many papers have proved their capabilities to solve a variety of problems [63] (e.g., pattern recognition, clustering, classification, etc.,), including the energy management of HEVs [64–66].

NNs are inspired by and resemble the human nervous system and the structure of the brain. The primary building block of a NN is the artificial neuron, or perceptron (depicted in Figure 2.5) [67], which takes several binary inputs, x_1, x_2, ..., x_N and produces a single binary output, y, according to:

$$y = f(w_i * x_i + b) \tag{2.9}$$

where x and y are the inputs and the output, respectively; w are the weights of the inputs; b is the bias vector; $f(.)$ is the activation function.

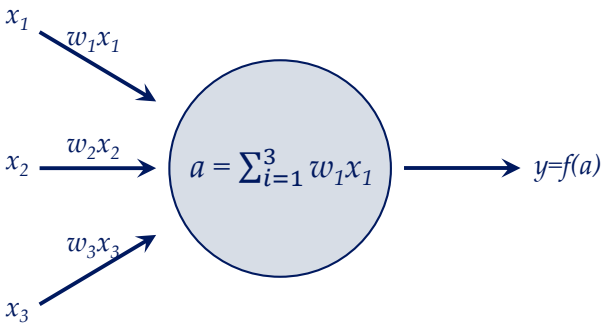

Fig. 2.5 Perceptron layout.

The nodes or units in each layer are connected to nodes in adjacent layers. Each connection has a weight value. The inputs are multiplied by the respective weights and summed at each unit. The sum then undergoes a transformation based on the activation function, which could be a sigmoid function, a hyperbolic tangent, or a Rectified Linear Unit (ReLU). During the training of the NN, the weights and the bias are automatically adjusted to learn a highly nonlinear input/output relationship by minimizing the actual and the predicted output patterns of a training set [68]. Deep Neural Networks (DNNs) are modeled as multilayer perceptrons, consisting of a higher or deeper number of processing layers. A breakthrough in DNNs occurred with the advent of the back-propagation learning algorithm. It was proposed in the 1970s [69] but it wasn't until the mid-1980s [70] that it was fully understood and applied to NNs. Self-directed learning was made possible with a deeper understanding and application of the back-propagation algorithm. The shift from shallow to deep learning has allowed for more complex and non-linear functions to be mapped, as they cannot be efficiently mapped with shallow architectures. This improvement has been complemented by the proliferation of cheaper high-performance Graphic Processing Units (GPU) and large volumes of datasets to use for training.

2.3.4 Long Short-Term Memory Networks

Among the deep learning techniques, i.e., Deep Neural Networks (DNNs), Convolution Neural Networks (CNNs), and Recurrent Neural Networks (RNNs), the latter can deal with temporal information of input data, thus can capture the hidden correlations between speed values. Specifically, RNNs architecture can update the current state based on the feedback of both the current input data and the past states (the so-called "short-term memory) [71]. However, when dealing with a large gap between the relevant input data, the error signals "flowing backward in time" tend to either blow up or vanish. To overcome these error back-flow problems, and correctly handle the so-called "long-term dependency", in 1997 Hochreiter and Schmidhuber proposed the Long Short-Term Memory (LSTM) layer [72]. Since they were first introduced, LSTMs have been modified and used by many researchers for numerous purposes [73, 74], including the energy management of HEVs [71]. Among the several changes leading to the layout of the layer adopted in this work, it is worth mentioning the introduction of gate f [75], which partially solves the gradient-vanishing problem typical of RNNs by discarding or keeping the information in the cell state.

Figure 2.6 shows a schematic of the standard LSTM cell. At time step t, the block uses the current state of the network (c_{t-1}, h_{t-1}) and the following input of the sequence to compute the output and update the cell state c_t. The layer adds or removes information from the cell state through the gates: i, f, and o denote input, forget, and output gates, respectively, while g denotes the cell candidate. Based on the connections shown in Figure 2.6, the LSTM cell can be mathematically expressed as:

$$\begin{cases} i_t = \sigma_g(W_i x_t + R_i h_{t-1} + b_i) \\ f_t = \sigma_g(W_f x_t + R_f h_{t-1} + b_f) \\ g_t = \sigma_c(W_g x_t + R_g h_{t-1} + b_g) \\ o_t = \sigma_g(W_o x_t + R_o h_{t-1} + b_o) \\ c_t = f_t c_{t-1} + i_t g_t \\ h_t = o_t \sigma_c(c_t) \end{cases} \tag{2.10}$$

where x_t is the input at time step t, c_t is the cell state, containing information from the previous time steps, h_t is the output state (also known as the hidden state),

W R, and b are the input weights, the recurrent weights, and the bias, respectively, and $\sigma(.)$ is the activation function.

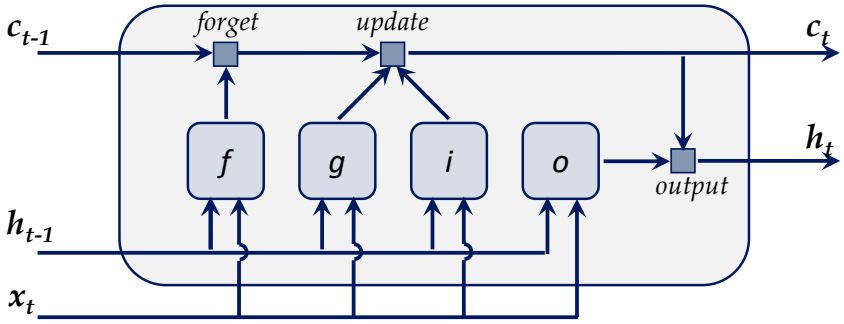

Fig. 2.6 LSTM layer layout: the predicted output patterns are assigned to the training set (the observations).

2.4 Connected xEVs

2.4.1 Intelligent Transportation System

An Intelligent Transportation System (ITS) [18] is a system, in the field of road transport, in which information and communication technologies can be easily exchanged. In the frame of an ITS, Vehicle-to-Everything (V2X) connectivity is one of its main pillars. V2X embraces all vehicle's connected communications: the on-board communication tools are used to deliver real-time traffic information so that the vehicle can proactively react to changing road conditions, recognize road signs and warnings, and more. Such communication can effectively enhance safety, traffic efficiency, and energy saving. For instance, the driver could be warned of potential hazards on the road and of issues with the vehicle itself. Moreover, by having access to the internet and/or to a wireless local area network, connected cars can get information from smartphones or, more generally, from Internet of Things (IoT) devices, constantly updating the driver. V2X incorporates the following more specific types of communication:

- Vehicle-to-Vehicle (V2V):
  These technologies transmit data between vehicles to enable applications that can warn drivers about potential collisions. Specifically, V2V-equipped cars

would emit data on their speed, position, heading, acceleration, size, brake status, and other useful data.

- Vehicle-to-Infrastructure (V2I):
  These technologies transmit data between vehicles and the road infrastructure to enable a variety of safety, mobility, and environmental applications. V2I applications are designed to avoid or mitigate vehicle crashes, particularly those crash scenarios not addressed by V2V alone, as well as to provide mobility and environmental benefits. Some potential safety applications of V2I are red light violation warnings, curve speed warnings, stop sign gap assist, reduced speed zone warnings, spot weather information warnings, etc. [76]

- Vehicle-to-Pedestrian (V2P):
  These technologies transmit data between vehicles and pedestrians to enable onboard safety monitoring tools and communication with a pedestrian's mobile device to avoid accidents. This could include people walking, riding bicycles, and entering/exiting mass transit vehicles.

Toyota was the pioneer in this field. In 2016, it became the first automaker to introduce automobiles equipped with V2X, which were only for sale in Japan. GM followed suit a year later: in the US, it introduced a Cadillac model also equipped with V2X. In 2019, Volkswagen presented the latest Golf generation: according to VW, the Golf was the first Volkswagen to offer V2X communication as standard in a mass-market model [77].

Two main standards are available for V2X communication. The first one is a set of radio standards based on the IEEE 802.11p technology and is referred to as Dedicated Short Range Communications (DSRC) [78]. The other standard is based on communication using cellular technologies [79]. The 3GPP developed the first Cellular V2X (C-V2X) standards based on the 4G mobile network [80]. The C-V2X potentiality could be further boosted by a possible coupling with the new 5G mobile network [81] or joint use of DSRC and C-V2X communication [82].

2.4.2 Connected Vehicle Control

The ability of connected vehicles to anticipate and predict possible future scenarios opens the door to energy-efficient control approaches. Information from connected

vehicles can be used to improve the energy efficiency of a vehicle at two different levels [83]:

- Route optimization:
  When a driver needs to move from a starting point A to a final point B, she/he usually chooses the shortest travel distance or the fastest travel time route. Apart from some recent exceptions [84], the same goes for most navigation systems. However, this is not always the most energy-efficient route because the shortest route may be congested, while the fastest route may be longer and contain segments with higher speed limits. Hence, V2X information could play a pivotal role in shifting from time-efficient driving to an energy-efficient one;

- Eco-driving:
  Once the most energy-efficient has been chosen, several speed profiles can be chosen on the selected route. The optimal speed profile, in terms of energy efficiency, is a constant speed: by reducing the occurrences and the intensity of the acceleration phases, the energy demand can be reduced. However, this is usually impossible to observe in real traffic conditions, especially in an urban environment with traffic light signals, road congestion, pedestrians, cyclists, road grade, different speed limits, etc. Also in this case, V2X information can be used to predict the traffic evolution over the defined route and deduce accordingly a vehicle speed profile as smooth and energy-efficient as possible. For instance, as a vehicle approaches a signalized intersection, with V2X technology it can access the Signal Phase and Timing (SPaT) of traffic lights (i.e., information about the location of the intersection and the number of seconds to switch from green to red light). With this information, the vehicle can use the current distance from the intersection and SPaT of traffic lights to calculate a vehicle speed profile that allows for avoiding unnecessary halts or slows at traffic lights. Quite recently, data-driven techniques, such as MPC [85] or RL algorithms [86, 87], have also been used to solve the eco-driving problem.

Chapter 3

Energy Management of HEVs

3.1 Introduction

In an ICE-equipped vehicle, the driver decides, through the accelerator and brake pedals, the instantaneous power delivery; then, a low-level controller, i.e., the Electronic Control Unit (ECU), converts her/his request into an amount of injected fuel. On the other hand, in an HEV, an ICE is combined with one or more EMs, and an additional control layer, namely the Energy Management System (EMS) and shown in Figure 3.1, decides the instantaneous power split between the actuators. Due to the increased complexity of an electrified powertrain, the benefits provided by hybridization can be jeopardized by not optimizing the cooperation between the power actuators. The scope of the energy management control strategy depends on the specific application: the strategy is usually focused on fuel economy, but its objective could also include other parameters, e.g., pollutant emissions, power delivery, etc. [88, 89].

3.2 Optimal Control Problem

Energy management in an HEV is an implementation of optimal control: the branch of control theory that deals with finding a control law for a given system such that an objective function is optimized. Optimal control means that the searched control law must achieve the best performance and respect the dynamics of the system where optimality is usually defined according to a performance index. For HEVs, the control law is represented by the instantaneous power split between the energy

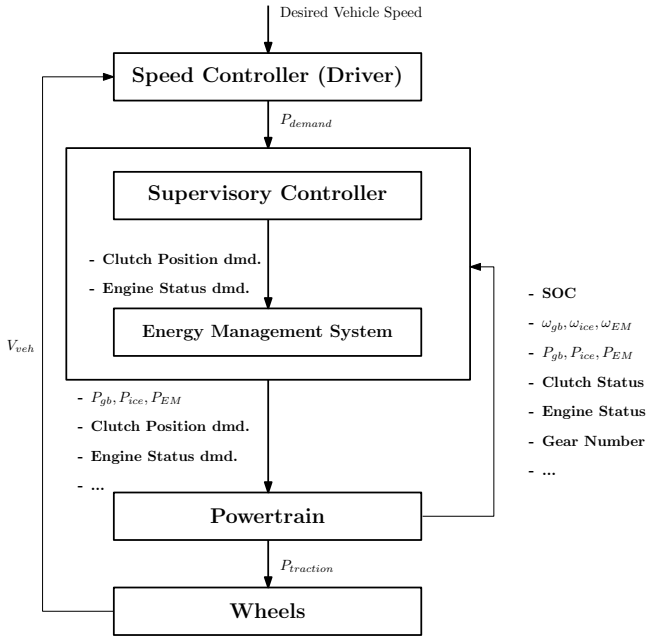

Fig. 3.1 The role of energy management system in a hybrid electric vehicle.

sources, and the performance index J_f can be the total fuel consumption, the total pollution emission, or any other meaningful cost function (or performance index) over the entire driving cycle.

The traditional optimal control techniques can only be used with simple mathematical models, and require a perfect knowledge of the entire optimization horizon, i.e., the time frame over which the optimization is defined. As these two conditions are not normally met by real systems, optimal control implementation in a physical domain whose future is unknown, is necessarily sub-optimal, i.e., imperfect. In formal terms [90, 91], an HEV can be considered as a dynamical system with the state equation:

$$\dot{x}(t) = f\left(x(t), u(t), t\right) \tag{3.1}$$

where $x(t) \in \mathbb{R}^n$ is the state variables vector, $u(t) \in \mathbb{R}^m$ is the control variables vector, f is a function that describes the system, and t is the time variable. Considering an optimal control problem that has a fixed final time and a partially constrained final state, the control law $u(t) : [t_0, t_f] \in \mathbb{R}^m$ is optimal if it minimizes, in the time interval $t \in [t_0, t_f]$, the cost function:

$$J = \phi\left(x(t_f), t_f\right) + \int_{t_0}^{t_f} L\left(x(t), u(t), t\right) dt \tag{3.2}$$

under the terminal conditions (boundary conditions on the state):

$$\psi\left(x(t_f),t_f\right)=0 \tag{3.3}$$

where $L(x(t),u(t),t)\in\mathbb{R}$ is the instantaneous cost function, and $\phi\left(x(t_f),t_f\right)\in\mathbb{R}$ is the terminal cost incurred at the end of the process. The cost function defined in Equation (3.2) is subject to the following constraints:

$$\begin{cases} G(x(t),t)\leq 0 & \\ x(t)\in\mathscr{X}(t) & \forall t\in[t_0,t_f] \\ u(t)\in\mathscr{U}(t) & \end{cases} \tag{3.4}$$

where $G(x(t),t)\leq 0$ denotes a generic instantaneous constraint, and $\mathscr{X}(t)$ and $\mathscr{U}(t)$ denote the set of admissible state and control values, respectively, at time t. L can be the instantaneous fuel consumption or any other instantaneous scalar index: the cost function, for example, can take into account the emission rates of the pollutants by introducing a weighting factor for each pollutant species [92], or drivability issues by adding an anti-jerk term [93]. The optimization problem can be subjected to additional local and integral constraints. Local constraints are imposed to limit the state and control variables, e.g., the engine torque and speed, the motor power, the battery SoC, etc. Integral constraints, instead, can be used for adding a generic penalization at the end of the process. If, for example, the performance index defined in Equation 3.2 just takes into account the engine fuel consumption, the solution to the minimization problem is trivial: the performance index is minimized by a purely electrical strategy, i.e., all the traction power is provided by the battery. This choice, however, will completely discharge the battery at the end of the mission. The integral constraints on the SoC can be used to correct this behavior. The integral (or terminal) constraints can be enforced either as hard or soft constraints [12]. Hard constraints consist in the boundary conditions (3.3) on the dynamic equations by requiring that the energy stored at the end of the mission equal the value at the start of the mission; soft constraints, on the other hand, modify the cost function (3.2) with the term $\phi(x(t_f),t_f)$ in order to induce the final value of the constrained variable to be close, but not necessarily identical, to the desired target.

3.3 State-of-the-Art Control Strategies

This Section presents various approaches for the evaluation of the optimal control law. In the literature, different categories of strategies have been proposed, and within this variety, a general classification can be outlined by identifying three general trends:

- Global optimization methods:
  The entire optimization problem is considered as a whole, and information about past, present, and future driving conditions is assumed to be completely known. This category includes Dynamic Programming (DP) [94] and Pontryagin's Minimum Principle (PMP) [95];
- Local optimization methods:
  The global problem is reduced to a sequence of local problems (but not necessarily instantaneous). In this case, information about the past and the present conditions is used, while prediction of future driving conditions may be used, for example in a receding-horizon approach. Model Predictive Control (MPC) [96], Stochastic Dynamic Programming (SDP) [97], and Equivalent Consumption Minimization Strategy (ECMS) [2] all belong to this category;
- Heuristic strategies:
  A set of rules that, on the basis of some significant variables, decides the power split among the on-board power sources. [98].

Some of the strategies studied in the literature are presented in the following Sections, pointing out the assumptions on which they are based and the applications for which they are suitable.

3.3.1 Dynamic Programming (DP)

Dynamic Programming (DP) [94] [90] is a numerical method for solving optimal control problems that guarantees global optimality, regardless of the type of problem. Unfortunately, it is non-casual (if applied to the energy management of HEVs, it requires the entire driving cycle to be known in advance), and the required computational effort increases exponentially with the number of state and control variables of the underlying dynamic system. When dealing with systems with continuous state variables, the state space typically needs to be discretized. Even if it is possible to

circumvent discretization, e.g., when the cost-to-go function can be expressed analytically, in general, discretization is the only viable option. Discretization, however, introduces numerical errors, which degrade the accuracy of the solution [99].

DP algorithm is based on Bellman's principle of optimality, which can be expressed as follows:

> *"An optimal policy has the property that whatever the initial state and initial decision are, the remaining decisions must constitute an optimal policy with regard to the state resulting from the first decision" [94].*

This means that the optimal path from any of its intermediate steps to the final one corresponds to the terminal part of the entire optimal solution. The mathematical transliteration of this simple principle can yield the equations given below. Since DP is discrete in nature, time, state space, and control space need to be discretized. Consider a discrete-time system, with a fixed final time:

$$x_{k+1} = f_k(x_k, u_k) \tag{3.5}$$

with $k = 0, 1, \ldots, N-1$, $u_k \in \mathscr{U}_k$, and $x_k \in \mathscr{X}_k$, and the control policy:

$$\pi = \{u_0, u_1, \ldots, u_{N-1}\} \tag{3.6}$$

The cost of π starting at time 0 (and state x_0) to time $N-1$ is:

$$J_\pi(x_0) = L_N(x_N) + \sum_{k=0}^{N-1} L_k(x_k, u_k) \tag{3.7}$$

where L_k is the instantaneous cost function, i.e., the cost of applying the control signal u at discrete time k to the dynamic system given by Equation 3.5. The optimal cost function is the one that minimizes the total cost:

$$J^*(x_0) = \min_\pi J_\pi(x_0) \tag{3.8}$$

and the optimal policy $\pi^* = \{u_0^*, u_1^*, \ldots, u_{N-1}^*\}$ is:

$$J_{\pi^*}(x_0) = J^*(x_0) \tag{3.9}$$

Consider now the "tail subproblem" that minimizes the cost-to-go function from time i (and state x_i) to time $N-1$:

$$V_i = L_N(x_N) + \sum_{k=i}^{N-1} L_k(x_k, u_k) \tag{3.10}$$

and the "tail optimal policy" $\{u_i^*, u_{i+1}^*, \ldots, u_{N-1}^*\}$, i.e., the last part of the optimal policy π^*. Bellman's principle of optimality states that "the tail policy is optimal for the tail subproblem". This statement is analytically proved by [90] where the induction principle is used to show that $J_k(x_k) = J_k^*(x_k)$, where $J_k^*(x_k)$ is the optimal cost of the tail subproblem that starts at time k and state x_k.

Bellman's principle of optimality is used in the DP algorithm, where starting from the final step N, the algorithm evaluates the optimal cost-to-go function $J_k(x_i)$ at every node in the discretized time state space by proceeding backward in time following the sequence of policies:

$$\mu_k^* = \arg\min_{u_k \in \mathscr{U}_k} \left(L_k(x_k, u_k) + J_{k+1}\left(f_k(x_k, u_k)\right)\right) \; k = N-1, N-2, \ldots, 1, 0 \tag{3.11}$$

$J_0(x_0)$, generated at the last step (actually, the first time step), is equal to the optimal cost $J^*(x_0)$. Thus, Bellman's principle of optimality proves that it is possible to determine the optimal sequence of control actions proceeding backward from the final state, choosing at each step the path that minimizes the cost-to-go (integral cost from that time step until the final state).

DP can be used for determining the optimal power split of an HEV, as shown in [100], where the policy is represented by the power split between the ICE and the EM at successive time steps, while the objective function corresponds to the overall energy consumption. Nevertheless, variations can be made to the definition of the policy and the objective function, e.g., considering also the engine pollutant emissions [101] or the CO_2 emissions related to the battery recharge from the grid [102]. Although DP offers the optimal solution, within the accuracy limits imposed by the discretization, it is not applicable in a real vehicle for the following reasons:

- The entire driving cycle must be known a priori because the optimal solution can only be calculated backward;

- It is computationally demanding: it requires the backward solution of the entire problem before being able to determine the first control action.

Despite these important shortcomings, DP can provide the closest approximation to the optimal solution and is often used to determine the maximum potentiality of a given architecture, thus serving as a benchmark for other control strategies, e.g., [100, 103–105].

3.3.2 Pontryagin's Minimum Principle (PMP)

Pontryagin's Minimum Principle (PMP) [1] [95] is a mathematical theorem that gives a set of instantaneous necessary conditions of optimality. A control law $u(t)$ that satisfies the conditions of the minimum principle is called extremal. Being the conditions of the minimum principle only necessary, the optimal solution, when one exists, must be an extremal control. Conversely, not all extremal controls are optimal.

There are several formulations of the principle [106]: the two most relevant for the energy management problem of HEV will be discussed in this Section. In the first formulation, no constraints are imposed on the state variable, which can assume any value in its general domain $x(t) \in \mathbb{R}^n$. Given the system equation (3.1), the cost function (3.2), and the terminal constraints (3.3), the minimum principle states that the optimal control law $u^*(t)$ must satisfy the following necessary conditions [106]:

1. $u^*(t)$ minimizes at each instant of time the Hamiltonian function, defined as:

$$H(x(t),u(t),t,\lambda(t)) = \lambda^T(t) \cdot f(x(t),u(t),t) + L(x(t),u(t),t) \tag{3.12}$$

where $f(x(t),u(t),t)$ is the right-hand side of Equation 3.1, $L(x(t),u(t),t)$ is the instantaneous cost in Equation 3.2, and $\lambda(t) \in \mathbb{R}^n$ (same dimension as the state vector $x(t)$) is a vector of optimization variables, also known as adjoint states or co-states of the system. The optimal solution $u^*(t)$ is such that:

$$u^*(t) = \arg\min_{u \in \mathscr{U}} (H(u(t),x(t),\lambda(t),t)) \tag{3.13}$$

[1] The minimum principle was originally proposed as a maximum principle by the Russian mathematician Lev Semenovich Pontryagin and his students in 1958 and later described in [95].

2. The co-state must satisfy the dynamic equation

$$\dot{\lambda}(t) = -\left.\frac{\partial H}{\partial x}\right|_{u^*(t)} \tag{3.14}$$

3. The state variable $x^*(t)$ must satisfy the terminal constraints

$$\psi\left(x(t_f), t_f\right) = 0; \tag{3.15}$$

Since no terminal conditions are imposed on the state, the terminal condition is given as:

$$\lambda^*(t_f) = \left.\frac{\partial \phi\left(x(t_f), t_f\right)}{\partial x}\right|_{*,t_f} \tag{3.16}$$

where $\phi\left(x(t_f), t_f\right)$ is the terminal cost from (3.2).

In the second formulation, the state variables are constrained to remain within some boundaries, which can be time-varying:

$$x(t) \in \Omega_x(t) \subset \mathbb{R}^n \; \forall t \in [t_0, t_f] \tag{3.17}$$

The state boundaries can be expressed by defining the set of admissible states, satisfying the conditions $G(x,t) \leq 0$, i.e.:

$$\Omega_x(t) = \{x \in \mathbb{R}^n | G(x(t), t) \leq 0\} \tag{3.18}$$

where the function $G(x(t),t) : \mathbb{R}^n \mapsto \mathbb{R}^p$ represents a set of p inequalities that the components of the state vector must satisfy.

PMP is a rather powerful theorem because it expresses the global optimal control problem in terms of local conditions, (3.1) and (3.14), and in terms of the instantaneous minimization (3.13). The problem, however, cannot be solved as a standard dynamic evolution problem, because its global nature is hidden in the initial and final boundary conditions. A limit of this technique is that the equations must be derived using a system model expressed in a simple form, but, if excessively simplified, the model may not be representative of the real system and the resulting optimal control may be sub-optimal. Moreover, applying PMP requires the a-priori knowledge of

the entire optimization horizon, which confines real-time implementation to cases in which the vehicle mission is either perfectly known or predictable.

3.3.3 Equivalent Consumption Minimization Strategy (ECMS)

The Equivalent Consumption Minimization Strategy (ECMS) is a static technique that relies on the instantaneous optimization of the powertrain energy flows. Since it was first proposed by Paganelli in 1999 [107, 2], the ECMS has received a lot of attention thanks to its potential to achieve sub-optimal results, while being feasible in a vehicle ECU. The basic idea of the ECMS is to move from a global optimization problem to a local minimization one: an equivalent fuel consumption, obtained by summing the actual engine fuel consumption, $\dot{m}_f(t)$, to a "virtual" fuel consumption (related to the use of the battery), $\dot{m}_{el}(t)$, is minimized at each instant of time [107]:

$$\dot{m}_{f,eq}(t) = \dot{m}_f(t) + \dot{m}_{el}(t) = \dot{m}_f(t) + \frac{s(t)P_{batt}(t)}{Q_{LHV}} \tag{3.19}$$

where $P_{batt}(t)$ is the instantaneous power provided ($P_{batt} > 0$) or absorbed ($P_{batt} < 0$) by the battery; Q_{LHV} [MJ/kg] is the fuel lower heating value (energy content per unit of mass); $s(t)$ is the instantaneous equivalence factor converting the battery energy consumption into a corresponding (or "virtual") fuel consumption [108]. For any vehicle operating point (speed, power required from the powertrain) the entire range of possible power splits is examined, and the equivalent fuel flows are determined for every combination, using the actual efficiency maps of the engine and electric machines. The combination with the lowest instantaneous fuel cost is selected. This approach, however, requires the appropriate value of equivalence factor $s(t)$ to properly estimate the cost of the energy stored in the battery: its optimal value, which entails the SoC balance at the end of the cycle, depends on both the powertrain topology and the specific mission profile. A wrong guessing of this parameter may jeopardize the benefits of the ECMS leading to results far from optimality. Figure 3.2 depicts the paths followed by the power flow during discharge (Figure 3.2a) and charge (Figure 3.2b), for a parallel HEV (in a series configuration the power summation node is located in a different point).

The following remarks can be made:

- During discharge, the electric motor provides mechanical power. The dotted route represents the energy that will be necessary to recharge the battery in the

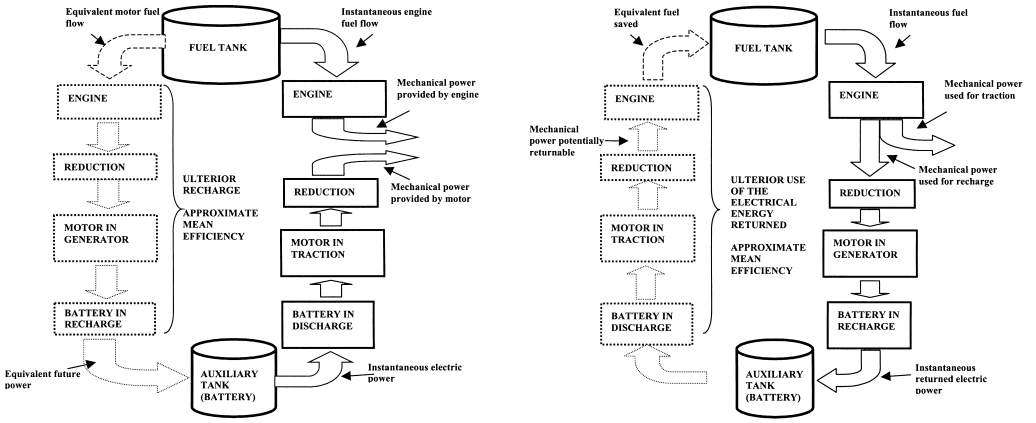

(a) Discharge (b) Charge

Fig. 3.2 Power flows during charge and discharge in a parallel HEV [2]

future. Since the operating point of this recharge cannot be known a priori, the average efficiency should be used.

- During charge, the electric motor receives mechanical energy and converts it into electrical energy that is stored in the battery. The dotted route represents the surplus energy that can be used in the future to produce mechanical power: since the EM will assist the ICE, this would allow less fuel to be used by the ICE in the future.

The theoretical bases of the ECMS were expanded by subsequent studies that demonstrated the correlation between the ECMS and PMP [109]. Thus, the ECMS can generate a sub-optimal control law, but only with the a priori knowledge of the entire mission profile, because the equivalence factor must be tuned, through a numerical optimization procedure, according to the driving conditions to achieve the charge sustainability. Despite its instantaneous formulation, the ECMS still implicitly relies on information about the future: if this information is wrong, the control still works, but the results are far from optimality. Therefore, since its initial introduction, several improvements and modifications have been proposed to direct the technique toward an online adaptation of the equivalence factor [110–112]. The most common methodology for the adaptation of the equivalence factor relies on a mathematical expression, which periodically modifies this parameter based on its past values and the difference between actual and reference SoC [113]:

$$s_{k+1} = \frac{1}{2}(s_k + s_{k-1}) + k_p(SoC_0 - SoC(t)) \tag{3.20}$$

with:

$$t = kT \quad k = 1, 2, ... \tag{3.21}$$

where s_k is the value of the equivalence factor currently used; s_{k-1} is the value used in the previous time interval; s_{k+1} is the value that will be used in the subsequent time interval; $(SoC_0 - SoC(t))$ is the difference between reference and actual SoC values, at the instant of the adaptation; k_p is the proportional gain of the feedback controller; T is the adaptation period. It should be noted that since the strategy usually aims to achieve charge sustainability, the initial SoC is used as the reference value.

3.3.4 Heuristic Strategy

The most common way of implementing supervisory control in an HEV is to introduce a set of rules that, on the basis of the observed values of some meaningful parameters, decide the power split among the on board power sources. Unlike the ones based on optimal control, Rule-Based (RB) techniques [98, 114–116] do not rely on formal models, but on rules based on engineering intuition: the objective is to make each element of the powertrain work in high-efficiency conditions. Figure 3.3 depicts a simple RB structure.

The rules are usually in the form of if-then-else logic, based on efficiency maps or fuzzy-logic methods. RB controllers depend only on instantaneous conditions that take into account the local constraints (i.e., limitations on power, torque, speed, etc.). The parameters of the RB controller (e.g., the threshold values that decide when to switch from one mode to another) are usually obtained from a calibration phase, where optimal control strategies, such as DP, can be used to benchmark or validate the effectiveness of the strategy [111, 117] or as a guideline to determine the control rules [98, 116, 118]. The main advantage of RB strategies is their conceptual simplicity and their notably limited computational effort. On the other hand, the presence of many thresholds and parameters makes it quite difficult to obtain an appropriate calibration that works for a wide variety of driving conditions. Hence, RB controllers cannot guarantee the optimality of the solution and cannot respect the integral constraints as, for example, the charge sustainability: the rules can only force a given integral measure (in this case, the SoC) to vary between two limits.

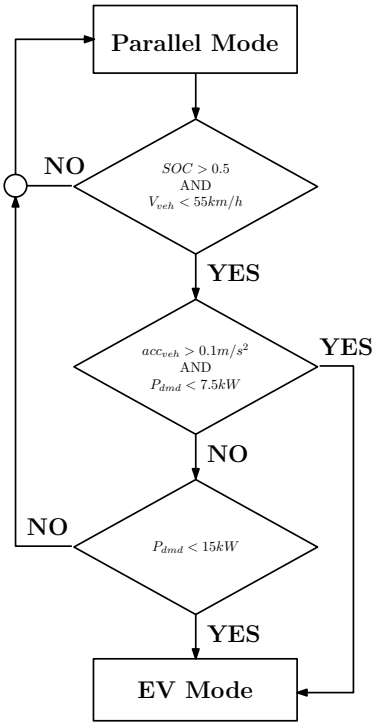

Fig. 3.3 An example of rule-based control.

3.4 EMS Enhancement

In the last decades, the EMSs of HEVs have been extensively studied and compared [14]. As depicted in Figure 3.4, which summarizes the EMS evolution in the past three decades based on the literature review carried out by [3], from the first proposed RB strategies, performance has constantly increased, and the current trend is towards real-time global optimum control. The advances in the field of AI (see Section 2.3), in addition to the possibility of scaling up computations on cloud platforms, have led to increasing interest in the exploitation of ML techniques for the energy management of HEVs. In particular, Reinforcement Learning (RL) is taking the lead as the preferred control strategy since it combines real-time implementation characteristics from RB methods and global optimum characteristics from DP [119]. The main challenge of current EMSs, though, is to attain optimal results in a real cycle since they are generally devised under specific driving conditions.

In this context, vehicle speed prediction can play a key role in improving the performance of the current strategies. In an ITS framework (see Section 2.4.1), HEVs and pHEVs can benefit the most since the information from the surrounding environment can be used to optimize their control strategies, allowing the development of the so-called predictive EMS.

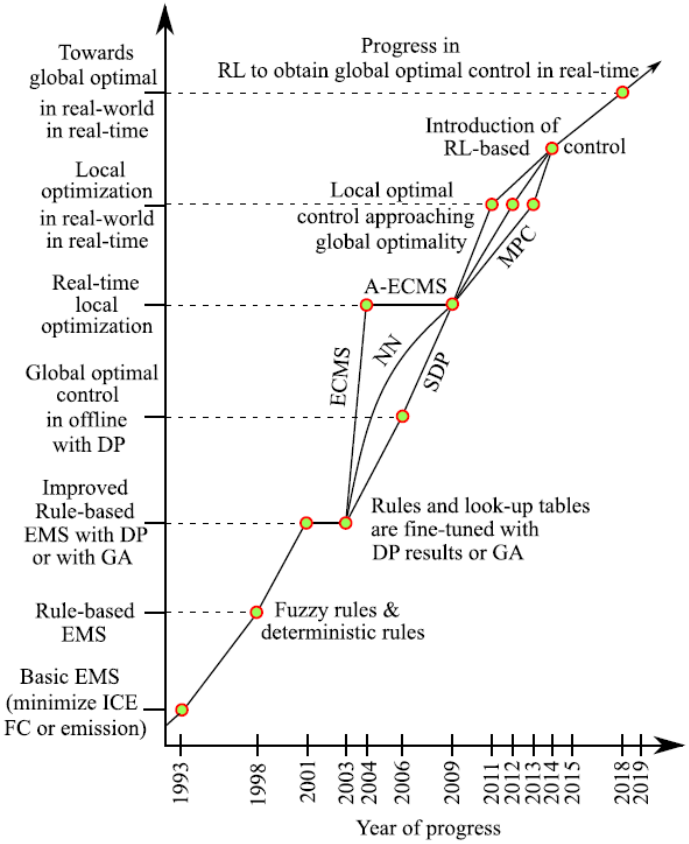

Fig. 3.4 Evolution of EMSs from 1993 to 2018 [3].

Although predicting the lead vehicle velocity can also be possible in the absence of connectivity or under data-restricted cases [120], Vehicle-to-Everything (V2X) communication along with cloud computing adoption may enable a change of paradigm of the energy management problem: from an instantaneous optimization to globally minimizing it over the entire driver route [121]. In this framework, several works have investigated the opportunities provided by the integration of vehicle speed prediction into the EMS of a hybrid powertrain [122, 123]. If the vehicle speed can be predicted as accurately as possible by taking into consideration traffic congestion and road slope, the EMSs can be effectively enhanced. Therefore, incorporating dynamic traffic conditions into EMSs and investigating predictive EMSs based on driving cycle prediction are possible future trends [14]. A deeper overview of state-of-the-art predictive EMS can be found in [22].

Moreover, the energy management strategies are mainly aimed at minimizing fuel economy and emissions, and they often neglect other performance factors, such as battery SoH (see Section 2.2.4). However, battery aging affects energy efficiency and fuel economy, and being able to incorporate these performance indexes to implement

them in an integrated optimization is a key issue. Some exceptions will be given below. Authors in [124] first proposed a variation of the PMP (see Section 3.3.2), where the reduction of battery life deriving from its usage is treated as an additional cost. In [125], the EMS problem is addressed and formalized as a mixed integer convex problem and the cost function takes into account also electricity and battery aging costs. Finally, in [126], an RL-based EMS for a pHEV is proposed that also considers the battery health. Nevertheless, the definition of SoH indicators that can exhaustively capture battery aging and that can be integrated into a real-time implementable strategy still remains an open research issue.

Chapter 4

xEVs Modeling

4.1 Introduction

Up until quite recently, new product development required physical prototype testing, with a huge amount of time and money invested by the manufacturers: months or years are needed to collect and analyze experimental data. In the context of increasing competitiveness, minimizing time and cost is key to the success of a new product, and numerical simulation can play a pivotal role: physical systems can be approximated by mathematical models, and the behavior of the physical system can be studied by simulating it in a virtual environment. Moreover, numerical methods enable solving complex mathematical systems, even when an analytical solution cannot be found, e.g., non-linear systems.

Moreover, in the last decades, the increasing concerns about environmental issues have made energy efficiency and pollutant emissions reduction among the primary selling points for automobiles, and numerical simulation is necessary at every stage of the design process in order to develop fast, efficient, and cost-effective engines [127]. Focusing on xEVs, the design and the optimization of these systems require numerical simulation support since, due to their complexity, the direct experimental analysis of different configurations and control strategies will be impossible.

4.2 Vehicle Modeling

Detailed simulation models are usually available and routinely used for the development of single components or subsystems (e.g., 1D-CFD models for ICE or

3D-CFD models for in-cylinder phenomena). At the vehicle level, however, the system complexity and the necessity to simulate the fuel consumption (or pollutant emissions) over long-duration driving cycles, a detailed 1D model will result in excessive computational cost. In these cases, vehicle-level energy analysis is more suitable and look-up tables are commonly used for simulating fuel consumption and pollutant emissions.

4.2.1 Equations of Motion

When the vehicle's longitudinal dynamics are investigated, the vehicle can be considered as a point mass. By applying the equilibrium to the point mass, as shown in Figure 4.1, its equilibrium equation can be written as:

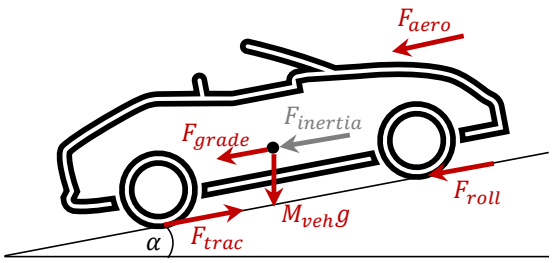

Fig. 4.1 Forces acting on a vehicle.

$$M_{veh}\frac{dv}{dt} = F_{inertia} \tag{4.1}$$

where M_{veh} is the total vehicle mass (considering all the driveline components' inertia), v is the longitudinal vehicle velocity, and $F_{inertia}$ is the inertial force. The latter can be rewritten by considering its different components:

$$F_{inertia} = F_{pwt} - F_{brk} - F_{roll} - F_{aero} - F_{grade} \tag{4.2}$$

where F_{pwt} is the tractive force generated by the powertrain, F_{brk} is the resistive force coming from the brakes, F_{roll} is the rolling resistance, F_{aero} is the aerodynamic resistance, and F_{grade} is the resistant force due to road slope. The rolling resistance force is usually modeled as [12]:

$$F_{roll} = c_{roll}M_{veh}g\cos\alpha \tag{4.3}$$

where g is the gravitational acceleration, α is the road slope angle, and c_{roll} is the rolling resistance coefficient. The latter is a function of vehicle speed, tire pressure, and external temperature and can be modeled as:

$$c_{roll} = c_0 + c_1 v + c_2 v^2 + c_3 v^3 \tag{4.4}$$

where c_i are the coefficients linking c_{roll} to the vehicle speed. The aerodynamic resistance can be expressed as:

$$F_{aero} = \frac{1}{2} \rho_{air} A_f C_d v^2 \tag{4.5}$$

where ρ_{air} is the air density, A_f the vehicle frontal area, C_d the aerodynamic drag coefficient. Finally, the resistant force due to road slope can be expressed as:

$$F_{grade} = M_{veh} g \sin \alpha \tag{4.6}$$

Aerodynamic and rolling resistances are usually experimentally determined in a so-called coast-down test: i.e., a free vehicle deceleration test. In these conditions, the deceleration is only due to aerodynamic and rolling resistances, and, by measuring the instantaneous vehicle speed, the total drag force acting on the vehicle can be evaluated as:

$$F_{roll+aero} = C_0 + C_1 v + C_2 v^2 \tag{4.7}$$

where C_0, C_1, and C_2 are called Coast-Down coefficients [127].

These equations represent the starting point for vehicle modeling and can be sufficiently accurate if the parameters are correctly identified. The three most common approaches suitable for this application will be briefly described.

4.2.2 Backward Kinematic Analysis

The backward approach is usually adopted for predicting a vehicle's fuel economy or pollutant emissions during a driving cycle. The vehicle speed and the road grade are supposed to be known and imposed on the vehicle. The internal powertrain dynamics are neglected because efficiency, power loss, and fuel consumption maps are used to model the components, e.g., the ICE returns a value of instantaneous fuel

consumption and of emission rate in function of its angular speed and torque. Despite the introduced simplifications, the look-up tables approach is widely adopted, because it is computationally efficient, and the overall fuel consumption and emissions predictions over the driving cycles have acceptable accuracy, especially for a first preliminary estimation. This approach, however, neglects all the dynamic phenomena considering transient conditions as a sequence of stationary states: during highly dynamic events, the simulation results can significantly differ from the experimental data. The typical information flow of a backward analysis can be easily understood with the block diagrams shown in Figure 4.2.

Fig. 4.2 Information flow in a backward kinematic approach.

4.2.3 Forward Dynamic Analysis

In the forward dynamic approach, the ICE is modeled through detailed 0D or 1D fluid-dynamic models: the ICE behavior is simulated with satisfactory accuracy even during highly dynamic events, e.g., a tip-in maneuver that accelerates the vehicle from a standstill. Contrary to the backward analysis, the vehicle speed is not imposed but is seen as a target value, and the driver model - a Proportional-Integral-Derivative (PID) controller - decides the instantaneous power delivery through the brake and accelerator pedals in order to achieve the target speed. Then, the vehicle dynamics equation is used to compute vehicle acceleration and speed. The forward analysis information flow is shown in Figure 4.3.

The quasi-static approach can be considered a particular case of the forward dynamic approach since system dynamics are taken into account. The main difference is that look-up tables are adopted for modeling the behavior of the powertrain components, i.e., ICE, EM, and battery. The quasi-static approach can predict the fuel consumption of a vehicle performing a driving cycle with reasonable accuracy, but cannot be suitable for other applications, such as soot emissions prediction, fast transients, and turbocharging system response simulation, because of their non-linearity.

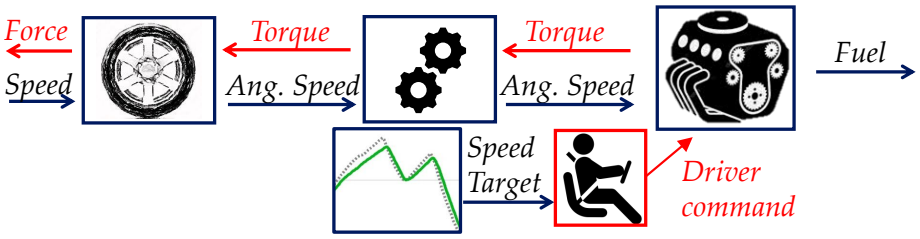

Fig. 4.3 Information flow in a forward dynamic approach.

4.3 ICE Modeling

A mathematical model correctly describing the physical phenomenon is a *sine qua non* for numerical simulation. Depending on the timescale and the nature of the modeled system, different degrees of detail can be adopted for ICE modeling. In Figure 4.4 the main engine modeling methodologies are shown: the y-axis represents the real-time factor, i.e., the ratio between simulation and real-life cycle duration.

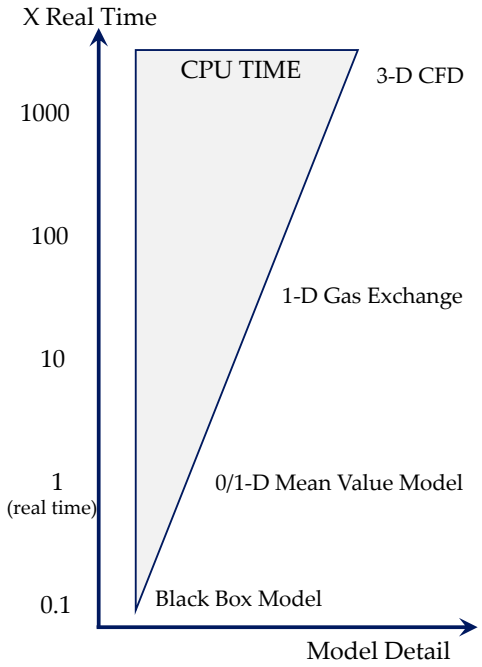

Fig. 4.4 Main engine modeling methodologies: model detail vs. computational time.

As evident from Figure 4.4, the 3D-CFD is the most complete and detailed approach, but it requires enormous computational effort. It is routinely adopted for modeling in-cylinder phenomena (e.g., combustion process, direct fuel injection, mixture formation, gas flow through intake and exhaust valves, etc.) as well

as for modeling flow dynamics of intake and exhaust systems. However, since the computational time increases with the volume of the discretized system, this methodology is usually applied to a specific engine component, and almost never to system-level simulations. On the other hand, 1D-CFD models are generally used to provide a system-level perspective: a network of ducts connected by junctions is used to model the engine intake and exhaust systems. For each element of the network, the equations governing the conservation of mass, momentum, and energy are solved by means of a finite difference technique. A good level of prediction can be achieved both under steady-state operating conditions and during transient phases, while not requiring excessive computational time. Finally, map-based models can obtain a significant reduction in computational time, at the expense of less detail. The ICE is modeled by means of experimental steady-state maps where the engine efficiency, power loss, and fuel consumption are defined, and the instantaneous fuel consumption and emissions rates are obtained by maps interpolation. This approach is routinely used for fuel consumption and emissions calculations on type approval driving cycles, where the smooth transients can be approximated by means of a sequence of stationary states. However, map models are unsuitable for fast transients or turbocharging system response simulation, given their non-linearity. 1D fluid-dynamic models would certainly be more appropriate because the map models neglect most of the engine dynamic phenomena. On the other hand, the computational effort of 1D fluid-dynamic models is more demanding, making it improper for long-lasting simulations, e.g., for driving cycles.

4.4 EM Modeling

When a system-level approach is adopted, EMs are typically modeled via a map-based methodology, i.e., their behavior is described by means of torque and efficiency maps. Due to the high speed at stake, the only element that is dynamically modeled is the rotor inertia: the electrical dynamics are much faster than the inertial or the engine ones. Depending on the model, power or torque can be used as a control input, and the relation between mechanical torque and electric power can be provided by an efficiency map (as a function of speed and torque/power). The efficiency of the power electronics system can be modeled by means of an ad hoc efficiency map or can be included in the EM efficiency map.

When in traction mode, the power needed at the shaft, P_{mech}, can be calculated from the electric power command, P_{elec}, and the efficiency map, η:

$$P_{mech} = \frac{P_{elec}}{\eta} \tag{4.8}$$

On the contrary, when in generator mode, the electric power can be calculated from the mechanical one:

$$P_{mech} = P_{elec}\eta \tag{4.9}$$

The power can be either positive or negative depending if the EM works in traction or generator mode, respectively. The power loss is always positive and is formulated as follows:

$$P_{loss} = P_{elec} - P_{mech} \tag{4.10}$$

4.5 Battery Modeling

A significant scientific effort has been made to create high-fidelity battery models in response to the growing interest in xEVs. These models are helpful in designing BMS algorithms for diagnostic, prognostic, and control applications as well as for forecasting and evaluating cell behavior and enhancing cell design. However, the nonlinear correlations between all its major parameters make modeling a device like a battery a challenging task. Two general approaches can be outlined in the literature, i.e., physics-based models and data-driven models, giving particular emphasis to Li-Ion batteries, the most common types used in xEVs.

4.5.1 Physics-Based Models

In the physics-based approach, the models are built from first principles, and the parameters are tuned using a relatively small number of tests. As shown in Figure 4.5, different degrees of detail can be adopted with a trade-off between more detailed insights and less computational complexity. Generally speaking, the predictive ability and accuracy of a model are inversely proportional to its length scale. As a result, the smaller the length scale, the higher the computational effort and complexity of the model. At the atomic scale, the models can be used to simulate material properties [37], such as diffusion; alternatively, phase-field approaches can be used

to study phase changes on a molecular scale [4], and microscale models using non-equilibrium thermodynamics can be used to simulate the 3D microstructures of porous electrodes [128]. From a system perspective, other typologies of models are more appropriate, e.g., Equivalent Circuit Model (ECM) or electrochemical models. Some of these models are presented in the following Sections, pointing out the assumptions on which they are based and the applications for which they are best suited.

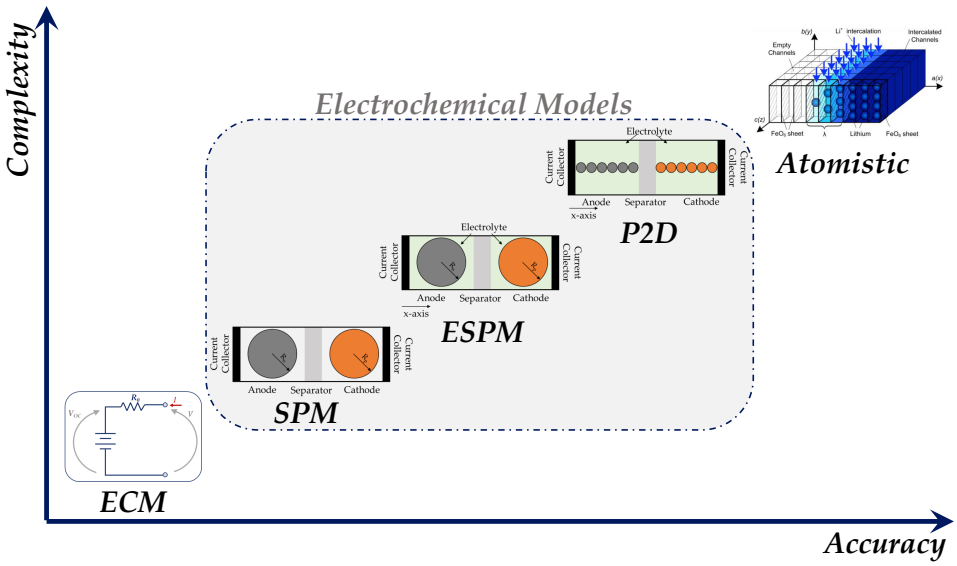

Fig. 4.5 The spectrum of battery models in the literature with a trade-off between more detailed insights and less computational complexity: ECM, SPM, ESPM, P2D, and Atomistic [4].

Equivalent Circuit Model (ECM)

The Equivalent Circuit Model (ECM) is the most popular approach for cell modeling: it uses an electrical-circuit analogy to approximate the cell's voltage response to different input-current stimuli. The circuit acts as a description of the cell's behavior, and the various circuit elements act as analogs to some of the internal processes [33]. A typical ECM is represented in Figure 4.6. The resistance R_0 represents the Ohmic losses due to the resistance of the wires, the resistance of the electrodes, and the dissipative phenomena that reduce the power available at the terminals. The resistance R_1 and the capacitance C_1 are used to model the dynamic response of the battery. The model depicted in Figure 4.6 is a first-order approximation (one R-C branch), but more R–C branches can be used to increase the model accuracy.

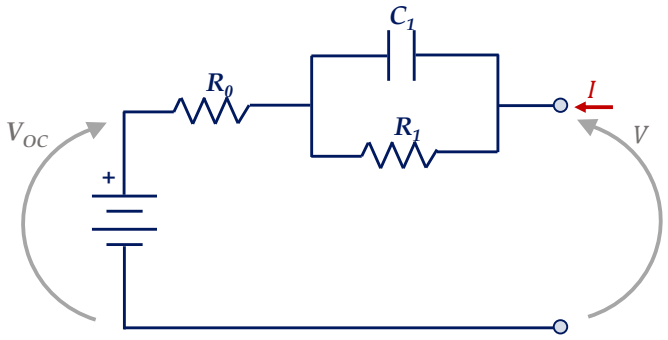

Fig. 4.6 Battery equivalent circuit-based model (second-order).

The voltage at the terminals can be expressed as:

$$V_L = V_{oc} - R_0 I - \sum_{i=1}^{n} V_i \tag{4.11}$$

where V_{oc} is the Open Circuit Voltage (OCV), i.e., the voltage measured at the terminals when the cell is unloaded and in complete equilibrium, V_i is the voltage across the ith R–C branch (characterized by the resistance R_i and the capacitance C_i), n is the order of the dynamic model considered, i.e., the number of R–C branches (in the example shown $n = 1$). The behavior of the R-C branch can be described with the 1^{st}-order differential equation:

$$C_i \frac{dV_i}{dt} = I - \frac{V_i}{R_i} \tag{4.12}$$

The capacitance C_i and the resistance R_i can, in principle, change with the direction of the current (charge or discharge) and with other operating conditions, such as temperature. The values of the parameters, i.e., R_0, R_i, and C_i, are estimated using curve fitting of experimental data, and the number of parameters to be identified increases with the model accuracy. Due to their simplicity, the ECM models allow for fast computation and are best suited for real-world applications: at present, the majority of Battery Management Systems (BMS) use ECM as a basis for maintaining the proper operating boundaries for the cells and for estimating internal cell states. Despite its conceptual simplicity, however, parameter identification is a non-trivial step: the parameters are a function of multiple variables and are generally a function of the operating conditions, i.e., temperature, SoC, etc. Although these models can be very accurate in specific situations, their validity is limited to the specific

operating conditions in which they have been calibrated and therefore they may lack generality.

Electrochemical Models

Electrochemical models are derived from the porous electrode and concentrated solution theory, via volume-averaging [129], or homogenization theory [130], and predict the system-level response of a cell from a fundamental characterization of the physical phenomena involved in the process. Because mass transport occurs mainly through diffusion, the dynamics of the ionic concentrations are described by Partial Differential Equations (PDEs). This represents a significant increase in complexity, with respect to the ECM, and solving the equations typically requires the adoption of numerical methods.

Pseudo-Two-Dimensional (P2D) Model

The most popular electrochemical model is the so-called Pseudo-Two-Dimensional (P2D) model - also known as Doyle-Fuller-Newman (DFN) model. It was developed by Newman et al. [129], and it simulates the lithium transport and diffusion both in the electrolyte and the electrodes. As shown in Figure 4.7, the two dimensions are the solid phase - the electrode particles are considered in a spherical domain - and the liquid phase - the electrolyte is considered in a linear domain. This allows a concentration gradient over the thickness of an electrode depending on the electrolyte transport and a gradient inside the particle depending on solid diffusion. The four governing laws that describe the battery dynamics within the solid and electrolyte phases [129, 131] are listed below.

1. Conservation of mass in the solid phase and respective boundary conditions:

$$\frac{\partial c_{s,j}}{\partial t} = D_{s,j}\left[\frac{\partial^2 c_{s,j}}{\partial r^2} + \frac{2}{r}\frac{\partial c_{s,j}}{\partial r}\right] \tag{4.13}$$

$$\left.\frac{\partial c_{s,j}}{\partial r}\right|_{r=0} = 0 \tag{4.14}$$

$$\left.\frac{\partial c_{s,j}}{\partial r}\right|_{r=R_j} = \frac{-i_{int,j}}{D_{s,j}a_{s,j}F} \tag{4.15}$$

where t and r are the temporal and radial coordinates, respectively, $j \in [p,n]$ in the solid phase represents the positive or negative electrode, $c_{s,j}$ is the lithium-ion concentration of each electrode, $D_{s,j}$ is the diffusion coefficient, $i_{int,j}$ is the intercalation current, $a_{s,j}$ is the specific interfacial surface area, R_j is the radius of the spherical particle, and F is the Faraday constant. The boundary conditions are defined at the center ($r = 0$) and the surface ($r = R_j$) of the solid particle. The flux of lithium ions at the center is zero, and the flux at the surface is equal to the rate at which lithium ions are transported between solid and electrolyte phases.

2. Conservation of charge in the solid phase and respective boundary conditions:

$$\frac{\partial}{\partial x}\left(\sigma_{eff,i}\frac{\partial \phi_{s,j}}{\partial x}\right) - a_{s,j} i_{int,j} = 0 \tag{4.16}$$

$$\left.\frac{\partial \phi_{s,j}}{\partial x}\right|_{x=L_n+L_s+L_p} = \frac{I_{batt}}{\sigma_{eff,i}} \tag{4.17}$$

$$\left.\frac{\partial \phi_{s,j}}{\partial x}\right|_{x=L_n} = \left.\frac{\partial \phi_{s,j}}{\partial x}\right|_{x=L_n+L_s} = 0 \tag{4.18}$$

where x is the linear Cartesian coordinate (it is defined in $x \in [0,L]$, with $L = Ln + Ls + Lp$), $\phi_{s,j}$ is the solid phase potential and $\sigma_{eff,i}$ is the effective electronic conductivity.

3. Conservation of mass in the electrolyte phase and respective boundary conditions:

$$\varepsilon_{e,j}\frac{\partial c_{e,j}}{\partial t} = \frac{\partial}{\partial x}\left(D_{e,j}^{eff}\frac{\partial c_{e,j}}{\partial x}\right) + (1 - t_0^+)\frac{\pm i_{int,j}}{F} \tag{4.19}$$

$$\left.\frac{\partial c_{e,j}}{\partial t}\right|_{x=0} = \left.\frac{\partial c_{e,j}}{\partial t}\right|_{x=L} = 0 \tag{4.20}$$

$$D_{e,n}^{eff}\left(\frac{\partial c_{e,n}}{\partial x}\right)\Bigg|_{x=L_n^+} = D_{e,s}^{eff}\left(\frac{\partial c_{e,s}}{\partial x}\right)\Bigg|_{x=L_n^-} \tag{4.21}$$

$$D_{e,s}^{eff}\left(\frac{\partial c_{e,s}}{\partial x}\right)\Bigg|_{x=L_n+L_s^+} = D_{e,p}^{eff}\left(\frac{\partial c_{e,s}}{\partial x}\right)\Bigg|_{x=L_n+L_s^-} \tag{4.22}$$

where $j \in [p,n,s]$ in the electrolyte phase represents the cathode, the anode, or the separator, $c_{e,j}$ is the lithium-ion concentration, t_0^+ is the transference number, $D_{e,j}^{eff}$ is the electrolyte phase effective diffusion coefficient. Note that a zero flux boundary condition is imposed at the current collectors, while continuity of concentration and flux is assumed between the anode, the separator, and the cathode.

4. Conservation of charge in the electrolyte phase and respective boundary conditions:

$$\kappa_j^{eff} \frac{\partial^2 \phi_{e,j}}{\partial x^2} - \kappa_{D,j}^{eff} \frac{\partial^2 \ln c_{e,j}}{\partial x^2} + a_{s,j} i_{int,j} = 0 \tag{4.23}$$

$$\left.\frac{\partial \phi_{e,j}}{\partial x}\right|_{x=0} = \left.\frac{\partial \phi_{e,j}}{\partial x}\right|_{x=L_n+L_s+L_p} = 0 \tag{4.24}$$

where $\phi_{e,j}$ is the electrolyte phase potential, κ_j^{eff} is the effective ionic conductivity in the electrolyte phase, and $\kappa_{D,j}^{eff}$ is the diffusional conductivity.

Despite being highly accurate for simulating charge-discharge cycles, the P2D model has a complex mathematical structure, including algebraic constraints, and requires a big parametrization effort and significant computing resources. These models are unsuitable for real-time applications: to become more widely adopted for lifetime estimation, the computational time needs to be reduced, either through the development of reduced-order models or numerical methods [132].

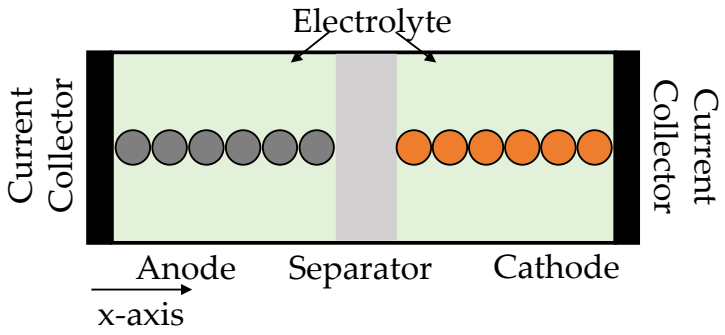

Fig. 4.7 Schematic representation of the Pseudo-Two-Dimensional (P2D) model.

Enhanced Single-Particle Model (ESPM)

The ESPM is a reduced-order electrochemical model that approximates the behavior of the entire electrode by a single spherical particle as represented in Figure 4.8. In this model, the law of charge conservation in the solid phase is relaxed under the assumption of infinite conductivity. Therefore, the ESPM is governed by only three conservation laws: the mass conservation laws in the solid (Equation 4.13) and electrolyte phase (Equation 4.19), and the charge conservation in the electrolyte phase (Equation 4.23). The solid particle concentration is described along the radial dimension r, while along x only the electrolyte concentration and potential are considered (the variation of electrochemical potential in the solid particles along x is ignored) [133]. The computational effort required to simulate charge-discharge cycles is greatly reduced if compared to a P2D model.

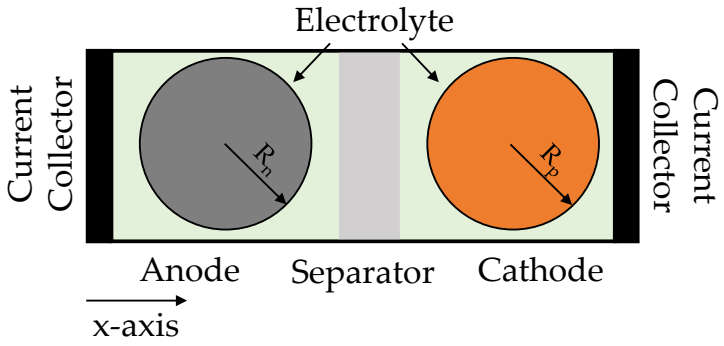

Fig. 4.8 Schematic representation of the Enhanced Single-Particle Model (ESPM).

Single-Particle Model (SPM)

The Single-Particle Model (SPM) was first used for modeling lithium-ion batteries in [134], and represents a further approximation of the ESPM: as shown in Figure 4.9 it does not only approximate each electrode with a single spherical particle with uniform current distribution (like the ESPM) but also assumes uniform lithium concentration in the electrolyte phase, thereby neglecting the electrolyte dynamics. Thus, the conservation of mass in the solid phase (Equation 4.13) is the only physical law governing the SPM dynamics. This approximation further reduces the computational effort making it suitable for the design of real-time observers and controllers for on-board applications. Despite this approximation, the SPM predicts well the battery behavior at low C-rates [135]: the SPM model can simulate entire charge-discharge cycles within seconds, thus allowing to understand how lithium-ion cells respond

Table 4.1 Comparison of the governing laws in the electrochemical models.

Governing Laws	P2D	ESPM	SPM
Conservation of mass in solid phase	✓	✓	✓
Conservation of mass in electrolyte phase	✓	✓	✗
Conservation of charge in solid phase	✓	✗	✗
Conservation of charge in electrolyte phase	✓	✓	✗

to different input stimuli, and it can be used within control designs to give good estimates of the SoC. Nevertheless, since it ignores the dynamics of electrolyte concentration and potential, the SPM model can simulate reasonably well only thin electrodes and low current conditions but fails at high current conditions [32]. Table 4.1 compares the governing laws that describe the battery dynamics for the P2D, ESPM, and SPM.

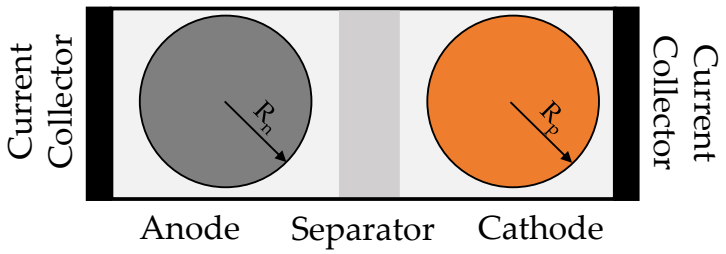

Fig. 4.9 Schematic representation of the Single-Particle Model (SPM).

4.5.2 Data-driven Models

Heuristic or data-driven techniques are model-free approaches that, creating correlations from experimental data, can be used to estimate battery SoH and predict its Remaining Useful Life (RUL). These techniques require limited battery knowledge and only need repeatable events. The recent advances in computational power and data generation have led to increasing interest in the application of Machine Learning (ML) techniques for predicting the RUL of batteries using data collected in both laboratory and online environments [136, 137]. ML approaches appear to be par-

ticularly attractive for high-rate operating conditions, where first-principles models may lack accuracy. Opportunities for improving the prediction capabilities include higher accuracy, earlier prediction, greater interpretability, and broader application to a wide range of cycling conditions.

In a purely data-driven approach, very few assumptions are made about the underlying principles governing the behavior of the battery, and machine learning models are trained with raw input signals (current, voltage, temperature, etc.), e.g., in [138]. Other types of data-driven methods extract features from the voltage, current, temperature, impedance, or power profiles that are used as inputs to machine learning models, e.g., in [26]. The feature-based models are commonly less complex than those trained with raw data, thus requiring less training data and being more readily applicable to lifetime estimation. All the data-driven approaches, however, suffer from the so-called 'curse of dimensionality': the amount of data needed to capture all combinations of operating conditions grows quickly with the number of conditions being investigated. This is compounded by the relatively slow rate at which battery lifetime data can be acquired, taking several months or years of experiments for each change in chemistry, form factor, or manufacturing process.

Finally, considering that ML and PB models both offer qualities that are distinct but complementary to each other, there is a growing trend of studies that tries to blend these two models to achieve better battery life prediction [56, 27]. These hybrid architectures are particularly promising since they could potentially combine physics-based and data-driven approaches to extrapolate outside the training data and allow accelerated development.

4.6 Modeling Tools

This Section will give some technical details about the software adopted in this work. Concerning the first case study, the data analysis and the reverse engineering of the strategy (see Section 5.1.3) were carried out in MATLAB®. For the virtual test rig development (Section 5.1.4), since fuel consumption and energy flows are the main subjects of this study, a quasi-static approach (see Section 4.2.3) was used. In particular, the software used for implementing the simulator is GT-SUITE® [139], a mono-dimensional (1D) fluid-dynamic numerical code developed by Gamma Technologies. The simulator is purely longitudinal: it does not account for any lateral or vertical motion. Steady-state efficiency maps were used for modeling the

powertrain components, i.e. ICE, EM, and battery. Since MATLAB® and Simulink® allow higher flexibility in the control design, the energy management system of the HEV was implemented in this software. MATLAB® was also employed for the vehicle speed optimization (see Section 5.2). The DP, relying on the open-source MATLAB® code developed at ETH-Zurich [140] was used for solving the optimal control problem, but it requires a simplified version of the vehicle model, relying on a backward kinematic model (see Section 4.2.2), which was built in Matlab®. This model features a lower order of dynamics in comparison with the GT-SUITE® model, i.e., it neglects any slip of the clutch and considers an instantaneous start and stop of the engine. This allows for reducing the computational requirement and satisfactorily capturing the energy flows in the vehicle.

Concerning the second case study, MATLAB® was used for developing the data pre-processing pipeline, and also for analyzing the processed field data. The simulations were run on Sherlock high-performance computing cluster at Stanford University [141].

Chapter 5

Case Study 1: Innovative EMS

The main control strategies for the energy management of HEVs, described in Chapter 3, can be used as a basis for developing advanced energy management strategies. In this context, it is of paramount importance to assess the state-of-the-art strategies already existing in the market. On the contrary, given the novelty of hybrid powertrains and their intrinsic complexities, car manufacturers are very jealous of their technical know-how, which is not usually disclosed. In this framework, this Chapter aims to propose innovative energy management strategies that are tested on a virtual test rig of a real case study. Figure 5.1 depicts the flowchart of the procedure carried out and the structure of the Chapter is summarized below:

- In Section 5.1, a digital twin of a commercially available pHEV is built. The data gathered from an extensive experimental campaign performed on the vehicle are post-processed and used to reverse engineer its control strategy and build a virtual test rig without having direct access to its EMS. This activity is described more in detail in [142];
- In Section 5.2 the virtual test rig is used to perform a vehicle speed optimization and assess, in a real-world scenario, the benefits that could be obtained by V2X connectivity and cloud computing on energy consumption and travel time. This activity, described more in detail in [143], proposes a Variable Grid Dynamic Programming (VGDP) that modifies the variable state search grid on the basis of V2X information allowing a drastic reduction in the DP computation burden by more than 95% if compared to the standard optimization performed with a fixed grid;

- The virtual test rig is then used to assess the potentialities of two advanced energy management strategies. The first one, which is described more in detail in [144], proposes an innovative deep learning-based EMS where the optimal solutions, provided by DP, are used to train RNNs to efficiently handle the energy management of the pHEV, achieving sub-optimal results. The second one, which was first proposed in [145] and further developed in [146], proposes an innovative A-ECMS algorithm. The information about future vehicle driving patterns, which could be obtained from V2X connectivity, is used by an LSTM deep learning model to find the optimal equivalence factor. For the sake of brevity only the work presented in [146] will be described in Section 5.3.

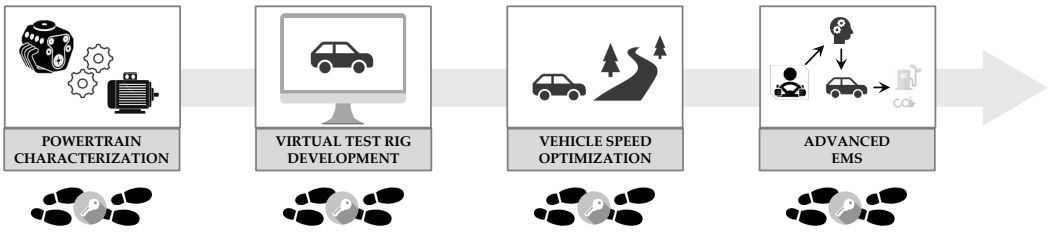

Fig. 5.1 Flowchart of the procedure carried out: powertrain characterization, virtual test rig development, vehicle speed optimization, and advanced energy management strategies.

5.1 Vehicle Digital Twin

In this Section, a virtual test rig of a commercially available pHEV is built. The data gathered from an extensive experimental campaign performed on the vehicle are carefully analyzed and post-processed in order to extract the strategy adopted by the EMS, pointing out any dependency of its decisions on the powertrain's main operating variables.

5.1.1 Test Case

The vehicle used in this Section as a case study is a Mercedes E300de, a state-of-the-art diesel pHEV available in the European market. Figure 5.2 schematically shows the powertrain layout and Table 5.1 summarizes the main vehicle and powertrain characteristics. It features a P2 architecture where a Euro 6d-temp 2.0-liter diesel ICE is coupled, through an auxiliary clutch (K0), with a 90 kW EM of PM synchronous

type. Both the ICE and the EM are connected, through a Torque Converter (TC) and a 9-speed Automatic Transmission (AT), to the rear axle. The powerful 90 kW EM, powered by a 13.5 kWh Li-Ion Nickel-Manganese-Cobalt-oxide (Li-NMC) HV battery, allows an all-electric range of 54 km, and a maximum speed, in all-electric mode, of 130 km/h. A DC/DC converter allows the HV battery to feed the 12V battery and all the Low Voltage (LV) loads (i.e., the 12V starter and the electrical oil pump for gearbox lubrication).

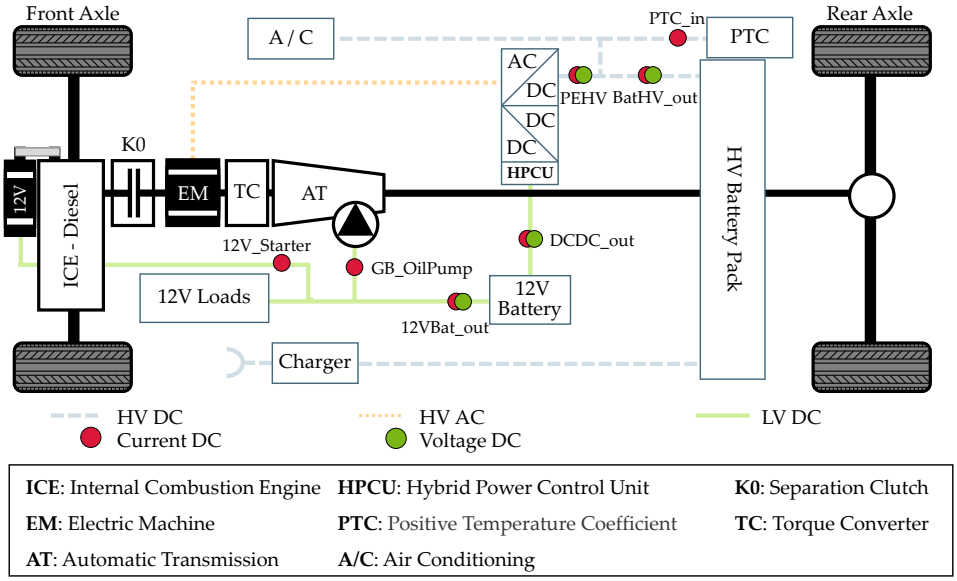

Fig. 5.2 Powertrain layout: a diesel engine is connected through an auxiliary clutch to an EM. Both the ICE and the EM are connected to the transmission by means of a torque converter.

Typically, a pHEV can operate in two different modes:

- Charge Depleting (CD):
  When the battery is sufficiently charged, the vehicle is mainly propelled in fully electric mode;
- Charge Sustaining (CS):
  When the battery SoC reaches a lower boundary, the ICE is used for propulsion and the SoC is maintained within a small window.

In the investigated vehicle, a Hybrid Power Control Unit (HPCU) is connected to the HV inverter, which handles the energy flows between the EM and the HV battery pack. The HPCU allows the driver to select between four different driving modes:

Table 5.1 Vehicle and powertrain main specifications.

Vehicle	Curb Weight [kg]	2060
	Power [kW] @ 100 km/h	14.9
Transmission	Type	9-AT w/ Torque Converter
ICE	Type	In-line 4 cylinders Turbo Diesel
	Displacement [cm^3]	1950
	Max Power [kW] @ 3800 rpm	143
	Max Torque [Nm] @ 1600-2800 rpm	400
	Compression Ratio	15.5:1
EM	Type	PM Synchronous Motor
	Max Power [kW] @ 2000 rpm	90
	Max Torque [Nm] @ 1750 rpm	440
	Max Speed [rpm]	6000
HV Battery	Type	Li-NMC
	Rated Voltage [V]	365
	Cacapity [kWh]/[Ah]	13.5/37
	Cooling System	Water Cooled

- Hybrid Drive:
  It is the default setting; the EMS autonomously decides the powertrain operating mode depending on the driving situation and the route profile;
- Electric Drive:
  This setting ensures zero local emissions because it is performed in CD mode; the power necessary to propel the vehicle is provided by the EM;
- E-Save Drive:
  This mode ensures the charge sustaining of the battery SoC, in order to allow the electric drive at a later stage; thus, the EM propels the vehicle in combination with the ICE;
- Charge Drive:
  This mode ensures that only the ICE propels the vehicle, while constantly charging the battery.

It is worth mentioning that during the test campaign, the hybrid drive was always selected so that the ECU of the vehicle autonomously decided the power split. In particular, two different operating modes are considered:

- EV Mode:
  The EM delivers all the required torque;

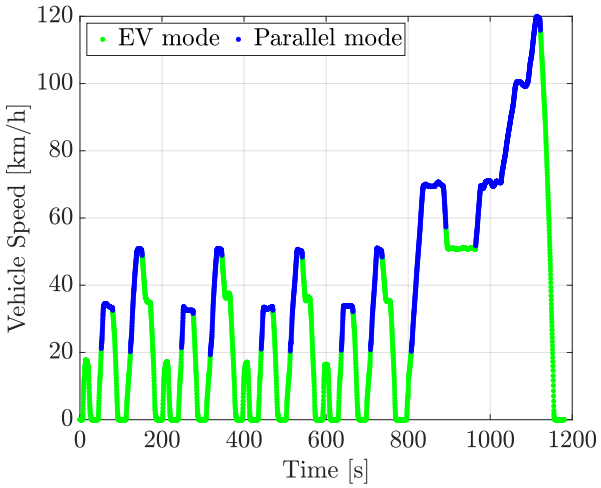

(a)

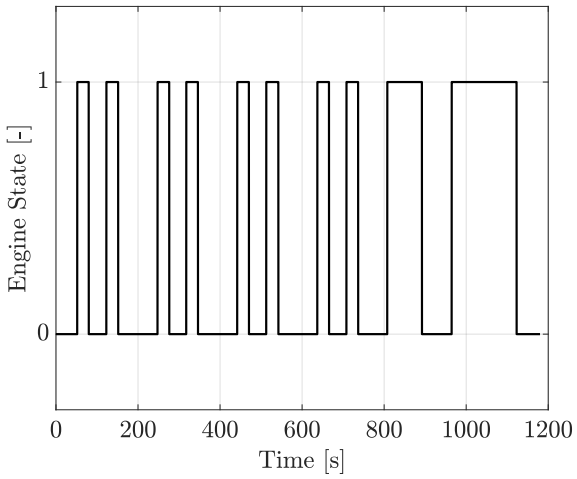

(b)

Fig. 5.3 Vehicle tested over the NEDC - (a): Vehicle speed profile along with the operating modes: EV mode (green) and parallel mode (blue) – (b): Engine state: 1 (on) and 0 (off).

- Parallel Mode:
  Both the ICE and the EM deliver the required torque.

The engagement of the clutch K0 between ICE and EM (see Figure 4.1) is chosen as a discriminator between the two modes. During the EV mode, the clutch is disengaged and the ICE is off, while during the parallel mode, the clutch is engaged and the ICE is coupled to the EM and the transmission. Figure 5.3 depicts the typical layout of the NEDC vehicle speed profile as a function of time, where the

Table 5.2 Characteristic values of the cycles performed during the experimental campaign.

Cycle	Time	Distance	Avg. Speed	Max Speed	Avg. Acc.	Max Acc.	Required Energy	Test Bench
	$[s]$	$[km]$	$[km/h]$	$[km/h]$	$[m/s^2]$	$[m/s^2]$	$[Wh/km]$	$[-]$
$NEDC$	1180	11	34	120	0.38	1.42	184	✓
$WLTC$	1800	23	47	131	0.41	1.84	222	✓
RDE_1	838	13	57	161	0.74	5.56	274	✗
RDE_2	4322	69	57	128	0.36	1.74	258	✗
RDE_3	4327	68	56	144	0.37	1.91	273	✗
RDE_4	6657	89	48	126	0.30	1.68	207	✓
RDE_5	6666	89	48	126	0.29	1.69	215	✓
RDE_6	5926	97	59	139	0.38	3.41	225	✗
RDE_7	5532	97	63	138	0.35	4.22	223	✗

parallel and EV modes are represented with blue and green points, respectively. The above-mentioned classification will be used hereinafter, but it should be noted that it is just a preliminary differentiation between the operating modes; more details about power split, load point moving, e-assist, etc., will be discussed in the following paragraphs.

5.1.2 Experimental Campaign

The vehicle was tested during an extensive experimental campaign. Most of the tests were carried out on an All-Wheel Drive (AWD) chassis dynamometer, but some additional measurements were performed in real-world scenarios, equipping the vehicle with a Portable Emissions Measurement System (PEMS), as described in detail in [147].

The characteristic values of the most representative cycles performed during the experimental campaign are shown in Table 5.2. As far as regulatory driving cycles are concerned (i.e., NEDC and WLTC), measurements were performed on the chassis dynamometer following the type-approval procedure [148]. For a pHEV, the guidelines defined in the UNECE Regulation 83 require two tests [5]:

- Condition A:
  At the beginning of the test, the HV battery must be fully charged;

Table 5.3 Trip composition of the RDE_7.

Section	**Duration**	**Distance**	**Distance Share**	**Average Speed**
	$[s]$	$[km]$	$[\%]$	$[km/h]$
Urban	3067	30.4	31.5	33.9
Rural	1405	31.0	32.2	76.1
Motorway	1060	35.1	36.4	113.9
Total Trip	5532	96.4	[-]	63.1

- Condition B:
  At the beginning of the test, the HV battery must be fully discharged.

According to the Regulation, Condition B was repeated both featuring a hot engine (i.e., immediately after Condition A) and a cold engine (i.e., performed one day after Condition A). The Real Driving Emissions (RDE) cycles, instead, were performed to fully characterize the powertrain control logic. As shown in Table 5.2, some cycles were conducted on the test bench by following real-driving mission profiles, while others were conducted on public roads on the outskirts of the Italian city of Turin (denoted with the ✗ symbol in Table 5.2). The experimental campaign allowed us to test the vehicle in a wide spectrum of driving conditions.

By way of example, the RDE_7 is illustrated in Figure 5.4, along with its vehicle speed plotted as a function of time. It is a pre-defined RDE-compliant route [149], and it will be used as a test case in the following Sections. The route, shown in Figure 5.4a, was obtained from Portable Emissions Measurement System (PEMS) and combined with a topographic map. It lasts approximately 92 minutes and is 96 kilometers long. In the test, a rural and a motorway operation follow the urban one, involving mild uphill and downhill sections and the trip composition is summarized in Table 5.3. In an RDE-compliant cycle, like this one, each section, i.e., urban, rural, and motorway, must cover a distance higher than 16 km, while the distance share must be contained in the (23–43)% range, for the rural and motorway sections, and in the (29–44)%, for the motorway one.

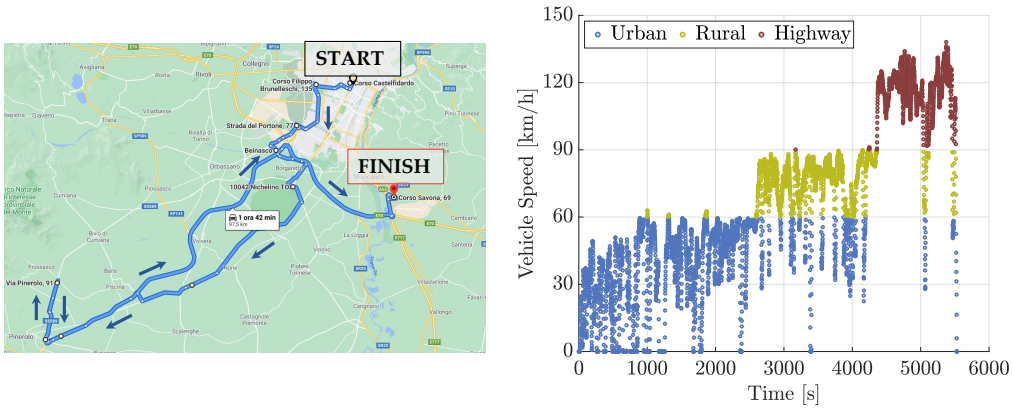

(a) (b)

Fig. 5.4 RDE_7 - (a) Vehicle position obtained from PEMS and combined with a topographic map (Courtesy of Google Maps). The route lasted approximately 92 minutes and was 96 kilometers long; (b) Vehicle speed as a function of time divided into urban, rural, and highway sections.

5.1.3 Reverse Engineering

The hybrid powertrain was fully characterized without performing a complete vehicle teardown. The Controller Area Network (CAN)-bus protocol, the On-Board Diagnostic (OBD) system, and additional sensors installed in strategic locations were used to collect data. For a detailed description of the vehicle instrumentation see [147]. The ICE was characterized in terms of Brake Specific Fuel Consumption (BSFC) maps, while the EM was characterized by combining the measurements of the electrical energy on the DC side with data available from the CAN-bus protocol. The torques and rotational speeds of ICE and EM were acquired from CAN. In fact, because of the system complexity and the huge effort required in the data acquisition, the EM was not instrumented. The maps used for modeling ICE and EM are shown in Figure 5.5. The engine BSFC is interpolated from the map reported in Figure 5.5a, as a function of engine speed and BMEP, while the EM losses are reported in Figure 5.5b as a function of speed and power.

Also for the HV battery, it was not possible to perform a detailed characterization of the battery chemistry. During the experimental campaign, a wide range of battery SoC, current, and voltage was explored by performing charge-discharge cycles to characterize the battery OCV and the internal resistance. The battery was modeled by means of an ECM, whose parameters are plotted in Figure 5.6 as a function of SoC. Since the EMS of the actual vehicle could not be accessed, the SoC variable

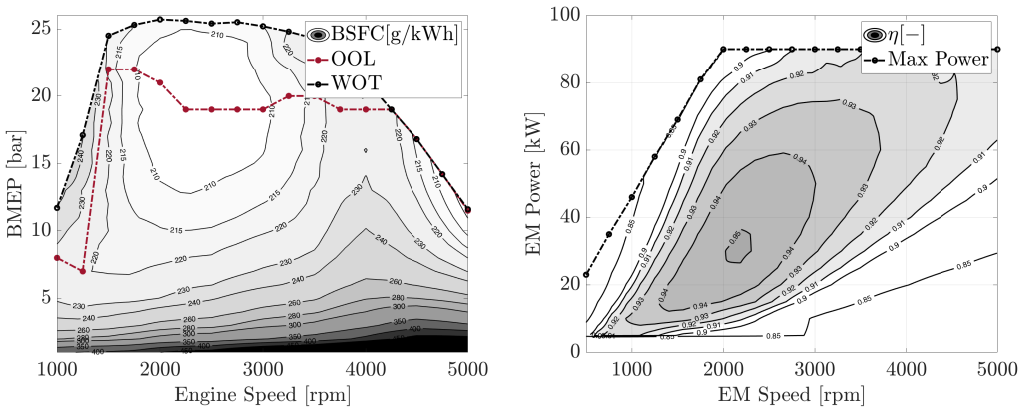

(a) (b)

Fig. 5.5 (a): BSFC of the Internal Combustion Engine; (b): Efficiency of the Electric Machine.

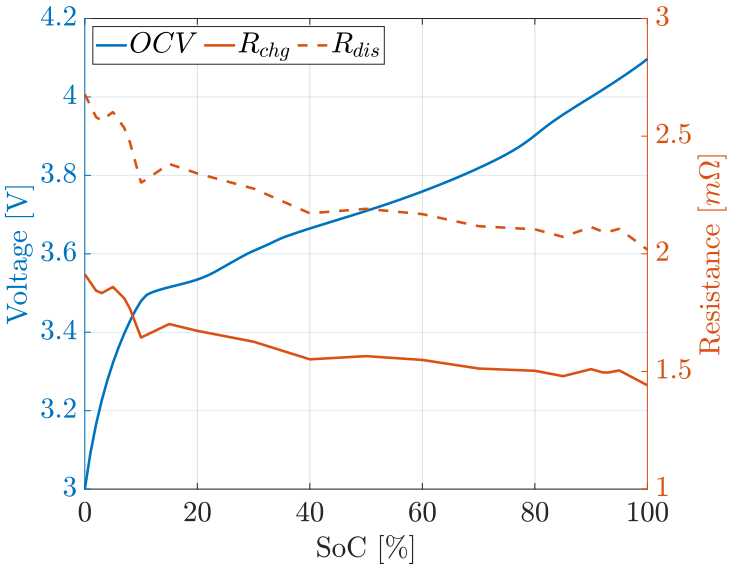

Fig. 5.6 High-voltage battery cell data: internal resistance in charge and discharge (orange line) and OCV (blue line) as a function of SoC.

used for the analysis is the dashboard displayed value which was acquired from the CAN network. Hence, the SoC varies in the range of 0-100% and is an indication of the actual energy capacity available to the user.

This Section focuses on the methodology carried out for reverse engineering the control strategy implemented in the hybrid powertrain without direct access to the EMS, and without a detailed characterization of the ICE, the EM, and the HV battery. The data coming from the experimental campaign described in Section 5.1.2 were

carefully analyzed and post-processed in order to extract the strategy adopted by the EMS, pointing out any dependency of its decisions on the main powertrain operating variables.

GPS Information Dependency

According to the car manufacturer, the vehicle EMS employs an intelligent operating strategy that takes into account navigation data, topography, speed limits, and traffic conditions of the planned route, in order to activate the electric driving mode when it is most appropriate [150]. RDE_2 and RDE_3 are specific tests aimed at assessing the reliance of the EMS decisions on the Global Positioning System (GPS) information: they feature the same real-world route with the vehicle navigation system alternatively switched ON and OFF. Figure 5.7a represents the RDE_3 (navigation system switched OFF), while Figure 5.7b represents the RDE_2 (navigation system switched ON). In both plots, the vehicle speed is plotted as a function of distance highlighting the operating modes, along with the battery SoC profile. When the navigation system is OFF, more than 40 km are covered in CD phase, leading to an almost linear SoC depletion. The ICE is switched ON only when the power requested by the driver exceeds the max performance of the EM. On the contrary, when the navigation system is ON, the EMS changes its strategy ensuring that the last stage of the journey (the urban one) can be covered in all-electric mode. As illustrated in Figure 5.7b, although the battery is fully charged at the beginning of the test, the highway section is performed in parallel mode, and the battery SoC remains almost constant. Then, the urban section is performed in EV mode, and the battery SoC is linearly depleted. Nevertheless, the battery is not fully discharged at the end of the test, and the hybrid potentiality is not fully exploited.

More details can be obtained from Figure 5.8. It depicts, during the highway section, the vehicle speed as a function of time highlighting the operating modes, along with the power delivered by the ICE and the EM. As evident from Figure 5.8a, when the navigation system is switched OFF, the ICE is started only when the power requested by the driver exceeds the max performance of the EM. On the contrary, as illustrated in Figure 5.8b, when the navigation system is switched ON, the highway section is almost entirely performed in parallel mode (the EM propels the vehicle only during low speed and acceleration phases). Moreover, when the ICE is switched on, the vehicle is propelled in ICE-only mode, e.g., in the interval 650-1100s, and the power delivered by the EM is almost null.

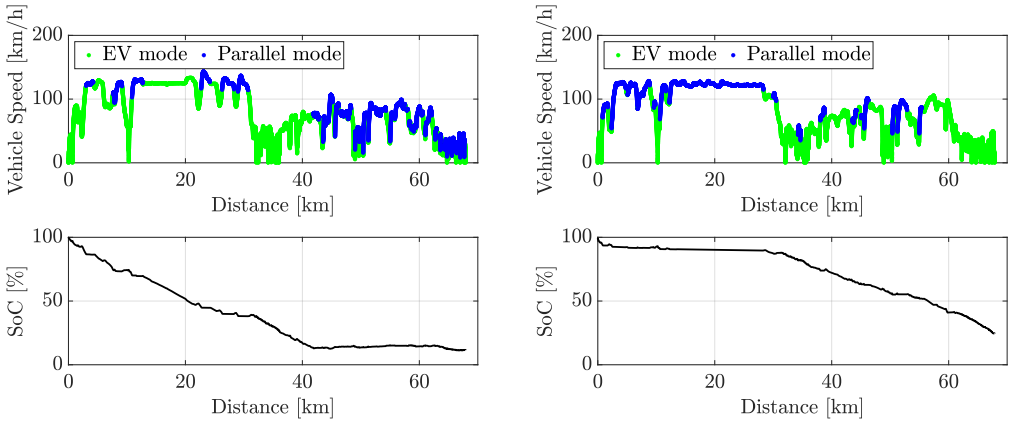

(a) (b)

Fig. 5.7 Above: Vehicle speed plotted as a function of distance highlighting the operating modes: EV mode (green) and parallel mode (blue) – Below: Battery SoC profile as a function of distance. (a): GPS OFF; (b): GPS ON.

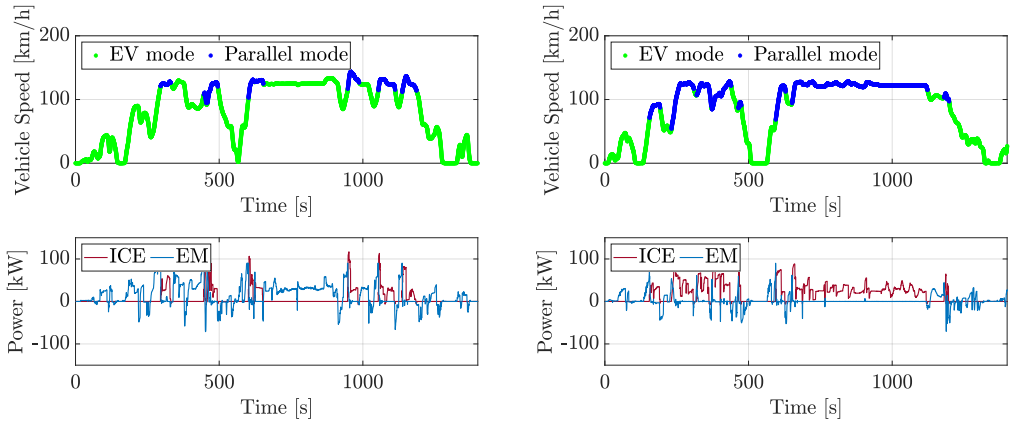

(a) (b)

Fig. 5.8 Above: Vehicle speed plotted as a function of time highlighting the operating modes: EV mode (green) and parallel mode (blue) – Below: ICE and EM power profiles plotted as a function of time. (a): GPS OFF; (b): GPS ON.

Figure 5.9, instead, displays the trade-off between CO_2 emissions and final SoC values for the two cases with the navigation system alternatively switched ON and OFF. When the navigation system is ON, although the EMS employs an intelligent operating strategy that activates the electric driving mode when it is most appropriate, it does not employ all the electrical energy stored on board since the battery is not fully depleted at the end of the driving cycle. This leads to higher CO_2 emissions if compared to the case with the navigation system switched OFF, which, on the contrary, completely discharges the battery at the end of the driving cycle. Therefore,

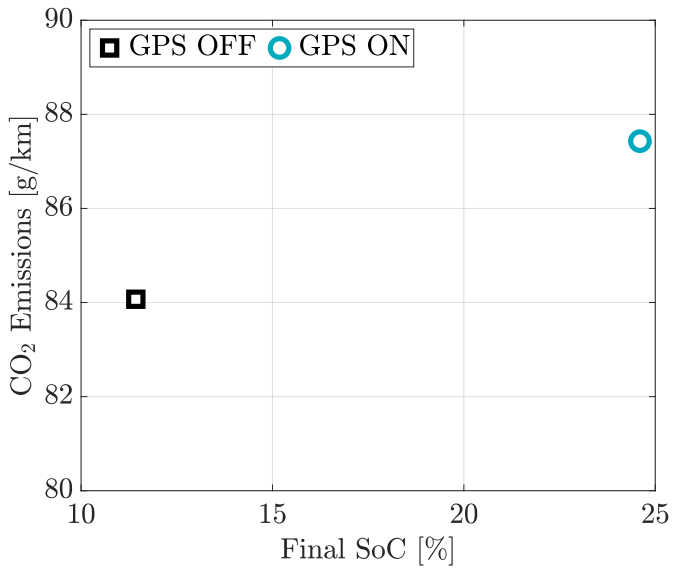

Fig. 5.9 Tradeoff between CO_2 emissions and final SoC with GPS ON (blue circle) and OFF (black square).

the comparison between the two strategies is not meaningful due to the different depths of discharge, and the real potential of the intelligent operating strategy, in terms of fuel savings, cannot be fully assessed given the limited dataset available.

Normal Operation

The current work aims to build a virtual test rig that can reproduce the vehicle behavior in normal operation. Some particular conditions entailing variations in the rules followed by the EMS will not be taken into account henceforth, e.g., the missions where the driver communicates the vehicle route to the EMS through the GPS navigation system, or the type-approval procedure featuring a cold engine (i.e., the cycle performed one day after Condition A).

If the battery at the beginning of the mission profile is fully or partially charged, the vehicle is propelled in EV mode (some exceptions will be seen in Section 5.1.3). The parallel mode is enabled only when the battery reaches low values of the SoC. Figure 5.10 shows the WLTC repeated several times according to the Regulation [5], where the colors follow the convention explained in Section 5.1.1. The vehicle performs twice the WLTC in EV mode (marked with a dashed area), and the ICE is switched on only at the end of the second cycle. The following Sections will analyze, more in detail, the rules followed by the control logic in CD and CS conditions. For

the sake of simplicity, the rules will be mainly shown on the WLTC, although also the other cycles were used in the overall procedure followed to extract them.

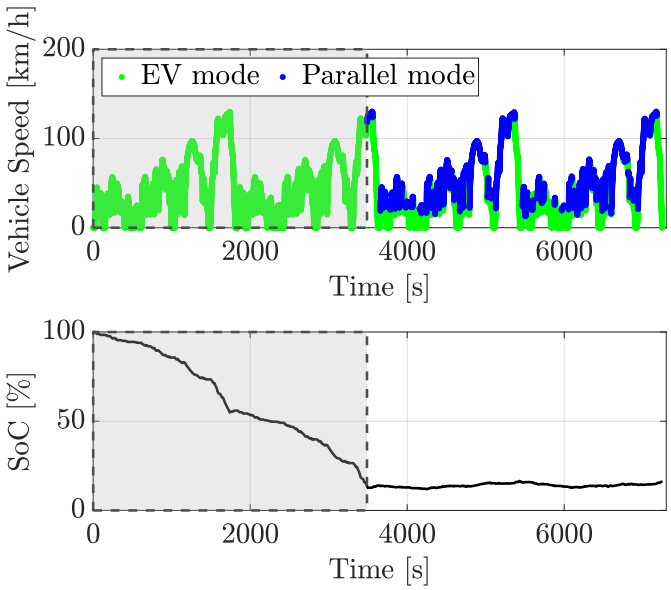

Fig. 5.10 WLTC repetitions according to the Regulation [5] - Above: Vehicle speed profile plotted as a function of time highlighting the operating modes: EV mode (green) and parallel mode (blue) – Below: Battery SoC profile as a function of time. The dashed area highlights the section performed in CD mode.

Rules in Charge Depleting

As already mentioned, if the battery at the beginning of the mission profile is fully or partially charged, the EMS chooses a CD strategy. From the analysis of the WLTC repetitions (black box in Figure 5.10), it can be noted that all the CD phase is carried out in EV mode: the ICE is never switched on and the EM delivers all the required power. A different behavior can be seen for the RDE_3 test (represented in Figure 5.11): also during the CD phase, the ICE is switched on (red dots) if higher loads are required.

A more granular analysis can be done from Figure 5.12, where all the EM operating points are plotted on its efficiency map. The same color convention of Figure 5.3 is adopted, i.e., green, blue, and red denote EV mode, parallel mode, and ICE switching on, while all the gray dots represent the transition phases during which the engine and the clutch engagement status are changing. It is eye-catching that, during the CD phase, the ICE is usually switched on (red dots) when the EM reaches its max performance. Moreover, in parallel mode, once the ICE is switched

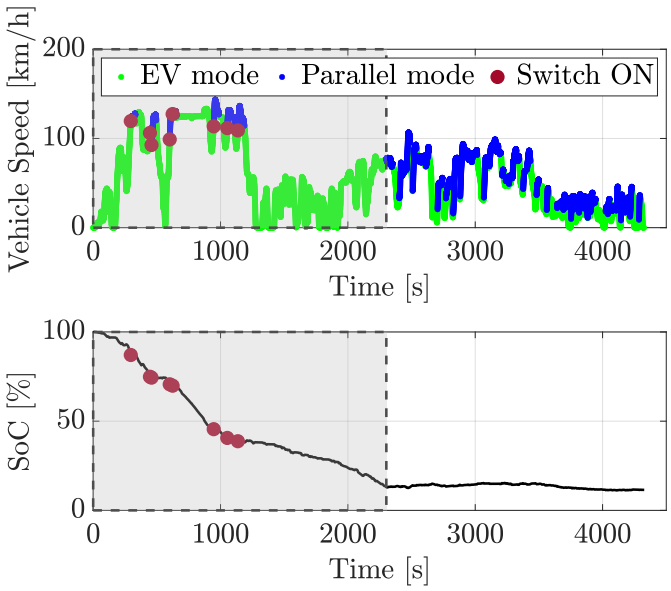

Fig. 5.11 RDE_3 - Above: Vehicle speed profile along with the operating modes: EV mode (green) and parallel mode (blue) – Below: Battery SoC profile as a function of time. The ICE switching on during the CD phase is denoted with red dots.

on, the EM spends most of the time at very low loads, implying that the vehicle is operating in a pure ICE drive.

The same behavior can be more clearly understood from Figure 5.13, where the EM power is plotted as a function of the powertrain power. As expected, all the green points lay on the bisector: thus, in EV mode, all the power is provided by the EM. In parallel mode, however, the behavior is surprising: most of the blue points lay on the x-axis. Thus, in parallel mode during the CD phase, the driver power request is almost totally fulfilled by the ICE.

Rules in Charge Sustaining

As evident from Figures 5.10 and 5.11, it can be noted that there is a turning point causing a switch from CD to CS mode. Indeed, from the analysis of the SoC trajectory over different mission profiles, it may be deduced that the EMS uses an SoC threshold of about 13%, for switching from CD to CS mode.

During the CS phase, since the energy must be ultimately provided by the ICE, the control strategy drastically changes if compared to the CD phase. Figure 5.14 shows the WLTC performed during the CS phase, where all the engine switch on and off are depicted (red and blue bullets, respectively) on the vehicle speed profile.

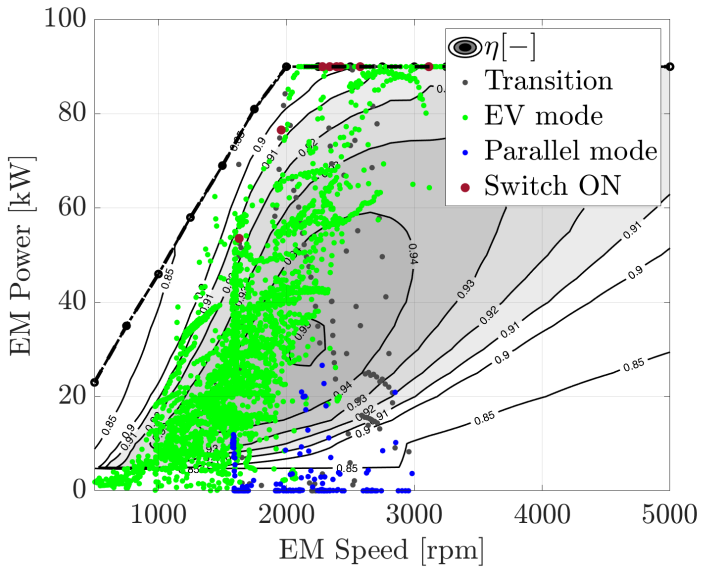

Fig. 5.12 *RDE*$_3$ - EM working points in speed (x-axis) power (y-axis) map and full-load curve. Green dots: EV mode; blue dots: parallel mode; red dots: engine switching on; grey dots: transition phases, i.e., the engine status and the clutch engagement are changing.

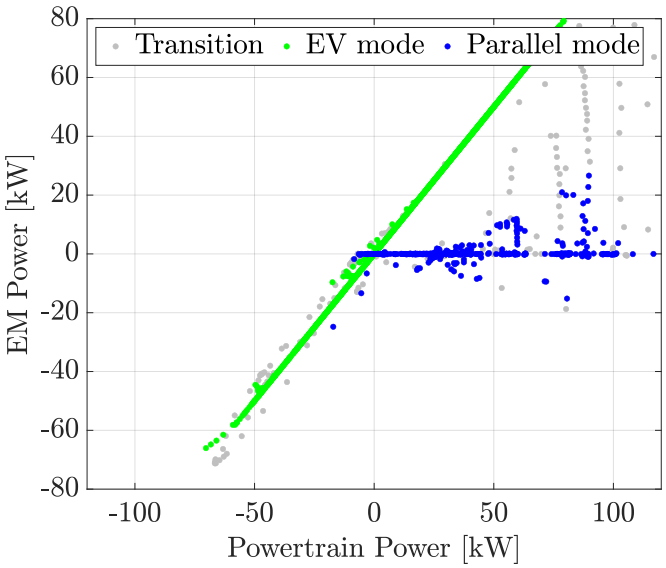

Fig. 5.13 *RDE*$_3$ - EM power plotted as a function of the powertrain power. Green dots: EV mode; blue dots: parallel mode; grey dots: transition phases, i.e., the engine status and the clutch engagement are changing.

Some meaningful variables were analyzed in order to highlight some threshold values determining the engine switch on or off. From Figure 5.15 (above), where all the engine ignition points during the WLTC are plotted as a function of the vehicle

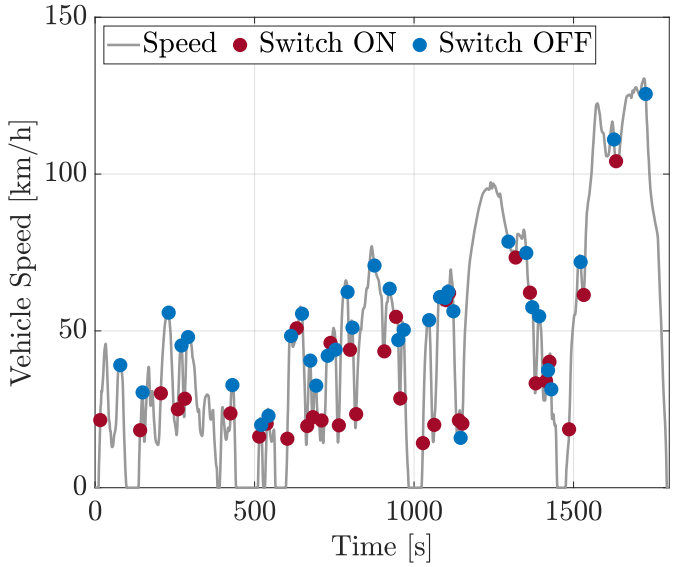

Fig. 5.14 WLTC performed during the CS phase, where all the engine switch ON and OFF are depicted (red and blue bullets, respectively) on the vehicle speed profile.

acceleration and speed, a clear pattern (hyperbola branch) can be identified. As expected, the higher the acceleration required by the driver the lower the vehicle speed threshold for ICE switching on. Similarly, Figure 5.15 (below) depicts all the engine shutdown points (always for the WLTC) plotted as a function of powertrain torque and vehicle acceleration. These two variables seem to be correlated through a linear trend because the lower the torque required by the driver the higher the vehicle deceleration threshold for ICE switching off. This control rule may be implemented for safety reasons since the combinations of engine inertia, pumping, and friction losses can provide additional braking power to the drivetrain that may be helpful during higher decelerations. Some additional constraints were observed on the minimum time for the engine to stay on and off: for all the investigated cycles it was observed that the ICE stayed on for at least 5 seconds and off for at least 4 seconds.

As already done for the CD mode, a more specific analysis was conducted to characterize the power split in CS mode. Figure 5.16 depicts all the engine operating points during the WLTC as a function of the torque delivered by the powertrain (ICE+EM) and the torque delivered by the ICE. The points that lay on the red line ($P_{ICE} = P_{PWT}$) represent an ICE-only mode; above the red line, the powertrain operates in Load Point Moving (LPM), i.e., the ICE works at higher loads to allow battery recharging; under the red line, an e-boost is performed. As evident from Figure 5.16, the ICE works most of the time in the LPM zone, boosting the battery

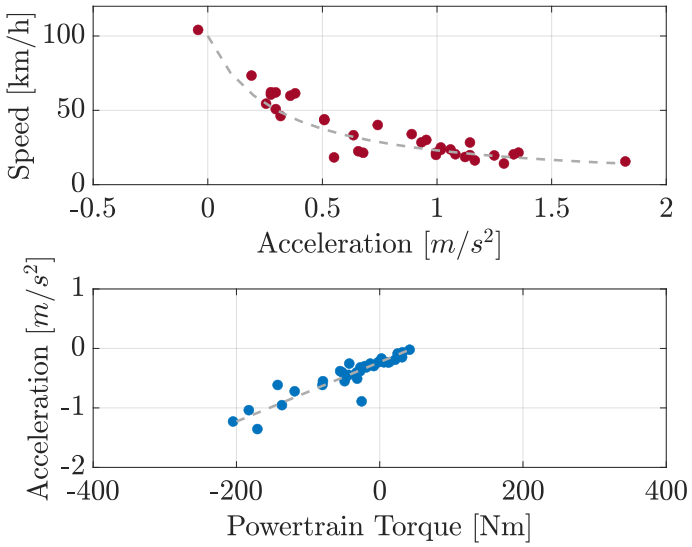

Fig. 5.15 Mapping of engine switching on and off during a WLTC - Above: Engine switch-on points as a function of vehicle acceleration and speed – Below: Engine shutdown points as a function of powertrain torque and vehicle acceleration.

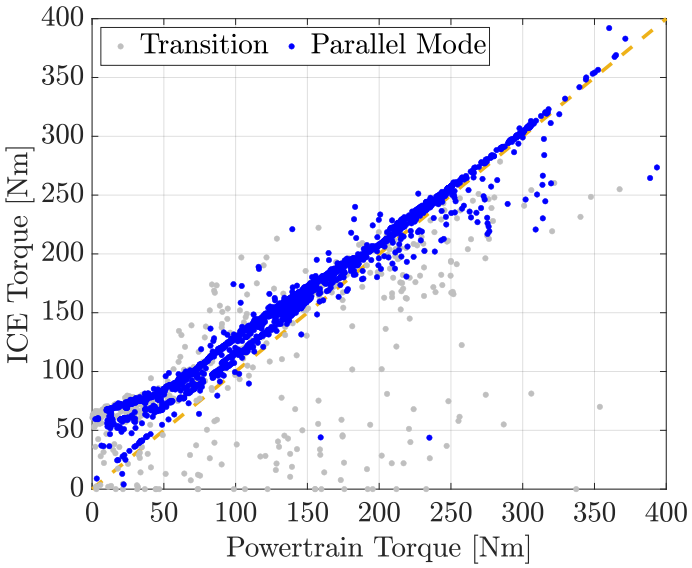

Fig. 5.16 WLTC – ICE torque represented as a function of the total powertrain torque. Blue dots: parallel mode; grey dots: transition phases, i.e., the engine status and the clutch engagement are changing.

recharge. This allows compensation of the energy provided by the battery in EV mode, to reach charge sustainability at the end of the cycle. On the contrary, an

e-boost is almost never performed since, as already mentioned, all the grey points represent only transitional phases.

An almost linear relationship can be identified between the torque delivered by the ICE and the total torque delivered by the powertrain. In particular, the lower the requested power, the bigger the shift of the engine operation toward higher loads. This may be performed to counterbalance the BSFC worsening at low ICE loads. From a more granular analysis, however, the rule governing the torque split during the CS phase appeared to change according to the SoC trend. This behavior can be more clearly understood from Figure 5.17, where different sections of the WLTC are analyzed separately depending on the SoC values. Specifically in sections 1 and 4, marked by blue and red boxes, respectively, the SoC is higher than 15%, while in sections 2 and 3, marked by yellow and green boxes, respectively, lower than 13%.

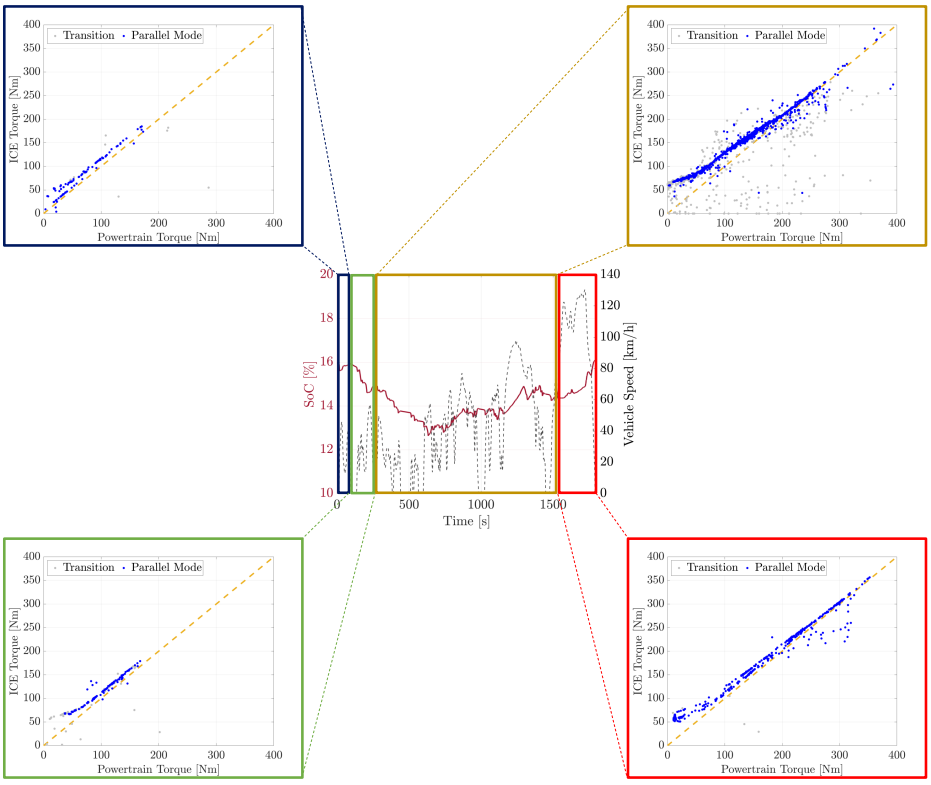

Fig. 5.17 WLTC subdivision in different time intervals depending on the SoC values. For each section, the correspondent torque split law is shown.

It seems that different relationships between the ICE and the total torque can be highlighted depending on SoC values. In fact, if the SoC is above the mentioned threshold (sections 2 and 3), the torque delivered by the engine appears to be closer

to the red line (apart from section 1 where a different behavior may be attributed to the engine warm-up). As a consequence, the ICE power exceeding the traction request, thus available for battery recharging, is quite limited, and for this reason, this rule will hereafter be referred to as the "weak rule." On the other hand, when the SoC is below the mentioned threshold (section 3), the torque split between ICE and EM seems to follow a different rule, with a higher deviation from the red line. As a consequence, a higher ICE power is available for battery recharging, and for this reason, this rule will hereafter be referred to as the "strong rule". For the sake of clarity, Figure 5.18 shows an enlargement of the two rules governing the torque split, i.e., the abovementioned "weak" and "strong" rules. The evidence from all the analyzed cycles suggests that the observed strategy that decides the torque split in the CS phase is aimed at guaranteeing charge sustainability while keeping the SoC in the range of 13%-15%.

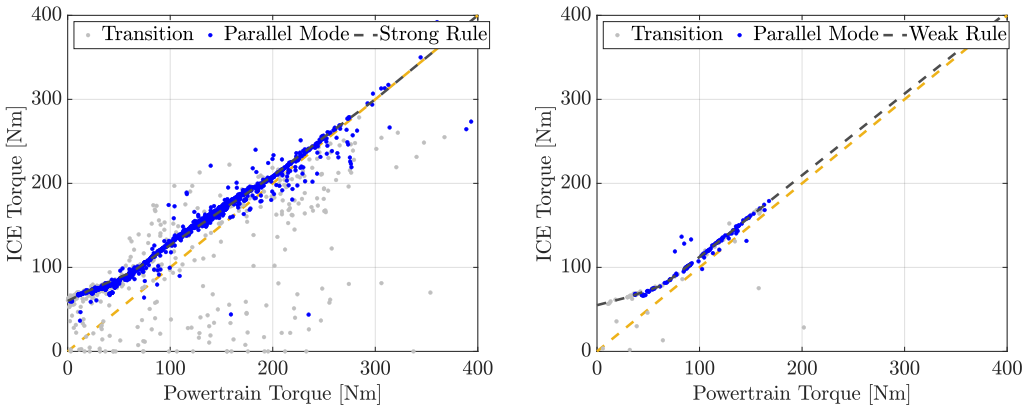

Fig. 5.18 Extraction of the rules governing the torque split - (a): "weak rule" entailing softer recharge of the battery – (b): "strong rule" entailing stronger recharge of the battery.

Rule-Based Supervisory Controller

The rules extracted in the previous Sections have been summarized in Figure 5.19. Although the control strategy implemented in the actual vehicle could be more complex, the flowchart explains quite well the overall behavior of the rule-based strategy. "Rule ON" and "Rule OFF" are the thresholds for switching on and off the engine; they were described in Section 5.1.3 and are represented in Figure 5.15. The minimum SoC that can be reached in CD operation triggering the passage from CD to CS operation is equal to 13%. The max SoC value for CS operations (i.e.,

the system exits from CS operation as soon as the SoC reaches this value) is 20%. In summary, if the battery is fully or partially charged, the vehicle operates in EV mode (i.e., only the EM provides the required power). If the power request exceeds the max EM capacity, the ICE is switched on, and the vehicle operates in parallel mode until the rule governing the ICE switching off is not triggered. This rule does not differ too much from the one governing the CS phase illustrated in Figure 5.15. When the battery SoC reaches a value of 13%, it triggers the passage from CD to CS strategy. In CS operation, the ICE is switched on according to the law shown in Figure 5.15, and is switched off according to the rule illustrated in Figure 5.15. Finally, through the combination of an LPM strategy (see Figure 5.18) and an additional condition inhibiting the ICE switching on above a certain SoC threshold, the charge sustainability is guaranteed.

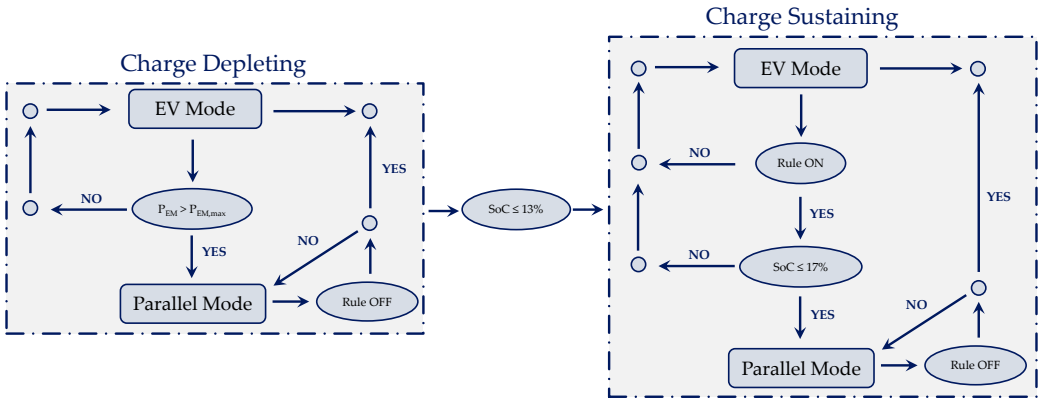

Fig. 5.19 Flowchart describing the overall behavior of the rule-based strategy extracted from the actual vehicle.

5.1.4 Validation

Vehicle Modeling

As shown for the WLTC, the procedure described in the previous Sections was carried out on the other driving cycles to obtain a set of comprehensive rules, capturing the vehicle behavior in a wide range of driving conditions. The extracted rules were used to build a virtual test rig of the tested vehicle. The model was developed in the GT-SUITE® [151] software environment using a quasi-static approach (see Section 4.2.3): the virtual vehicle driver compares the actual vehicle speed to a target one and generates a power demand profile to follow the target speed. The code computes

the actual vehicle speed by solving the longitudinal vehicle dynamics, while fuel consumption is calculated based on steady-state performance maps. The powertrain parameters along with the performance maps are described in Sections 5.1.1 and 5.1.3. Regarding the HV battery, it was modeled as a simple ECM. Knowing its chemistry, i.e., Li-NMC battery technology, the OCV, and the internal resistance were modeled, as a function of the cell SoC and temperature, using data available in the scientific literature [152, 153] as a starting point. Then, the model parameters were experimentally tuned by matching the experimental charge-discharge tests. Finally, the RB control strategy was implemented in the Simulink® environment and then coupled with the GT-SUITE vehicle model. The ICE switching on and off is governed by the rules presented in the previous Section, while a weighted average of the two LPM laws, based on the instantaneous battery SoC, is implemented to introduce a smooth transition between strong and weak conditions (see Figure 5.18).

In order to properly estimate the amount of energy recovered through regenerative braking and consequently replicate the experimental SoC trajectory, it is of paramount importance to capture the powertrain contribution to the vehicle braking system. In a hybrid vehicle, during braking maneuvers, the braking control logic depends on comfort and safety levels, and on the battery current limits. In particular, for a rear-wheel drive configuration, such as the test case, particular attention should be paid to vehicle dynamics since the EM contributes to the rear axle braking. The braking system was modeled through static maps, experimentally obtained in [147], where the braking power ratio, i.e., regenerative braking power over total braking one, is expressed as a function of vehicle speed and acceleration. As already mentioned, the virtual test rig was aimed at reproducing the vehicle behavior in standard driving. Some particular conditions entailing variations in the rules followed by the EMS were not taken into account.

Model Validation

The model validation was mainly carried out along the regulatory driving cycles, but, in order to prove its capabilities in predicting the vehicle behavior also in a real-driving scenario, the model validation will be only shown for the RDE_7 cycle. It should be added that, in order to give more robustness to the model validation, this cycle was not included in the procedure followed for reverse engineering the vehicle control strategy. Figures 5.20 and 5.21 show the simulation results (red line)

Table 5.4 Comparison between experimental data and simulation results for the battery final SoC and the vehicle CO_2 emissions over the RDE_7

CO_2 **Specific Emissions** $[g/km]$		**Final SoC** $[\%]$	
Exp	Sim	Exp	Sim
95	96 $+1.0\%$	19	18 -4.7%

compared to the experimental measurements (black dashed line), with the plots on the right representing an enlargement of the highlighted area on the left.

Figures 5.20a and 5.20b display the vehicle speed profile: despite being a dynamic model, i.e., the speed is not imposed but seen as a target, the model results excellently match the experimental value, even during erratic speed variations. Figures 5.21a and 5.21b prove that the ICE rotational speed is well captured over the entire cycle, and, apart from some occasional cases, the model correctly predicts the ICE on and off events. Moreover, as evident from Figure 5.20e, the transition from CD to CS mode is well captured. Although the cycle is highly transient, the operating points of ICE and EM are correctly reproduced in terms of speed and load. As a result, the battery SoC profile – Figures 5.20e and 5.20f – show a remarkable agreement with the measured data: for the majority of the trip, the difference between measurement and simulation lies within the ±5% limit.

Figures 5.20 and 5.21 prove the robustness of the strategy obtained from the reverse engineering of the actual vehicle. Furthermore, the limited errors in both the battery final SoC and the total vehicle CO_2 emissions (see Table 4) prove the reliability of the vehicle model in reproducing, in a virtual environment, the behavior of the actual vehicle. Although the final SoC discrepancy may appear quite significant (4.7%), it should be noted that this value is almost negligible (0.44%) if compared with the energy required for the entire driving cycle: less than 0.1 kWh over 21.6 kWh. Hereinafter, the extracted control logic will be indicated as RB and will be used as a reference for the assessment of the performance of the advanced control energy management strategies.

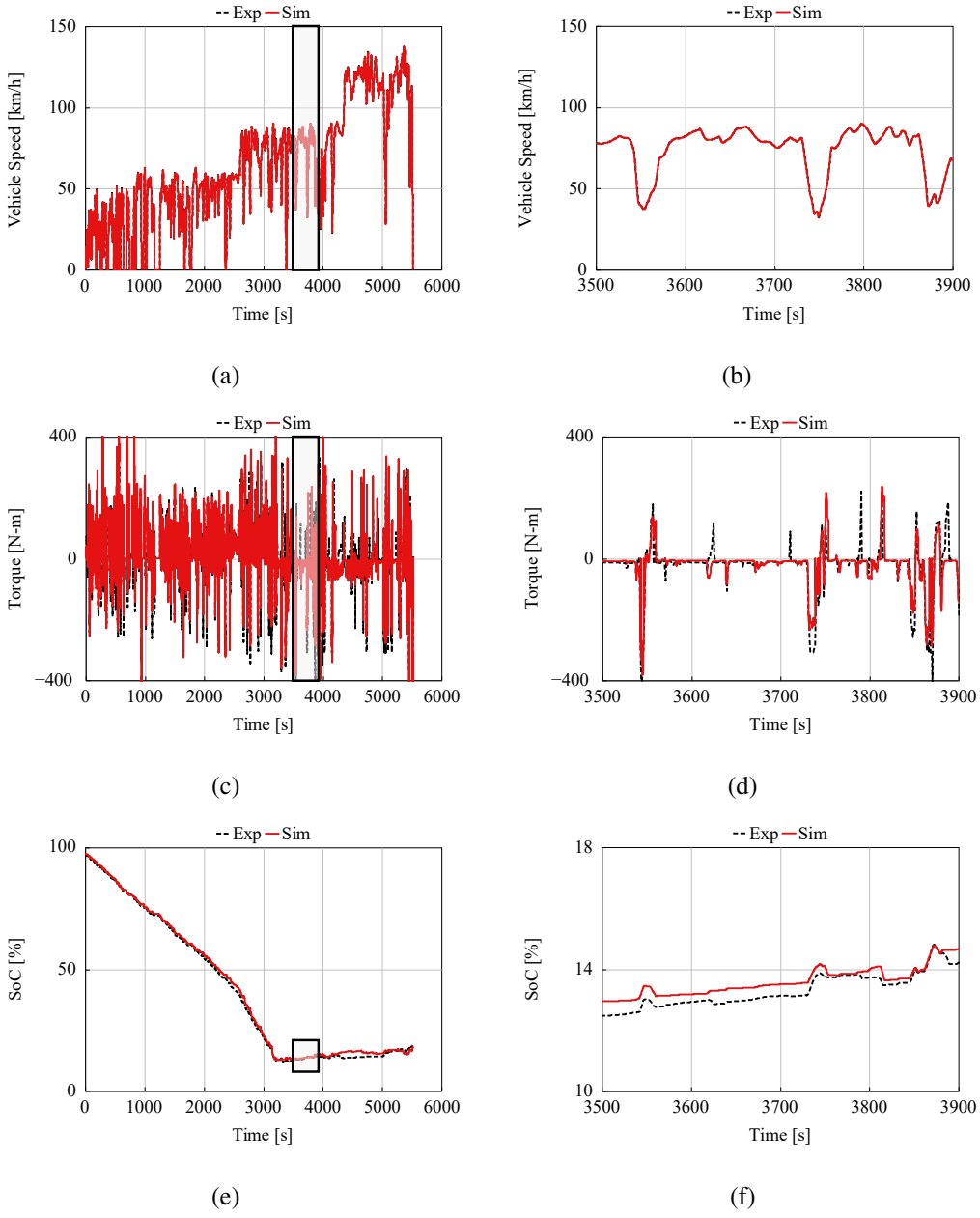

Fig. 5.20 Comparison between numerical simulation (red line) and experimental measurements (black dashed line) for the RDE_7 – (a) (b): Vehicle speed – (c) (d): EM torque; (e) (f): Battery SoC. The plots on the right represent an enlargement of the highlighted area on the left.

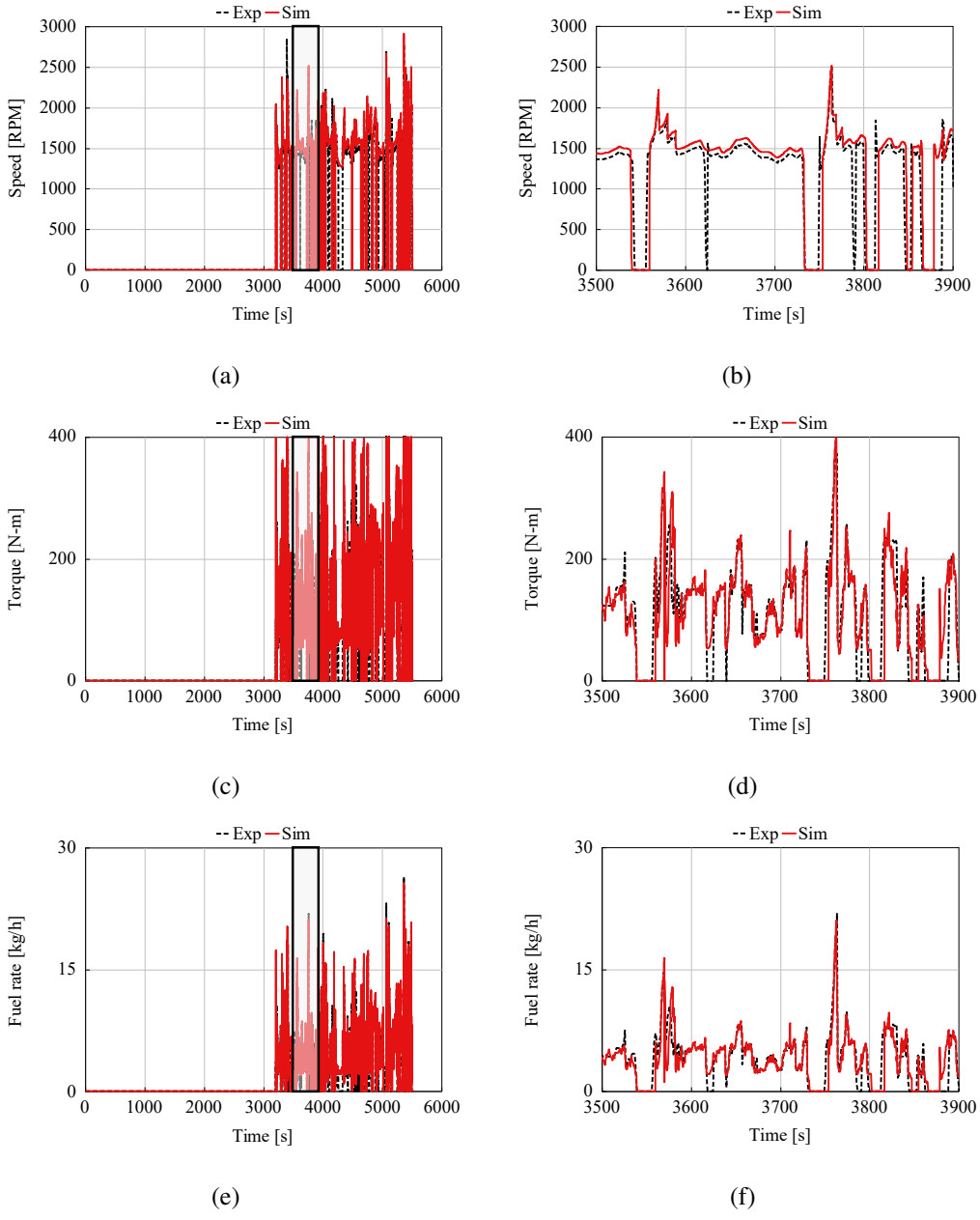

Fig. 5.21 Comparison between numerical simulation (red line) and experimental measurements (black dashed line) for the RDE_7 – (a) (b): ICE speed; (c) (d) ICE torque; (e) (f) Fuel rate. The plots on the right represent an enlargement of the highlighted area on the left.

5.2 Vehicle Speed Optimization

As already mentioned, the development of the virtual test rig was aimed at obtaining a high-fidelity test bench in which several optimization analyses could be performed. The first analysis was aimed at assessing the theoretical benefits that the introduction of V2V and V2I communication can have, in a real-world route, in terms of energy and time savings. With the recent advances in ITS technology that could empower vehicles to share information with the surrounding environment, vehicles can have realistic information about speed limits and Expected Time of Arrival (ETA). In this context, a Variable Grid Dynamic Programming (VGDP) is proposed which by modifying the variable state search grid on the basis of the V2X information allows a drastic reduction in the DP computation burden by more than 95% if compared to the standard optimization performed with a fixed grid. For this analysis, a simplified version of the vehicle model, relying on a backward kinematic model (see Section 4.2.2) was developed in MATLAB®. Moreover, since this analysis was focused at the vehicle level, the energy is minimized and powertrain agnostic results are obtained, i.e., adaptable for each type of vehicle: ICEV, HEV, pHEV, BEV, etc.

5.2.1 Scenarios Generation

The cycle selected as the Reference Scenario is the RDE_7, a pre-defined RDE-compliant route [149], while the simulation scenarios are generated by assuming two different levels of penetration of V2X technologies. Scenario #1 was designed supposing that a global optimization algorithm can choose the vehicle speed in the real-world mission profile, still respecting all the full stops imposed by traffic and/or infrastructure. Thus, starting from the Reference Scenario, several intersections, regulated by a stop sign, were introduced every time the vehicle comes to a full stop. As depicted in Figure 5.22a, it is assumed that the vehicle can have full access to infrastructure and traffic information. As shown in Figure 5.23, the optimizer is allowed to range in a vehicle speed window that takes into account the effects of speed limits and mild traffic conditions in a realistic scenario. Specifically, the upper and lower boundaries were obtained, starting from the speed profile of the Reference Scenario, by applying a moving average of $\pm$ 20 km/h over a section of 500 meters. It should be noted that the upper boundary never exceeds 135 km/h, and both the upper and lower ones merge to zero whenever a full stop sign is introduced.

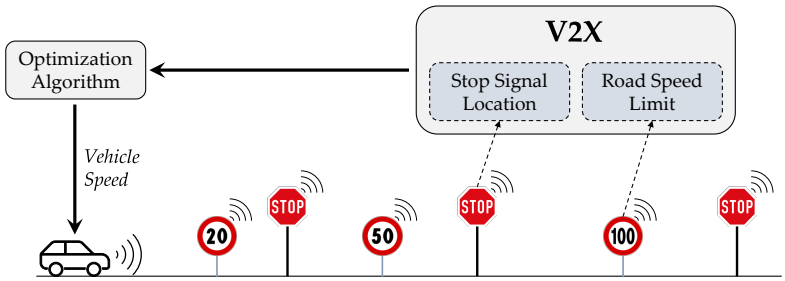

(a)

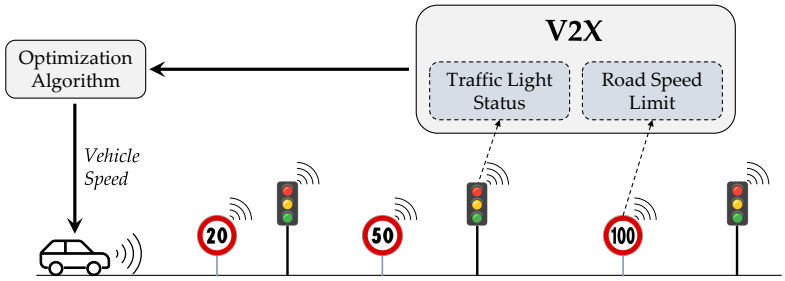

(b)

Fig. 5.22 Scenarios generation - (a): Scenario #1: generated starting from the Reference Scenario and assuming an intersection regulated by a stop sign every time the vehicle comes to a full stop; – (b): Scenario #2: generated starting from Scenario #1 and converting all the stop signs into traffic lights.

Scenario #2 was designed starting from Scenario #1 and converting all the stop signs into smart traffic lights. The duty cycle of the traffic lights was chosen following the guidelines provided for urban areas in [154]: cycle lengths of 60–90 seconds and a 3:2 ratio (for the amount of green time) are suggested to improve pedestrian compliance and decrease congestion on surrounding streets. Following these guidelines, the traffic lights were modeled through square waves with a period of 1 minute and a green phase of 60%, but, for the sake of simplicity, only red and green phases were considered. To introduce variability, the initial phase was randomly assigned. The speed boundaries were modified allowing a time-dependent upper boundary where the traffic lights are located. The upper boundary assumes the moving average value or zero if the traffic light has a green or red phase, respectively. As depicted in Figure 5.22b, it is assumed that SPaT information is deterministic and given; thus, the optimizer can have a-priori access to infrastructure and traffic information via V2I communication.

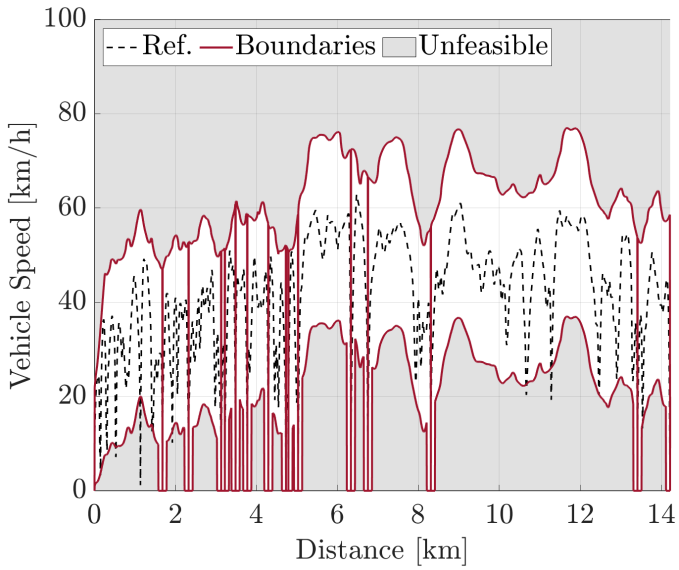

Fig. 5.23 Speed boundaries: the upper and lower boundaries of the window were thought to merge the effects of speed limits and mild traffic conditions in a realistic scenario.

5.2.2 Optimal Control Problem

The eco-driving problem can be formalized as an optimal control problem (see Section 3.2), where the optimizer can have access to both the vehicle's GPS coordinates (e.g., total trip length, road grade, and speed limits) and V2X information (e.g., SPaT, traffic conditions). Since the position of all the route features varies in a time-based perspective but remains fixed in a distance-based one, it is beneficial to express the model equations in distance-based coordinates: distance l (instead of time t) becomes the independent variable. Equation 3.2 can be reformulated as follows:

$$J = \Phi(x(l_f), l_f) + \int_{l_0}^{l_f} L(x(l), u(l), l)\, dl \tag{5.1}$$

subject to the following constraints:

$$\begin{cases} G(x(l), l) \leq 0 \\ x(l) \in X(l) \qquad \forall \quad l \in [l_0, l_f] \\ u(l) \in U(l) \end{cases} \tag{5.2}$$

Table 5.5 State and control variables for Scenario #1 and Scenario #2.

	Scenario #1	**Scenario #2**
State Variables	Speed	Speed,Time
Control Variables	Acceleration	Acceleration

The optimization framework includes information coming from the surrounding environment, e.g., traffic lights state, speed limits, distance to travel, etc. Starting from the optimal control problem defined in distance-based coordinates (Equation 5.1), the cost function of this problem was defined according to the following:

$$J = \int_{l_0}^{l_f} \beta \frac{e_{fd}(x(l),u(l),l)}{E_{fd}} + (1-\beta)\frac{t(x(l),u(l),l)}{T}\, dl \tag{5.3}$$

where β is a calibration factor that weighs the influence of the energy demand at the expense of the traveling time; e_{fd} and t denote, respectively, the energy and time demand at the single distance step; E_{fd} and T denote, respectively, the energy and time demand along the entire cycle. The constraints for the specific problem are the physical limitations of the actuators (maximum deliverable power), limits from road infrastructure, e.g., speed limits and traffic lights stop, and maximum acceleration and deceleration values (imposed to enhance the driver's comfort in the vehicle). Table 5.5 shows the chosen state and control variables. In Scenario #1, the vehicle speed is the only state variable and vehicle acceleration is the only control one. In Scenario #2, since the SPaT is time-dependent, the time must be added as a state variable increasing the computational burden. For speed, acceleration, and time variables a discretization resolution of $1km/h$, $0.01m/s^2$, and $0.5s$ were used, respectively, while a discretization resolution of $5m$ was used for the independent variable, i.e., distance.

5.2.3 Variable Grid Dynamic Programming

In this work, Dynamic Programming (DP) [90] is used to solve the associated energy minimization problem. In particular, the open-source MATLAB® code developed at ETH-Zurich [140] was used for solving the optimal control problem. In n-dimensional state and m-dimensional control spaces, the number of discrete grid points rises exponentially with the dimensions of n and m [155]. These large

computing power requirements have made the DP usage for the eco-driving problem largely limited to asserting an offline performance benchmark. However, with the recent advances in ITS technology that could allow vehicles to share information with the surrounding environment, it seems feasible that the vehicles can have realistic information about speed limits and ETA. In this context, the VGDP can use the average traffic information and the ETA to reduce the space of the states to only those feasible: this allows for drastically reducing the computation burden of this algorithm. Figure 5.24 shows the definition of the variable grid in the urban section of Scenario #1. Specifically, the variable speed grid was defined according to the upper and lower boundaries (supposing that the vehicle can never exceed those limits), while the variable time grid was defined allowing the optimizer to sufficiently vary around a predicted time of arrival. The introduction of the variable state search grid is particularly relevant for Scenario #2 (two control variables). As shown in Figure 5.25, it allows a reduction in the computational time of more than 95% if compared to the standard optimization performed with a fixed grid. It should be noted that an increase of the interval chosen for the distance discretization, despite degrading the accuracy of the solution, can be beneficial for the computational time: a preliminary investigation showed that a 10x increase in the distance step can lead to an 11x reduction in the computational time. The computational times here shown refer to a workstation with the following specifications: Intel(R) Xeon(R) CPU E5-2680 v3 @ 2.50GHz, 64 GB RAM.

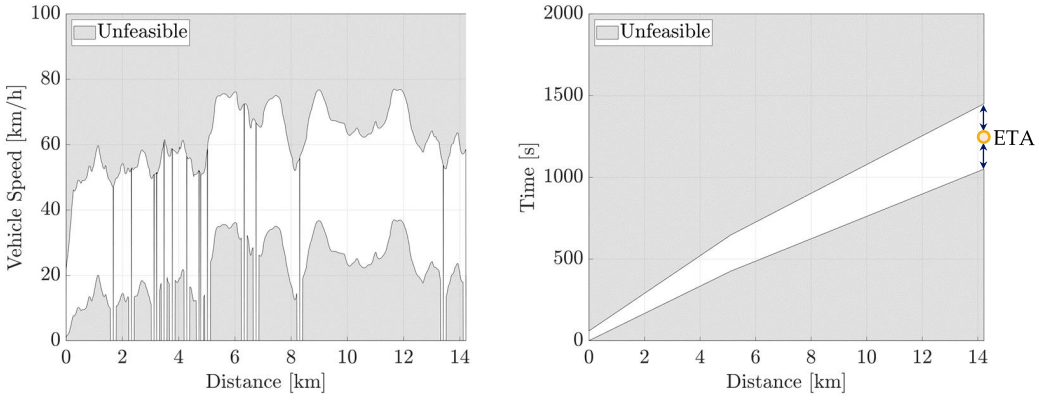

Fig. 5.24 Variable state search grid: the variable speed grid was defined according to the upper and lower boundaries, supposing that the vehicle can never exceed those limits. The variable time grid was defined allowing the optimizer to sufficiently vary around an Estimated Time of Arrival (ETA).

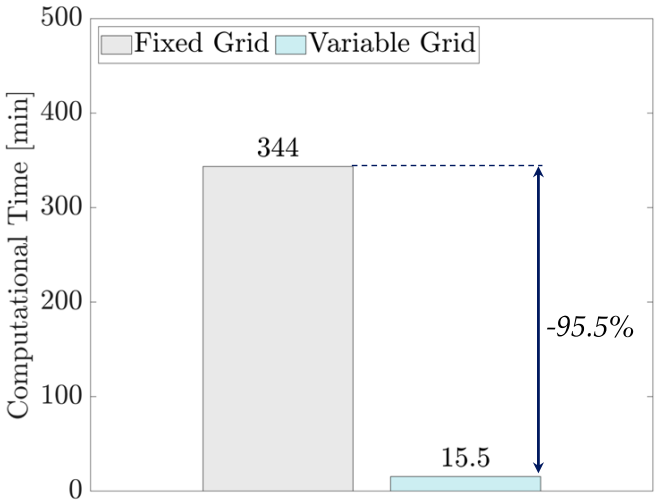

Fig. 5.25 Scenario #2: computational time for the optimal control problem with a fixed state search grid (grey) and a variable state search grid (light blue). The variable grid allows a reduction in the computational time of more than 95%.

5.2.4 Scenario #1 Optimization

In this Section, the vehicle speed optimization for Scenario #1 is analyzed. Figure 5.26 shows the optimized vehicle speed for Scenario #1 (blue line) compared to the Reference Scenario (black dotted line). The optimizer chooses an almost constant speed only in the rural section, while, in the urban and highway sections, the vehicle speed lies as much as possible on the lower and upper boundaries, respectively. From Figure 5.27, where a detail of the urban section is shown, it can be seen that the optimal speed presents smoother accelerations and decelerations if compared to the Reference Scenario, still respecting all the full stops imposed by the infrastructure.

Figure 5.28 shows the achievable reductions in terms of travel time and energy for Scenario #1. Nearly 30% of energy reduction can be obtained while decreasing the travel time by almost 10%. It should be mentioned that, for simplicity, regenerative braking is not considered in this analysis: all the energy required for braking is considered lost.

5.2.5 Scenario #2 Optimization

In this Section, the vehicle speed optimization for Scenario #2 is analyzed. Since the major benefits of a smart infrastructure can be obtained in an urban environment,

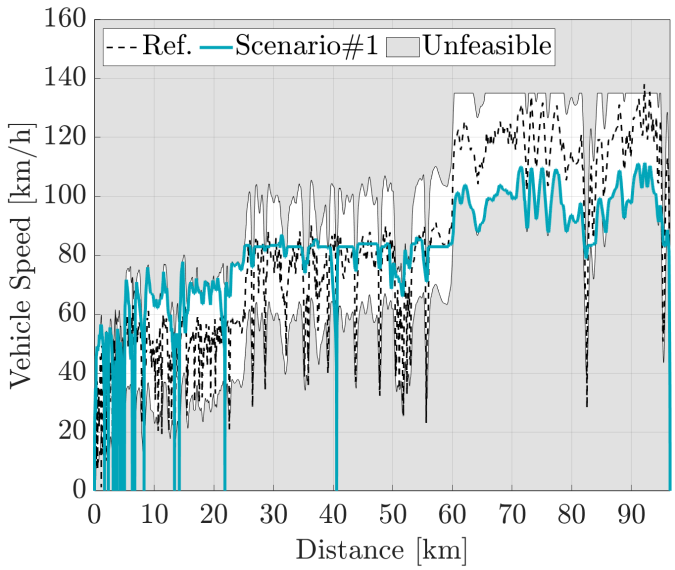

Fig. 5.26 Scenario #1: optimized vehicle speed (light blue) compared to the Reference Scenario (dashed black) on the RDE-compliant route.

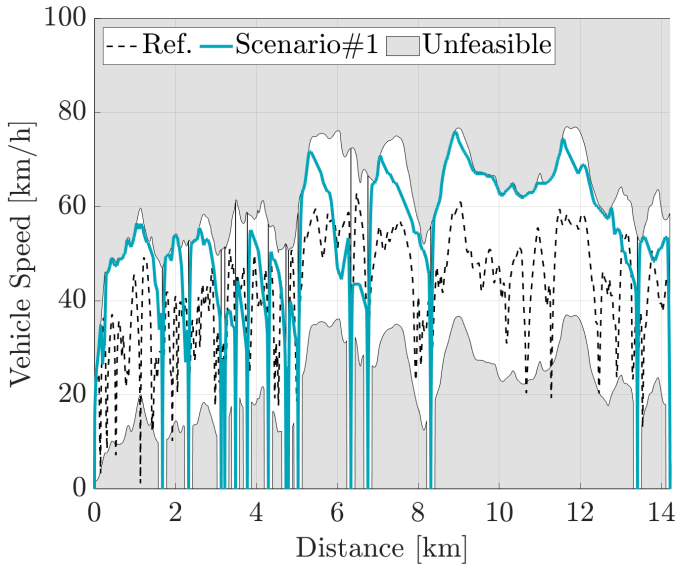

Fig. 5.27 Scenario #1: optimized vehicle speed (light blue) compared to the Reference Scenario (dashed black) on the urban section of the RDE-compliant route.

only this section will be analyzed. Figure 5.29 shows the optimized vehicle position as a function of time along with all the traffic light phases. Since the SPaT of the traffic lights is communicated to the optimizer, the chosen speed trajectory allows crossing all the intersections at a green light. As evident from Figure 5.30, an almost

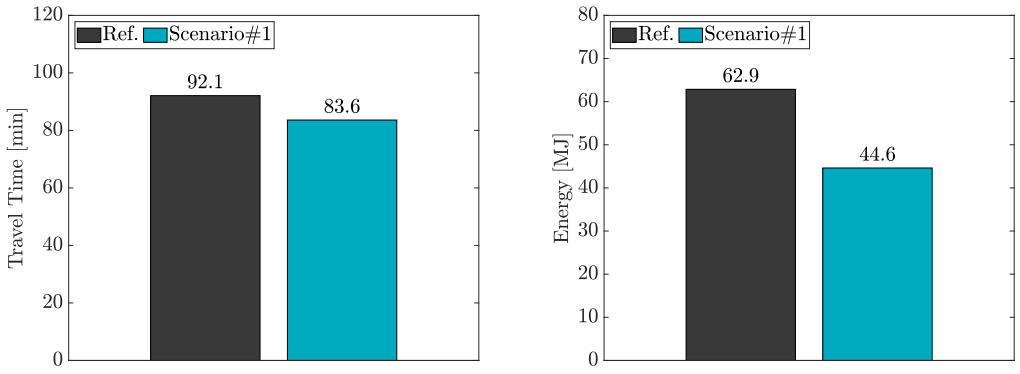

(a) (b)

Fig. 5.28 Scenario #1: (a) - Achievable time reduction on the RDE-compliant route; (b) - Achievable energy reduction on the RDE-compliant route.

constant speed is preferred: the results suggest that a stop sign (or in general a full stop of the vehicle) is detrimental to both the travel time and the required energy. The deceleration and acceleration phases preceding and following a full stop of the vehicle cause a major reason for energy loss that should be avoided.

Figure 5.31 quantifies the maximum achievable reductions in terms of energy and travel time in a framework of connected vehicles able to exploit V2X information in a smart infrastructure. The introduction of smart infrastructure can lead to a further reduction both in terms of travel time and energy if compared to Scenario #1. In an urban environment, the energy required by the vehicle can be halved while decreasing the travel time by more than 35%.

5.2.6 Sensitivity Analysis

An additional sensitivity analysis was performed to assess the impact that the weighting factor can have on the results. Three different cases were considered: Case 1 ($\beta = 0.2$) prioritizes travel time at the expense of energy; Case 2 ($\beta = 0.5$) gives equal weight to travel time and energy (results shown in Sections 5.2.4, 5.2.5); Case 3 ($\beta = 0.8$) prioritizes energy at the expense of travel time. Figure 5.32 shows the Pareto front, between energy and travel time, that is obtained by varying the value of β in Scenarios #1 and #2, while Table 5.6 and Table 5.7 provide more granularity by displaying the numerical comparison of the effect of using different values of β.

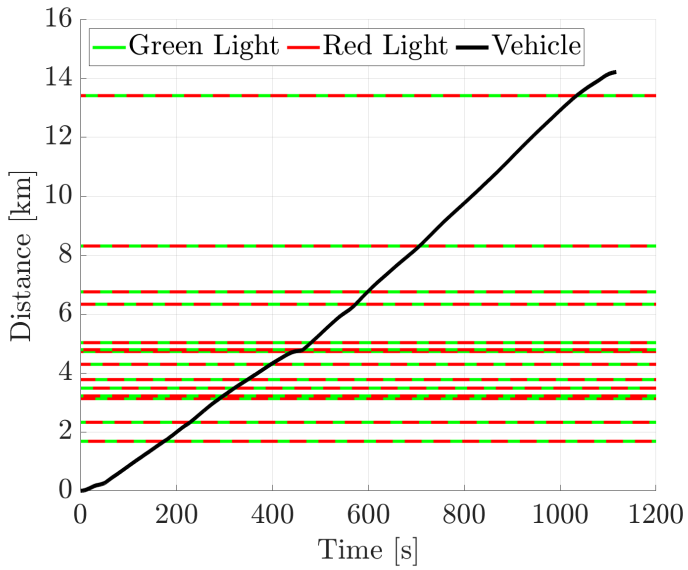

Fig. 5.29 Scenario #2: vehicle position as a function of time along with all the traffic light phases. The optimizer chooses the best speed trajectory in order to cross all the intersections at a green light.

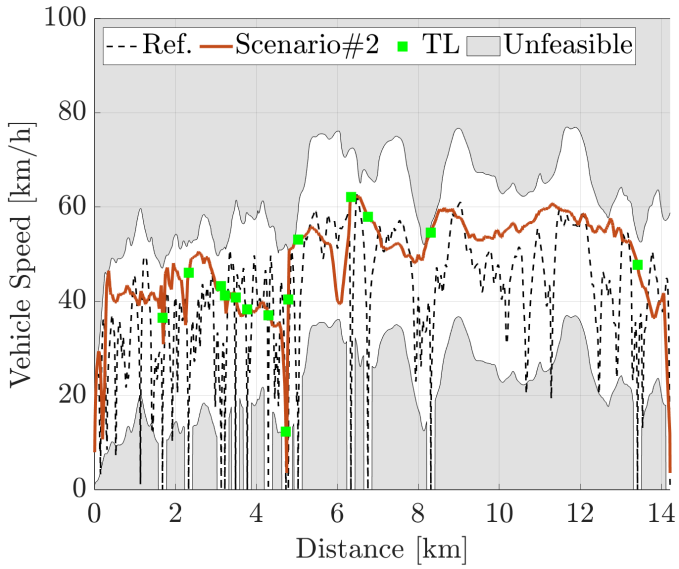

Fig. 5.30 Scenario #2: optimized vehicle speed (orange) compared to the Reference Scenario (dashed black) on the urban section of the RDE-compliant route.

Focusing on Scenario #1 (light blue marks), the energy consumed to perform the cycle is reduced in all three cases if compared to the Reference Scenario. For Case 3 (light blue diamond), however, the excessively conservative driving style

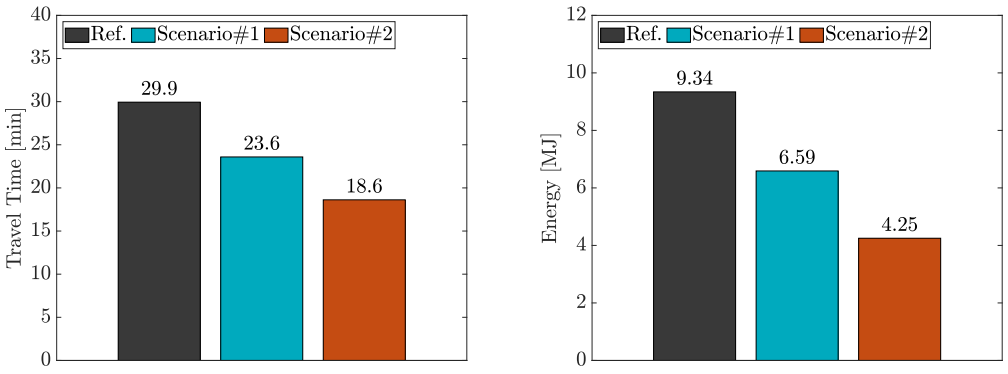

(a) (b)

Fig. 5.31 (a) - Achievable time reduction on the RDE-compliant route for Scenario #1 (light blue) and #2 (orange); (b) - Achievable energy reduction on the RDE-compliant route for Scenario #1 (light blue) and #2 (orange).

Table 5.6 Scenario #1: numerical comparison of the effect of different β values on the energy consumption and travel time.

		Ref.	Case 1	Case 2	Case 3
Energy	[MJ]	9.3	8.3 -11%	6.6 -29%	4.7 -50%
Travel Time	[min]	30	22 -26%	24 -24%	29 -1%

Table 5.7 Scenario #2: numerical comparison of the effect of different β values on the energy consumption and travel time.

		Ref.	Case 1	Case 2	Case 3
Energy	[MJ]	9.3	4.4 -53%	4.3 -54%	3.9 -59%
Travel Time	[min]	30	18 -38%	19 -38%	21 -28%

leads to an increase in travel time if compared to the Reference Scenario. Focusing on Scenario #2 (orange marks), Figure 5.32 proves that the introduction of a smart infrastructure, i.e., connected traffic lights, can further improve the trade-off between required energy and total travel time. Moreover, Figure 5.32 shows that the variation

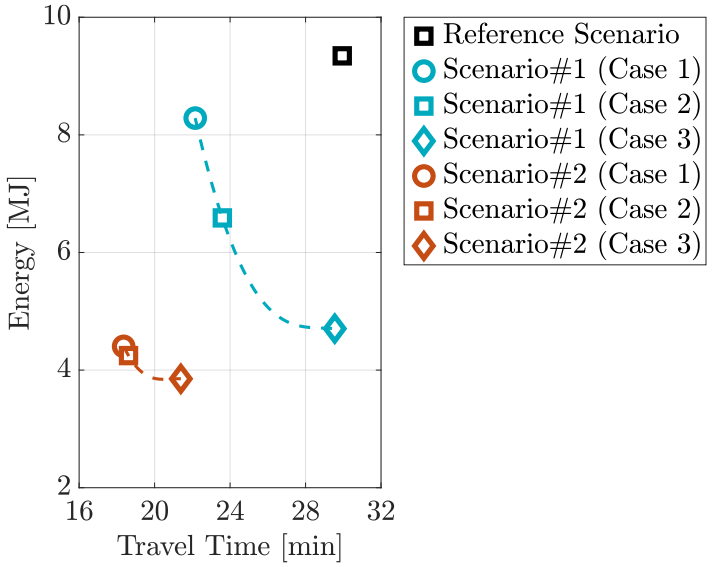

Fig. 5.32 Pareto front between energy and travel time for both Scenario #1 (light blue) and Scenario #2 (orange) when varying the value of the weighting factor β.

of the weighting factor in Scenario #2 leads to a much more restrained variation in the trade-off energy/time.

5.3 A-ECMS based on V2X

In the last decade, the availability of cloud computing platforms and the introduction of look-ahead technologies, such as V2X connectivity, have paved the way for reliable predictions of future driving conditions. In this Section, the virtual test rig obtained in Section 5.1 will be used to assess the potentialities of an advanced energy management strategy that exploits these technologies. An innovative Adaptive V2X connectivity-based ECMS (A-V2X-ECMS) uses a limited set of future operating conditions to obtain, from LSTM networks, the optimal equivalence factor. The novelty of this work is the algorithm proposed for the equivalence factor selection: differently from other studies, it only uses vehicle speed prediction and does not need any calibration, except the preliminary training of the ML models that must be performed off-line. In this work, V2X connectivity is assumed to provide a reliable speed prediction, and, since it represents a preliminary assessment of the algorithm potentiality, a perfect knowledge of the future speed profile is assumed (e.g., the

uncertainties related to the estimation of traffic conditions are neglected). This work is described more in detail in [146].

5.3.1 Database Expansion

Since the experimental tests performed on the real vehicle had been limited due to time and money constraints (see Section 5.1.2), the only available experimental data would not have been sufficient to fully exploit the potentialities of ML algorithms. To cover a wider spectrum of driving patterns, a database expansion was performed: the virtual test rig, obtained through the model validation, was used as a test bench where the vehicle could virtually perform several mission profiles. The database consisted of traces available from experimental tests carried out on other vehicles and type-approval procedures available from the literature (i.e., EPA tests [156], - such as US06, FTP, etc. - Artemis cycles [157] and RTS95 [158]). Moreover, concerning the gearshift logic, the experimental tests were used for training NNs in mimicking the experimental behavior and later used to reproduce the gearshift logic of the actual vehicle on the tests performed with the digital twin. The database expansion led to an increase in the time of vehicle testing from 510 min (experimental) to 1927 min (experimental + virtual). Figure 5.33 displays all the cycles as a function of two main energetic indices: the square of the average vehicle velocity and the product of average vehicle velocity and average vehicle acceleration. They can be considered indicators of the average energy required in a cycle, and the driving cycle aggressiveness, respectively. It should be noted that the area covered in the plot is considerably widened thanks to the database expansion and that the cycles selected for testing the proposed strategy (green dots) are well distributed over the plot.

5.3.2 Strategies Comparison

The performance of the proposed strategy is assessed by comparing it with the following strategies:

- Rule-Based:
  Rules extracted from the actual vehicle (see Section 5.1.3. The strategy comprises simple rules, thus it is easily implementable in a vehicle ECU;
- Optimal ECMS:
  ECMS (see Section 3.3.3) where the equivalence factor is properly calibrated

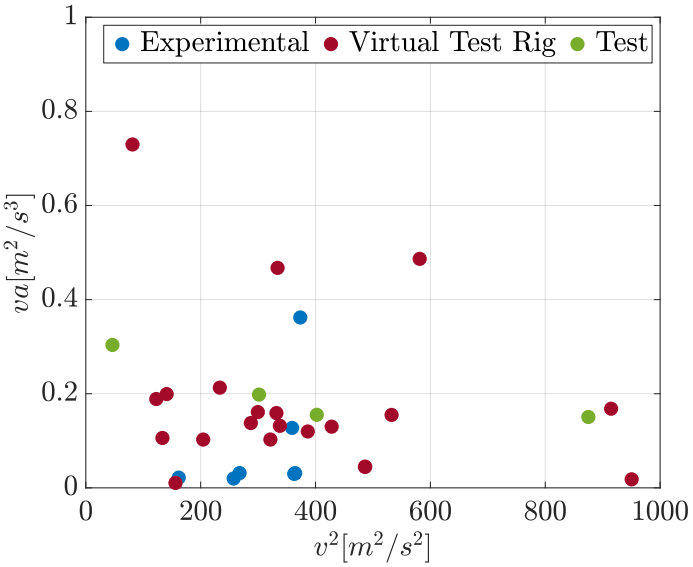

Fig. 5.33 Database expansion: cycles plotted as a function of squared vehicle velocity and velocity times acceleration.

through an offline optimizer. Since this strategy requires the a-priori knowledge of the entire vehicle mission profile. it will only be used as a reference for optimal results;

- Standard A-ECMS:
  ECMS where the equivalence factor is periodically updated based on its past values and the difference between actual and reference SoC (see Equation 3.20. In this work, $k_p = 1$, and coherently with [113], $T = 120s$;
- A-V2X-ECMS:
  The strategy proposed in this work uses vehicle speed prediction to guess the optimal equivalence factor.

5.3.3 Proposed A-V2X-ECMS

The overall structure of the proposed methodology is shown in Figure 5.34. The initial value of the equivalence factor is provided by an LSTM network, that using information about future vehicle driving patterns and the current SoC level, chooses the appropriate value of the equivalence factor. Then, the value of the equivalence factor is kept constant until some trigger events occur, i.e., a radical change of driving pattern (e.g., a vehicle moving from an urban to a rural condition) or a high deviation

of the SoC from the reference value. As far as the change in the driving patterns is concerned, a methodology was developed for defining one or more energetic indices that can capture it. When a trigger event occurs, the LSTM network is used to update the value of the equivalence factor depending on the new conditions. By comparing this methodology to the standard law proposed in [113], we can introduce proactive behavior thanks to the information coming from V2X connectivity.

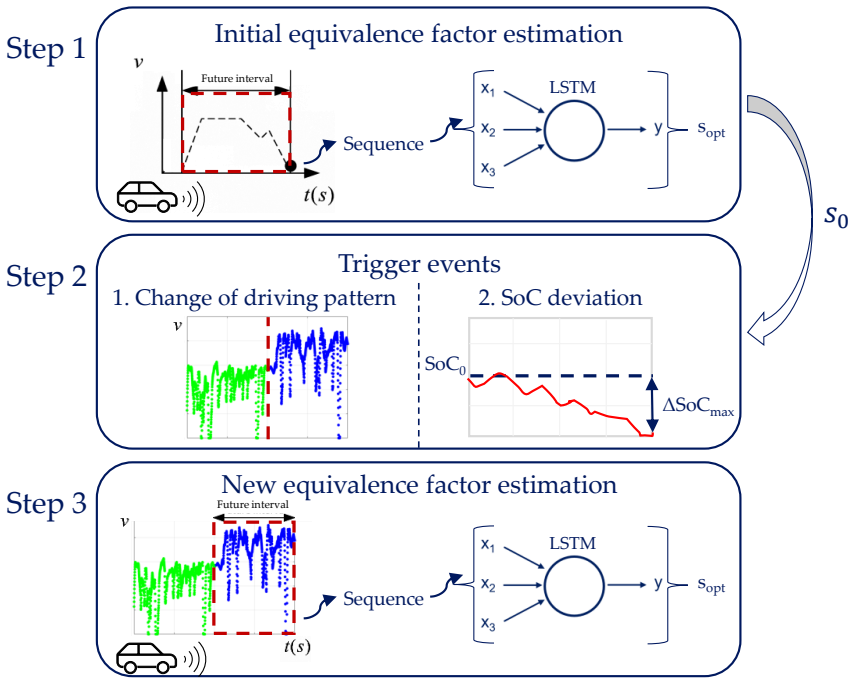

Fig. 5.34 The overall structure of the proposed A-V2X-ECMS methodology.

Driving Pattern Recognition

For a given vehicle configuration, the characteristics of a certain driving scenario can be directly related to the energy required by the powertrain, which strongly affects its efficiency. Therefore, since the equivalence factor represents the efficiency of the powertrain energy flows, it is possible to find a mathematical correlation between its optimal value and the driving conditions. Thus, it could theoretically be possible to identify one or more energetic indices that can fully characterize a certain driving scenario. In the proposed methodology, an unsupervised learning technique is adopted to cluster the driving conditions in three different groups. The number of clusters was chosen coherently with the typical classification used by the European Regulation in the RDE cycles (namely, urban, rural, and highway) [149].

Table 5.8 Energetic indices used for collecting information about the driving patterns of the driving cycles.

	Energetic Index	Symbol	Unit		Energetic Index	Symbol	Unit
1.	$\frac{\sum_{i=1}^{N} v_i}{N}$	$\overline{v}$	$[\frac{m}{s}]$	**8.**	$\frac{\int_{t_i}^{t_f} v^2(t)dt}{\int_{t_i}^{t_f} v(t)dt}$	v^2	$[\frac{m}{s}]$
2.	$\sqrt{\frac{1}{N}\sum_{i=1}^{N}(v_i-\overline{v})^2}$	σ_v	$[\frac{m}{s}]$	**9.**	$\frac{\int_{t_i}^{t_f} a^2(t)dt}{\int_{t_i}^{t_f} v(t)dt}$	a^2	$[\frac{m}{s^3}]$
3.	$\frac{\sum_{i=1}^{N} a_i}{N}$	$\overline{a}$	$[\frac{m}{s^2}]$	**10.**	$\frac{\int_{t_i}^{t_f} v(t)a(t)dt}{\int_{t_i}^{t_f} v(t)dt}$	va	$[\frac{m}{s^2}]$
4.	$\sqrt{\frac{1}{N}\sum_{i=1}^{N}(a_i-\overline{a})^2}$	σ_a	$[\frac{m}{s}]$	**11.**	FFT_1	P_1	$[Hz]$
5.	$\frac{\int_{t_i}^{t_f} v^2(t)dt}{t_f-t_i}$	I_v^2	$[\frac{m^2}{s^2}]$	**12.**	FFT_2	P_2	$[Hz]$
6.	$\frac{\int_{t_i}^{t_f} a^2(t)dt}{t_f-t_i}$	I_a^2	$[\frac{m^2}{s^4}]$	**13.**	FFT_3	P_3	$[Hz]$
7.	$\frac{\int_{t_i}^{t_f} v(t)a(t)dt}{t_f-t_i}$	I_{va}	$[\frac{m^2}{s^3}]$	**14.**	FFT_4	P_4	$[Hz]$

Each driving cycle comprising the database described in Section 5.3.1 was subdivided into sub-cycles, lasting 120s each: this time interval represents a tradeoff between the lengths of a reliable speed prediction and a reliable characterization of the driving pattern. The indices, chosen for collecting information about the driving pattern of each sub-cycle, are listed in Table 5.8. They are obtained from simple statistical formulas applied to the vehicle speed and acceleration, while the FFT_i denote the first four harmonics obtained by applying the Fast Fourier Transform (FFT) algorithm to the velocity signal. In Table 5.8, $v(t)$ is the vehicle speed, $a(t)$ is the vehicle acceleration, t_f is the final time, t_i is the initial time, and N is the number of sampling points.

The k-means algorithm [159] was chosen for this application. This technique partitions data into k number of mutually exclusive clusters: a point is assigned to a specific cluster if, in the hyperplane described by the features (the energetic indices in our case), the distance between the point and the center of the cluster is minimized; then, each center is recomputed as the center of mass of all points assigned to it. These two passages (assignment and center calculation) are repeated until the process reaches convergence. By way of example, Figure 5.35 show the driving pattern recognition performed on the RDE_7. As previously explained, the cycle is first subdivided into intervals 120s long, then the energetic indices listed in

Table 5.8 are computed and used as input to the k-means algorithm. As evident from Figure 5.35, this procedure allows for correctly recognizing the different driving patterns. The first portion of the driving cycle, which is conducted in an urban environment, is identified as the first cluster (that we call urban). The second portion of the driving cycle, which occurred in extra-urban driving conditions, is subdivided into two other clusters (that we call rural and highway, respectively). These results, along with the ones coming from other mission profiles, proved that the k-means algorithm, using the defined energetic indices, can correctly recognize the different driving patterns.

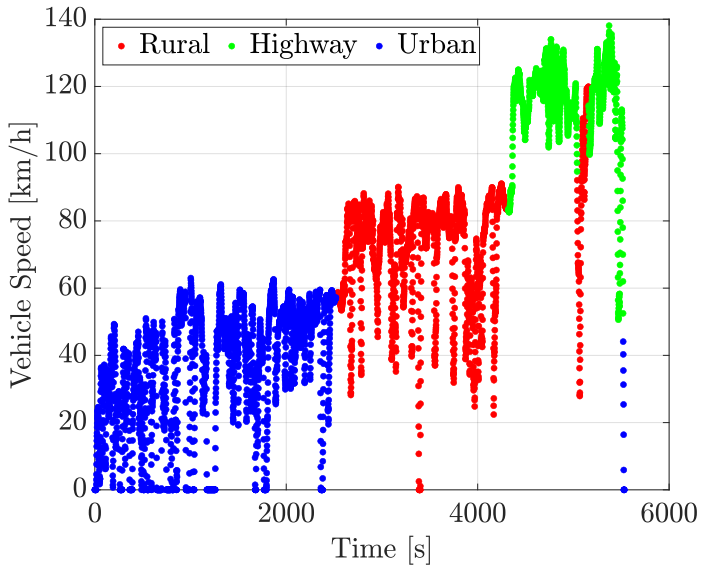

Fig. 5.35 Driving pattern recognition performed on the RDE_7 with a k-means algorithm.

Dimensionality Reduction

In order to investigate the influence of the energetic indices on driving pattern recognition, a Principal Component Analysis (PCA) [160] was performed. This technique represents the variables (in our case the energetic indices) as a set of new orthogonal variables, called "principal components". Its goal is to extract the important information from the variables and capture most of the variance with the first few principal components. Figure 5.36a depicts the Pareto chart, where each bar represents the weight of a principal component, while Figure 5.36b depicts the relative weights of the indices (the rows) for each component (the columns): the darker the blue, the bigger the weight. It may be seen that the first principal

component alone can describe all the variability among the dataset and that this component is mainly composed of the energetic index I_v^2 (#5 in Table 5). The results coming from the PCA seem to suggest that, given a vehicle speed profile, a k-means algorithm using only the I_v^2 index can correctly recognize the correct driving pattern.

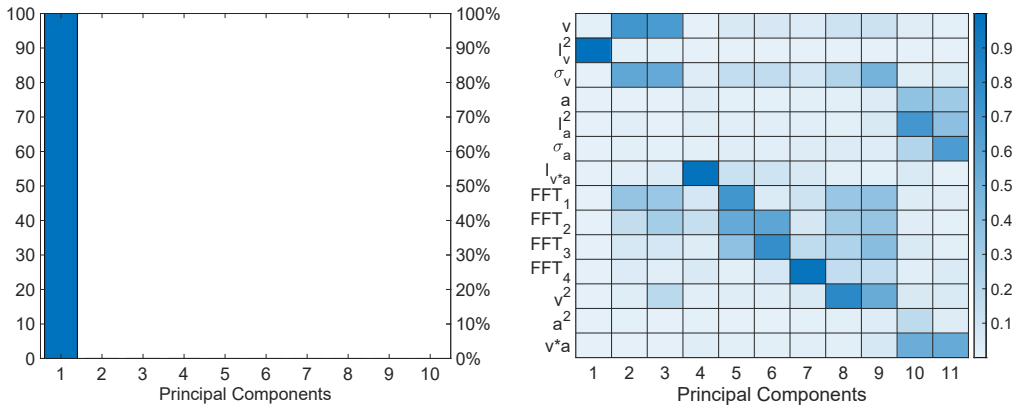

(a) (b)

Fig. 5.36 PCA performed on the energetic indices. (a): Pareto chart of the principal components; (b): Heat map of the principal components - the colors represent the relative weights of the indices (the rows) for each component (the columns).

Online Driving Pattern Recognition

The procedure previously described can only provide a posteriori cluster identification of the driving patterns, but a different approach is necessary to obtain a real-time adjustment of the equivalence factor. Therefore, some threshold levels were identified for the I_v^2 index, by computing, over the entire dataset, the average values that the k-means algorithm associates to a change of driving pattern (i.e., urban, rural, and highway). By way of example, Figure 5.37a shows the I_v^2 index profile along with the obtained threshold levels on the RDE_7. Coherently with the subdivision performed in Section 5.3.3, the I_v^2 index at a specific time t is computed on the interval $[t \div t + 120s]$. The threshold levels regulate the transitions between the driving patterns: $1 \rightarrow 2$ from urban to rural and vice versa $2 \rightarrow 1$; $2 \rightarrow 3$ from rural to highway and vice versa $3 \rightarrow 2$, and Figure 5.37b depicts the vehicle speed profile by highlighting the driving patterns with different colors. The striking similarities between Figures 5.35 and 5.37b prove that the I_v^2 index thresholds can achieve an online cluster identification consistent with the one obtained a posteriori with the k-means algorithm.

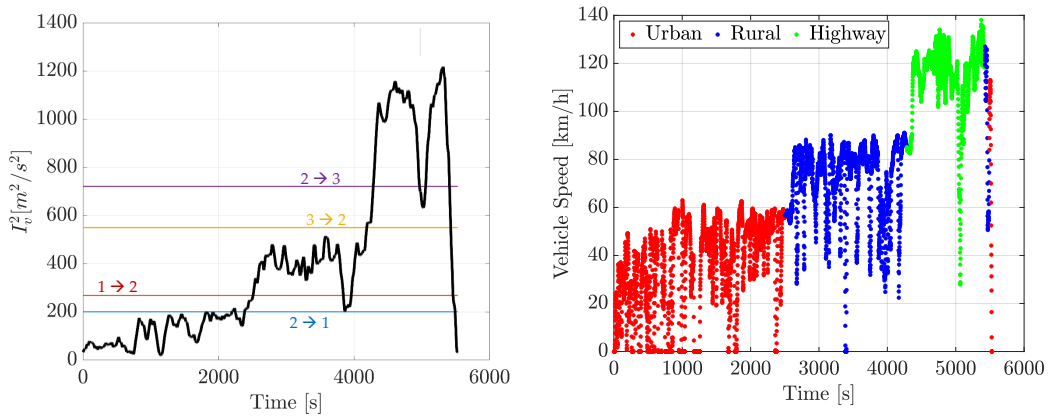

(a) (b)

Fig. 5.37 (a): I_v^2 index computed on the RDE_7 along with the defined thresholds. (b): Speed profile of the RDE_7 plotted as a function of time: the passage from one pattern to another is highlighted by a change in color.

LSTM Deep Neural Networks Training

The LSTM networks were trained with the same database used for the driving pattern identification. For this analysis, the driving cycles were subdivided into sub-cycles of various lengths reasonably assigned to urban, rural, and highway clusters. For each sub-cycle, 7 different levels of initial SoC were considered between 0.1 and 0.25. The SoC levels were added to consider, also in the training phase, different initial discrepancies between actual and target SoC values. Considering all the sub-cycles and the corresponding SoC levels, the database consisted of 1169 observations. Each sub-cycle was considered as a set of sequences, i.e., vehicle speed, vehicle acceleration, required power, and initial SoC.

On the other hand, the virtual test rig validated in Section 5.1.4 was used for computing the optimal equivalence factor. A genetic algorithm optimization was implemented aimed at minimizing the difference between actual and target final SoC values. In the optimization, the optimal equivalence factor could vary between 1.5 and 3.0, but all the cases featuring a boundary value, i.e., 1.5 or 3.0 were discarded, since a boundary value means that the final SoC target could not be reached due to the excessive difference from the imposed initial value. This selection led to a reduction in the number of observations from 1169 to 944. As shown in Figure 5.38, the LSTM network was trained by assigning the predicted output patterns (the optimal equivalence factors) to the training set (the observations). The experiment manager app [161] was used in the design of the network hyperparameters, i.e., all

the fixed parameters chosen by the user and not tuned during the training phase. After defining the allowed range of variation, this tool can optimize the hyperparameters under multiple initial conditions. For this analysis, a Bayesian optimization was used and the obtained hyperparameters are shown in Table 5.9.

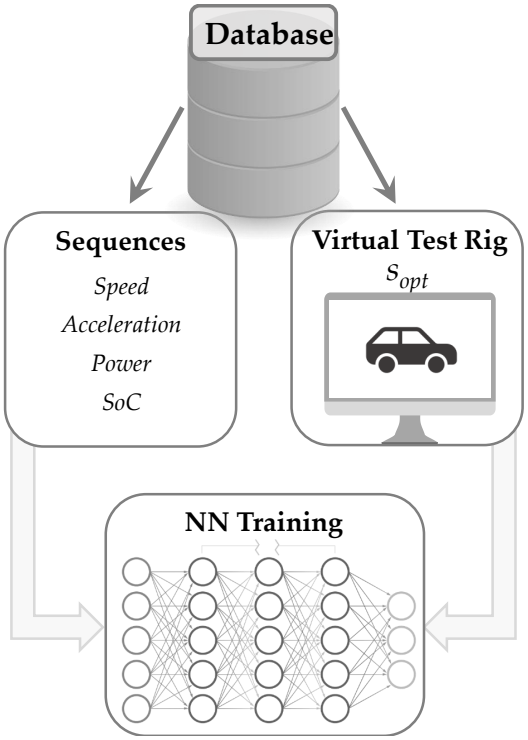

Fig. 5.38 Training of the LSTM network: the predicted output patterns (the optimal equivalence factors) are assigned to the training set (the observations).

The topology of the LSTM network is shown in Figure 5.39: the input layer features 4 nodes and receives, as inputs, vehicle speed, vehicle acceleration, required power, and initial SoC. Then, two fully connected layers, with 40 and 28 nodes, respectively, are followed by the dropout and the regression output layers.

Computational Time

It is worth noting that the proposed methodology does not require an increase in computational time if compared to a standard ECMS formulation. In fact, the NNs require an additional computational effort only when a trigger event occurs and the equivalence factor value must be updated. Table 5.10 displays the computational time required for performing the simulations along with the Real-Time (RT) factor, i.e., the ratio between simulation and real cycle duration. The computational time is shown for all the Artemis driving cycles: Artemis Urban, Road, and Motorway

Table 5.9 Hyperparameters of the LSTM network used in the A-V2X-ECMS model.

Hyperparameters	Value
Deep	2
nNodes1	40
nNodes2	28
Dropout	0.5418
Learn Rate	0.001
Regularization Factor	1.0620e-9

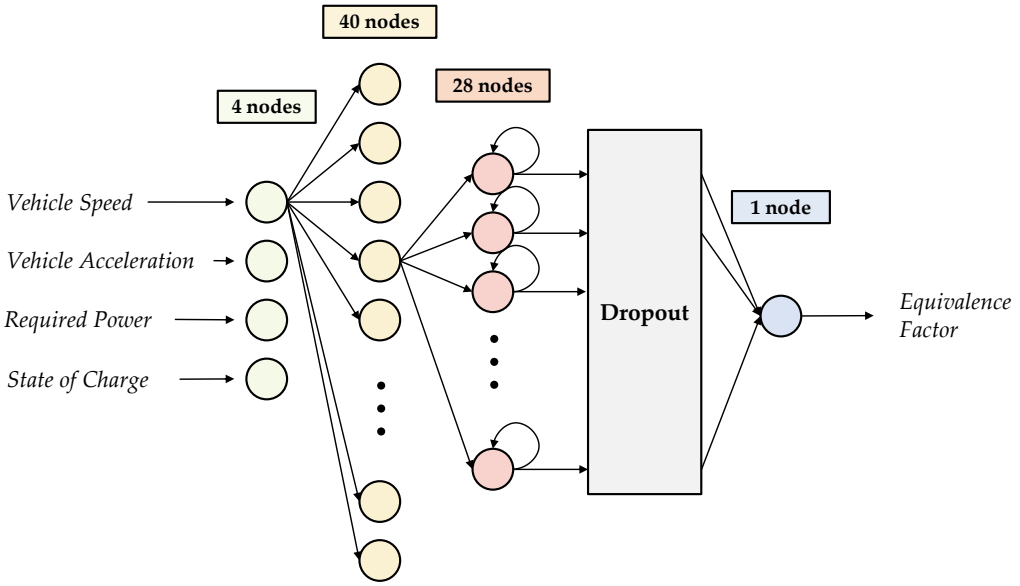

Fig. 5.39 Topology of the LSTM network: input layer, 2 fully connected layers, dropout layer, and regression output layer.

last 993s, 1082s, and 1028s, respectively. It is evident that, in all the simulations, the RT factors of the proposed A-V2X-ECMS are almost identical to the ECMS ones, making this strategy feasible in a vehicle ECU. On the contrary, A-V2X-ECMS-C displays the case in which the NNs are used for continuously updating the equivalence factor; in this case, the computational time drastically increases, leading to a non-feasible strategy. The computational times here shown refer to a PC with the following specifications: Intel (R) Core (TM) i7-2600 CPU @ 3.40GHz, 3.40 GHz, 16 GB RAM.

Table 5.10 Comparison of the computational time for different simulations featuring a standard ECMS, the proposed A-V2X-ECMS, and an A-ECMS where NNs are used to continuously update the equivalence factor.

	ECMS		**A-V2X-ECMS**		**A-V2X-ECMS-C**	
	Duration	**RT Factor**	**Duration**	**RT Factor**	**Duration**	**RT Factor**
Artemis Urban	6min 57s	0.42	7min 11s	0.43	7h 59min 19s	29.0
Artemis Road	8min 10s	0.45	8min 1s	0.44	8h 40min 4s	28.8
Artemis Motorway	7min 25s	0.42	7min 52s	0.44	8h 32min 17s	28.8

5.3.4 Results

The fuel economy potential of the A-V2X-ECMS was assessed on the Artemis driving cycles [157] and over the RDE_7 cycle to prove its capabilities in a driving scenario that follows all the requirements of the RDE Regulation [149]. It is worth mentioning that the cycles used for testing the LSTM network were never used during the training phase. For the sake of brevity, this dissertation will present only the results over the RDE_7 cycle, comparing them with the ones coming from the RB logic, the Standard A-ECMS, and the ECMS featuring the optimal equivalence factor. Regarding the RB strategy, it should be noted that, while the model validation was performed in CD+CS operation (see Section 5.1.4), only the CS strategy will be considered for this analysis. Figure 5.40a depicts the SoC profile for the RB strategy (dashed black), Standard A-ECMS (light blue), optimal ECMS (yellow), and A-V2X-ECMS (red), while Figure 5.40b shows the corresponding equivalence factor profile. Figure 5.41, instead, displays the trade-off between CO_2 emissions and final SoC values for all four cases.

As evident from Figure 5.40a, the RB strategy does not achieve charge sustainability: since the ICE is excessively used to charge the battery during the cycle, this strategy does not exploit the full potential of the hybrid powertrain, leading to higher CO_2 emissions. In the Standard A-ECMS, although the charge sustainability is satisfyingly respected, the continuous adaptation of the equivalence factor introduces oscillations that lead to SoC swings. On the contrary, the A-V2X ECMS reaches a final SoC value not so far from the optimal ECMS, and the Standard A-ECMS ones, but, updating the equivalence factor only when a trigger event occurs, the oscillations of the equivalence factor are strongly decreased. Its value is confined in an interval

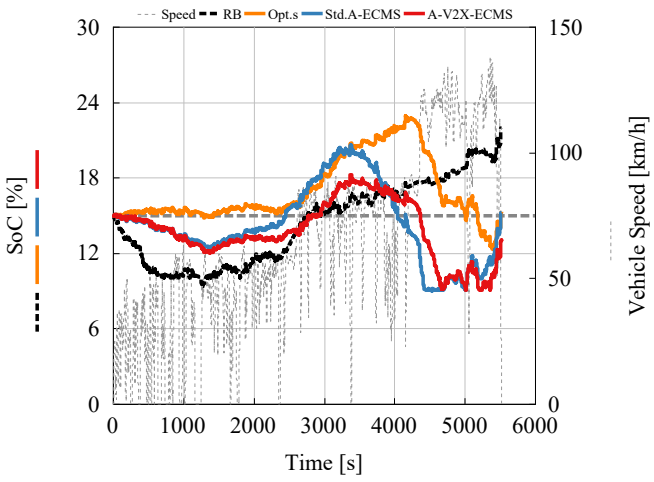

(a)

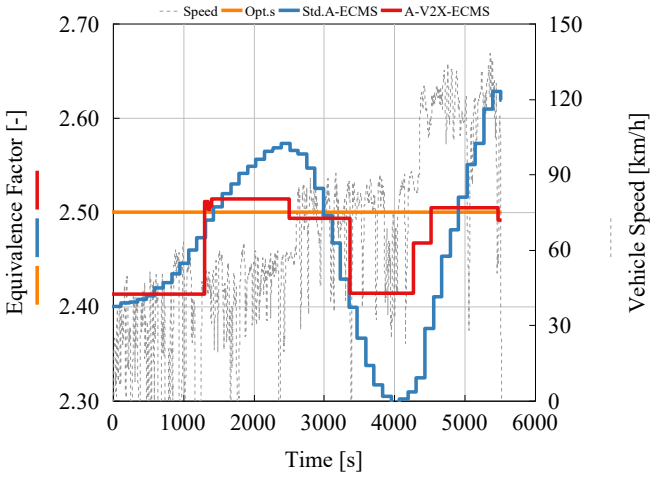

(b)

Fig. 5.40 Comparison of the results over the RDE_7 cycle for RB, ECMS optimized for CS conditions, Standard A-ECMS, and A-V2X-ECMS – (a): SoC as a function of time – (b): Equivalence factor as a function of time.

much closer to the optimal equivalence factor if compared to the Standard A-ECMS. In terms of charge sustainability, the two methodologies are quite comparable (see 5.40a), but for the A-V2X-ECMS the SoC is confined in a smaller interval around the target value over the entire mission profile, thus leading to a better trade-off between CO_2 emissions and final SoC. In fact, the A-V2X-ECMS chooses the most appropriate equivalence factor for each section, and eventually reaches better performance in terms of fuel economy over the entire cycle.

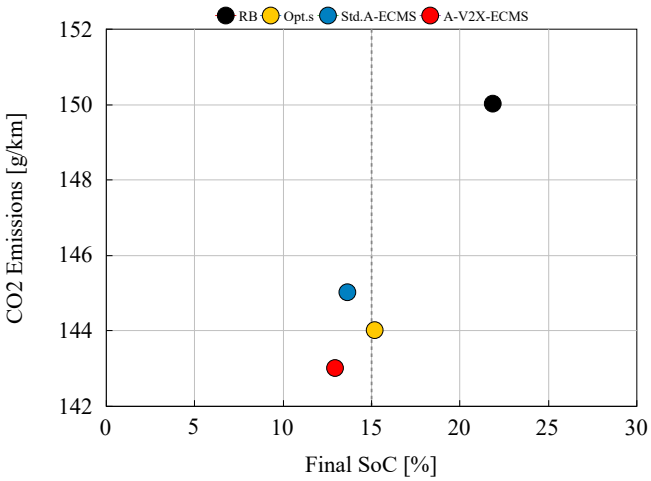

Fig. 5.41 Comparison of the results over the RDE_7 cycle for RB, ECMS optimized for CS conditions, Standard A-ECMS, and A-V2X-ECMS: Tradeoff between CO_2 emissions and final SoC.

The differences between the four strategies in optimizing the engine operation can be more clearly understood from Figure 5.42, where the engine operating points, over the RDE_7, are plotted on its BSFC map. The operating points are represented by means of circle markers whose size is proportional to the time spent by the engine in that region. By analyzing Figure 5.42a, it is evident that, when the power split is decided by the RB strategy, the ICE is operated in a wider area; instead, when the power split is decided by one of the strategies adopting the ECMS computation, the ICE is mainly operated in a region closer to the Optimal Operating Line (OOL), and the operating points at the lowest BMEP values are avoided. The robustness of the A-V2X-ECMS can be confirmed by Figure 5.42d: the power split chosen by this strategy is similar to the optimal ECMS one. The proposed strategy can obtain performance similar to the case in which all the mission profile is a priori known.

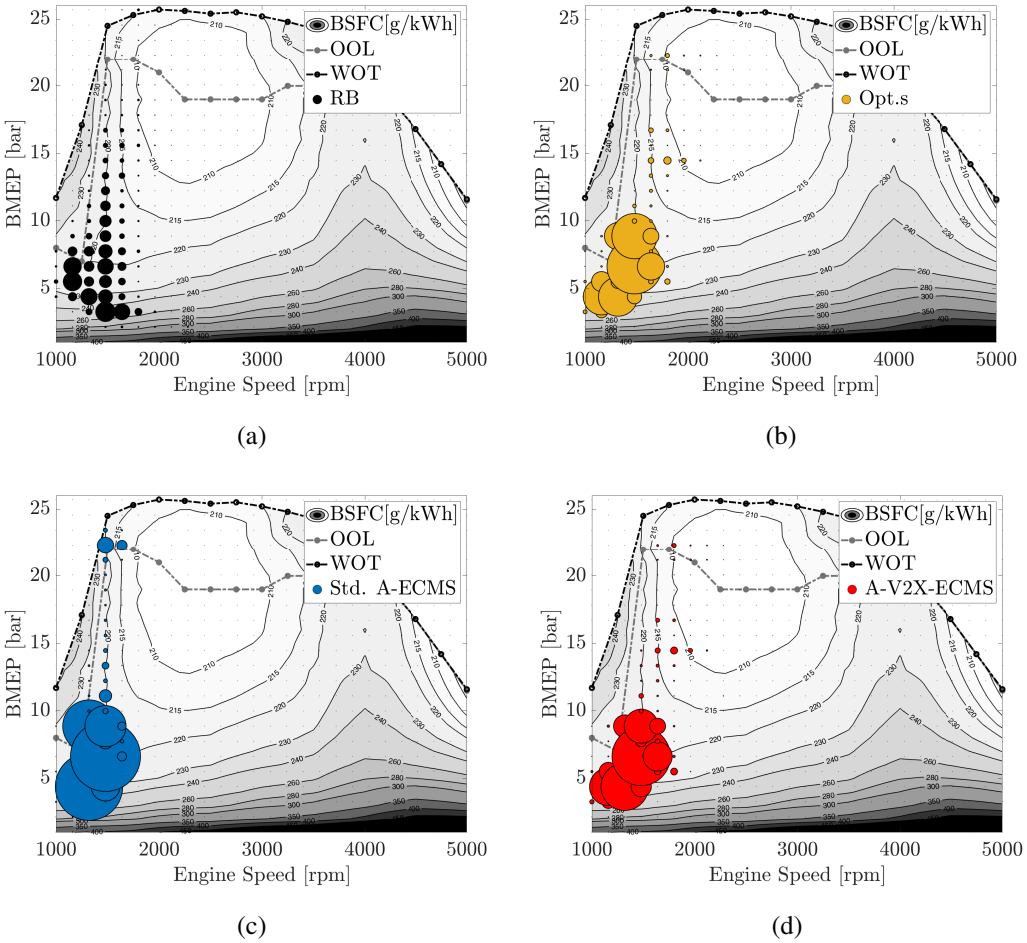

Fig. 5.42 Comparison of the ICE operating points over the RDE_7 cycle reported on the BSFC map – (a): RB – (b): ECMS optimized for CS conditions – (c): Standard A-ECMS – (d): A-VX-ECMS.

Chapter 6

Case Study 2: Battery SoH

An accurate estimation of the State of Health (SoH) of a LIB may provide valuable insights that can be used by the BMS to enforce safe operating bounds and enable health-conscious control strategies. This particularly rings true for BEVs, where the battery SoH strongly affects the available driving range but plays a pivotal role also in the energy management of HEVs and pHEVs since battery aging affects energy efficiency. Thus, if available, battery SoH indicators could also be included in the cost function of the EMS in order to penalize actions that could undermine battery health. However, monitoring battery health in the field through the signals tracked by the BMS such as current, voltage, and temperature is a multifaceted challenge and remains an open research conundrum.

In this framework, this Chapter analyzes the battery pack data collected from a real operating BEV in order to define Performance Indicators (PI), that are linked to health and can be extracted and monitored from real-time vehicle operation. Figure 6.1 depicts the flowchart of the procedure carried out. It should be noted that the set of presented PIs can be easily extended to assess the health of the battery of a pHEV, like the first case study (see Chapter 5).

The work presented in this Chapter is part of a project, sponsored by Volkswagen Group of America (VWoA) on which I worked while I was a visiting student at Stanford University, and is described more in detail in [162]. Moreover, three U.S. patents application have been filed featuring these techniques [163–165]. The structure of the Chapter is summarized below:

- In Section 6.1, the case study is described, giving particular emphasis to the battery topology and hierarchy;

- In Section 6.2, the data and the pre-processing pipeline are described: the signals are grouped in a structured way to reduce dimensionality, and to create the basis for analysis and data-driven model development;
- In Section 6.3, a new set of PIs is obtained, showing how these indicators are intricately related to the operating conditions, namely the battery temperature;
- In Section 6.4 some additional comments are made on the PIs highlighting the major contributions of this work.

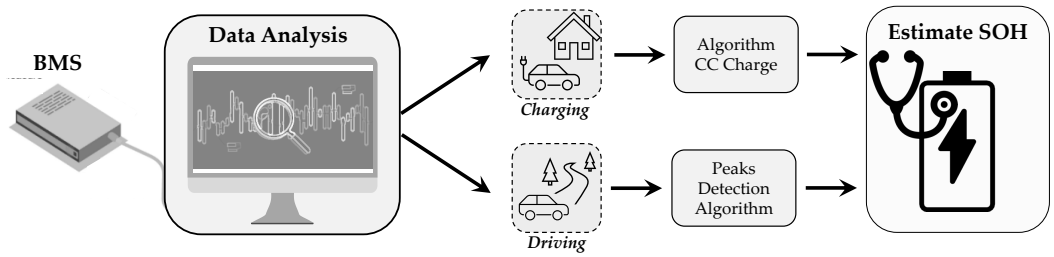

Fig. 6.1 Flowchart of the procedure carried out: data collected from a real operating BEV is analyzed in order to define Performance Indicators (PI) that can be correlated to health.

6.1 Test Case

The vehicle used in this work is an Audi e-tron, a state-of-the-art mid-size electric SUV, powered by a 95 kWh Li-ion battery pack. The battery pack has a nominal voltage of 396 V and a total capacity of 240 Ah. As shown in Figure 6.2, the battery contains 36 modules connected in series, each comprising 12 lithium-ion pouch cells with 4p3s topology and a rated capacity of 60 Ah.

The BMS has a primary-secondary architecture and each module is equipped with three voltage sensors, i.e., $v_{m,1}, v_{m,2}, v_{m,3}$, that measure the voltage across each group of four cells in parallel, and two temperature sensors. i.e., $t_{m,1}, t_{m,2}$, that measure the temperature at the module level. The BMS and the components within utilize the CAN bus to serially communicate the measured signals and control variables among each other, and to communicate with various other relevant electronic control units in the vehicle.

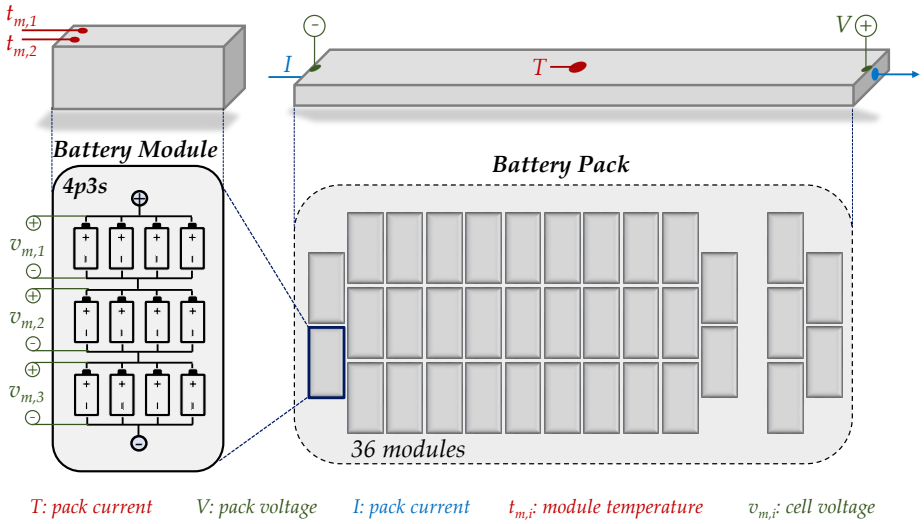

Fig. 6.2 Schematic of the battery pack containing 36 modules connected in series, each comprising 12 lithium-ion pouch cells with 4p3s topology. The available current, voltage, and temperature sensors are shown.

6.2 Data

In this work, BMS data from daily driving of the Audi e-tron are used and analyzed. As shown in Figure 6.3, the vehicle was driven in the San Francisco Bay Area, CA, from November 2019 to October 2020. The gap in the data between February and May 2020 is due to COVID-19 restrictions, that did not allow any testing of the vehicle. The logged data lasts approximately 3750 hours, and the percentage of charging, driving, and idle time, i.e., the time in which the vehicle is parked and the battery is not charged, is shown in Figure 6.4. It should be noted how idle time constitutes more than 90% of the total percentage: this suggests that, during normal operation of BEVs, the importance of calendar aging should not be undervalued.

The dataset used in this work consists of 2 TB of data. The BMS transmits 1655 signals, but the exact composition is proprietary: the signals include voltage, current, temperature, SoC, and other categorical information necessary for safe and reliable battery operation. A pre-processing pipeline was applied in order to clean, re-sample, and group the signals in a structured way to reduce dimensionality. By using the Sherlock high-performance computing cluster at Stanford University [141], the cardinality of the dataset was compressed from 2 TB to 22.1 GB. The MAT-files obtained as a result of the pre-processing pipeline were then used to perform the following analysis.

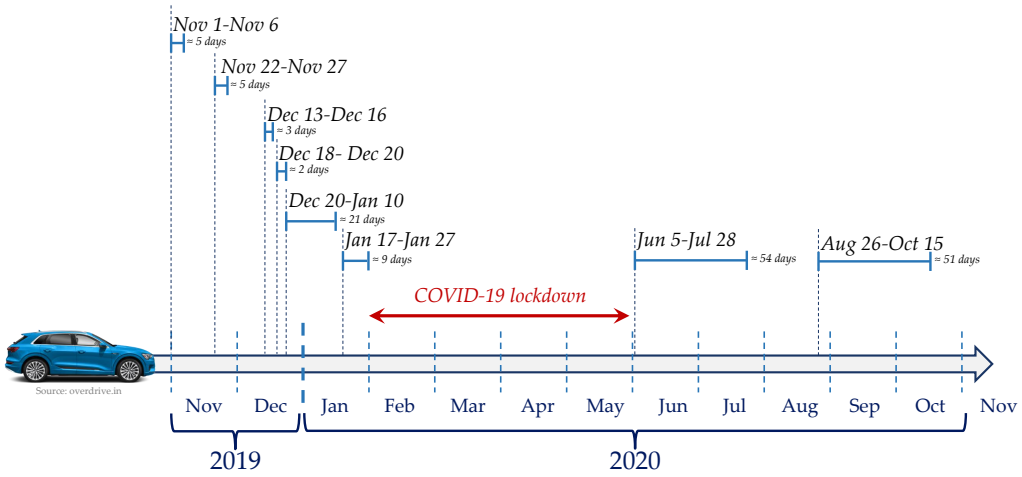

Fig. 6.3 Data from driving the vehicle from November 2019 to October 2020. The gap in the data between February and May 2020 is due to COVID-19 restrictions, that did not allow any testing of the vehicle.

6.3 Performance Indicators

In this Section, a set of Performance Indicators (PIs) that can be easily extracted from real-world driving events (i.e., braking and acceleration) and charging conditions are presented, and their dependency on temperature and time is shown.

6.3.1 High-Frequency Resistance

Abrupt changes in the battery pack current (herein referred to as "current peaks") can be considered as close as possible to a pulse. This study proposes a procedure to compute the battery's high-frequency resistance during the vehicle's braking and acceleration phases, similarly to the HPPC test (see Section 2.2.4). The voltage response curve corresponding to the change in current can be measured and used to compute the high-frequency resistance as:

$$R = -\frac{V(t_2) - V(t_1)}{I(t_2) - I(t_1)} = -\frac{\Delta V}{\Delta I} \tag{6.1}$$

where $V(t_1)$ and $I(t_1)$ are the voltage and current values at the beginning of the pulse, while $V(t_2)$ and $I(t_2)$ at the end of it. However, differently from the HPPC test, acceleration and braking events do not have standardized pulses, since they strongly depend on the driver, i.e., how strongly he pushes the pedals, and the braking and

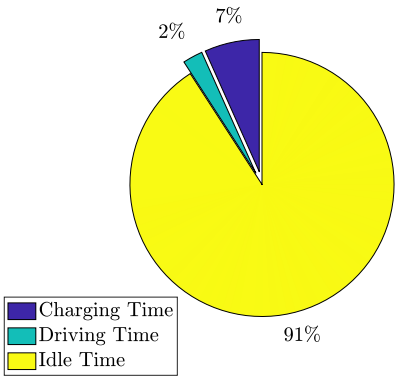

Fig. 6.4 Percentage of charging, driving, and idle time, i.e., the time in which the vehicle is parked and the battery is not charged, in the database used for this work.

acceleration events must be sufficiently short to avoid heat generation and/or change of SoC. For these reasons, in order to obtain reproducible and consistent results, the following algorithm was developed:

$$\begin{cases} a) & -thr < I_1 < thr \\ b) & \begin{cases} Acc: \ I >= 0 \\ Br: \ \ I <= 0 \end{cases} \quad \forall \quad t \in [t_1, t_2] \\ c) & \begin{cases} Acc: \ (\frac{dI}{dt})_f >= 0 \\ Br: \ \ (\frac{dI}{dt})_f <= 0 \end{cases} \quad \forall \quad t \in [t_1, t_2] \\ d) & \mid I_2 - I_1 \mid > \Delta A \\ e) & (t_2 - t_1) = \Delta t \end{cases} \tag{6.2}$$

The algorithm for the peak detection is composed of the set of conditions written in Equation (6.2). A peak is detected if it features an increase (or decrease) of current of at least ΔA - Condition (d) of Equation (6.2) - lasting Δt - Condition (e). Moreover, the absolute value of I_1 (the current at the beginning of the peak) must be smaller than the threshold thr - Condition (a) - and the current should never

change sign during the peak, i.e., always positive or negative for acceleration and braking events, respectively - Condition (b). Finally, to capture the phases in which the current is consistently increasing or decreasing, the derivative of the current must never change sign during the peak - Condition (c). To avoid being affected by the noise present in the current signal, the derivative of the current is filtered by means of a moving average on a window of 100s. The parameters of the algorithm were optimized in order to detect a congruous number of peaks that are as much as possible consistent among themselves. The following set of parameters was used:

$$\begin{cases} a) & \begin{cases} Acc: & thr = 5\ [A] \\ Br: & thr = 2\ [A] \end{cases} \\ d) & \Delta A = 100\ [A] \\ e) & \Delta t = 1\ [s] \end{cases} \tag{6.3}$$

The operation of the peaks detection algorithm is explained in Figure 6.5, where it has been applied on a small dataset (approximately 1 hour). All the peaks detected during the acceleration phases are highlighted in blue, while the ones detected during braking are in red. The zoom below illustrates more in detail the detection of a peak during a braking phase. In the current profile, the sequence of values that respect the algorithm conditions is shown in red. The peak lasts 1s, and the corresponding voltage values are shown in light blue.

Figure 6.6 shows two examples of peak detection during acceleration (a) and braking (b). Hereinafter, the resistance values computed during braking and acceleration events will be indicated with R_{BR} and R_{ACC}, respectively. Over the entire dataset, 392 R_{BR} values and 529 R_{ACC} values have been computed. Figure 6.7 shows all the resistance values computed over the entire dataset as a function of date and temperature, i.e., the date (in the form of epoch time) and battery temperature recorded by the BMS during the detected braking or acceleration event. The temperature, as it will be shown later, seems to affect the resistance values, while time seems to have a marginal effect on data collected over one year of EV operation.

Seasonality and temperature dependence for R_{BR} and R_{ACC} are shown in Figure 6.8. All values of R_{BR} and R_{ACC} are sorted into bins depending on temperature (buckets of 1 $[^{\circ}C]$) and date (buckets of individual months). The average value of all the resistances in a bucket was computed and plotted as a rhombus in Figure

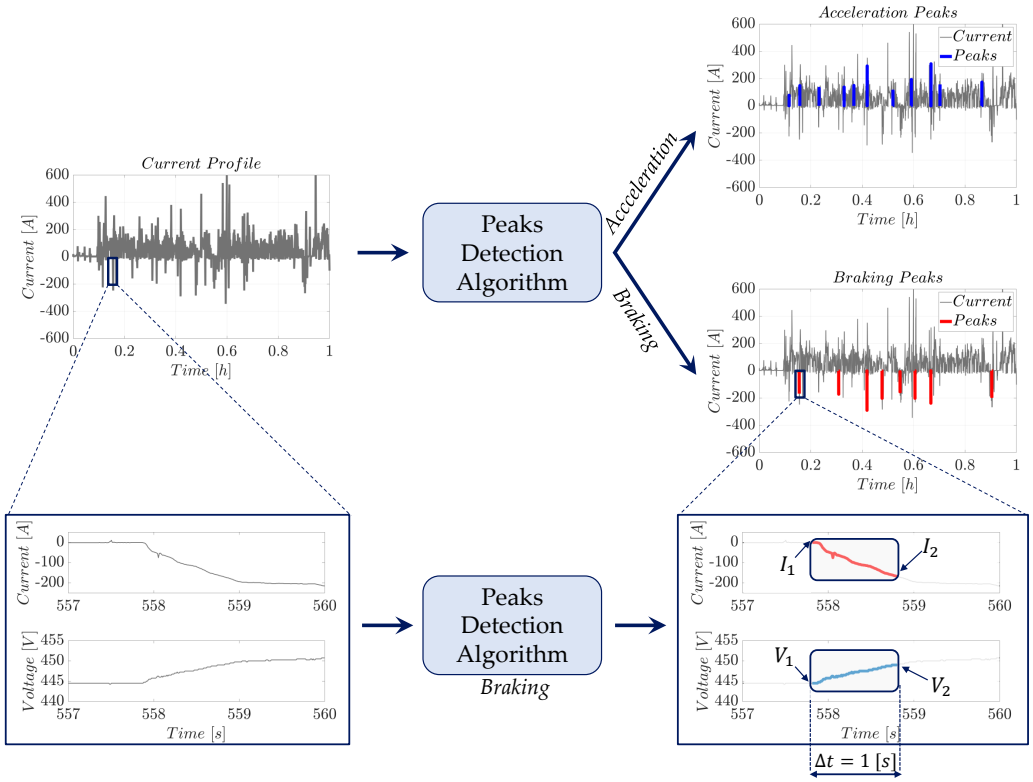

Fig. 6.5 Operation of the peaks detection algorithm: the peaks detected during the acceleration phases are highlighted in blue, and the ones detected during braking in red. The zoom below illustrates more in detail the detection of a peak during a braking phase.

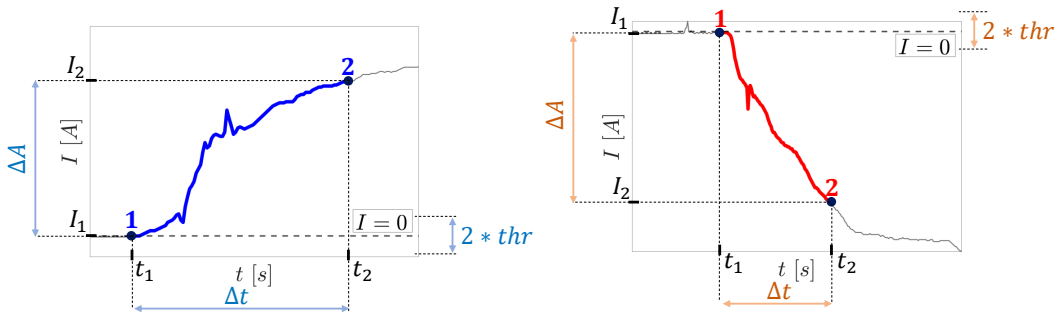

Fig. 6.6 (a): Example of a peak detected during an acceleration phase; (b): Example of a peak detected during a braking phase.

6.8. A negative correlation between high-frequency resistance and temperature can be observed across all months. Instead, no clear evidence of correlation can be detected between high-frequency resistance values and months. In fact, the lower high-frequency resistance values observed from June to September can be mainly attributed to the higher temperatures (no bins at lower temperatures). These results

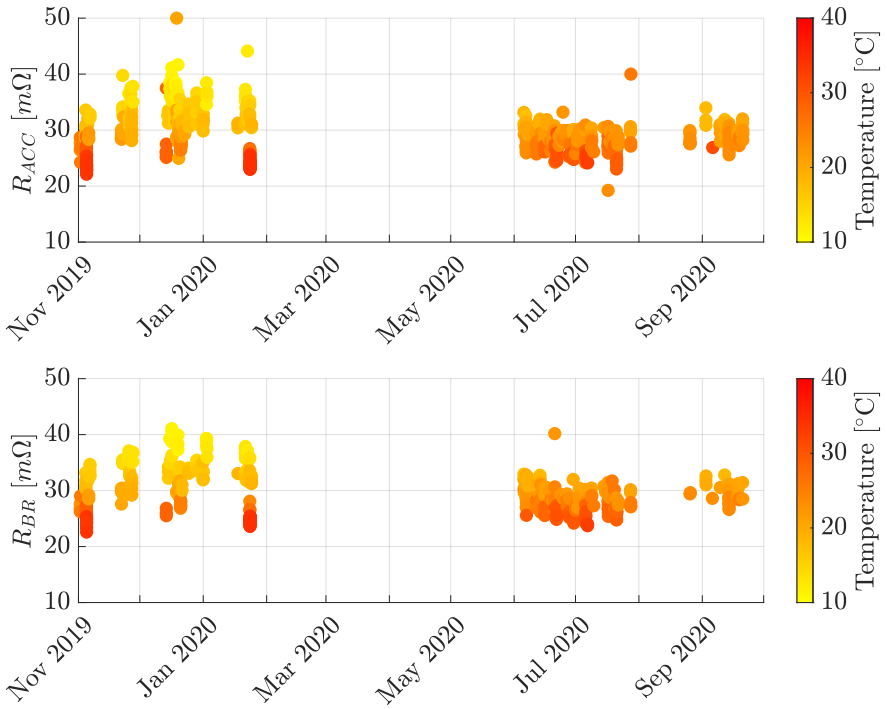

Fig. 6.7 High-frequency resistance computed during peaks in acceleration (above) and braking (below) events: the resistances are plotted as a function of date and pack temperature.

suggest that for the first year of EV operation, the temperature has a dominant effect on the high-frequency resistance and outwins time.

Figure 6.9 shows with more granularity the dependence of the high-frequency resistance on temperature. All the R_{BR} and R_{ACC} values are sorted into temperature buckets of 1 [$°C$]. The average value of all the resistances in a bucket is computed and plotted as a green rhombus (braking) or a red square (acceleration). R_{BR} and R_{ACC} have the same trend and are negatively correlated with temperature. This result is supported by the fact that, at lower temperatures, the transport processes are slower and the overpotential is higher, resulting in higher values of the high-frequency resistance. Moreover, the good overlapping of the R_{BR} and R_{ACC} values seems to corroborate the procedure developed for peak detection and high-frequency resistance computation.

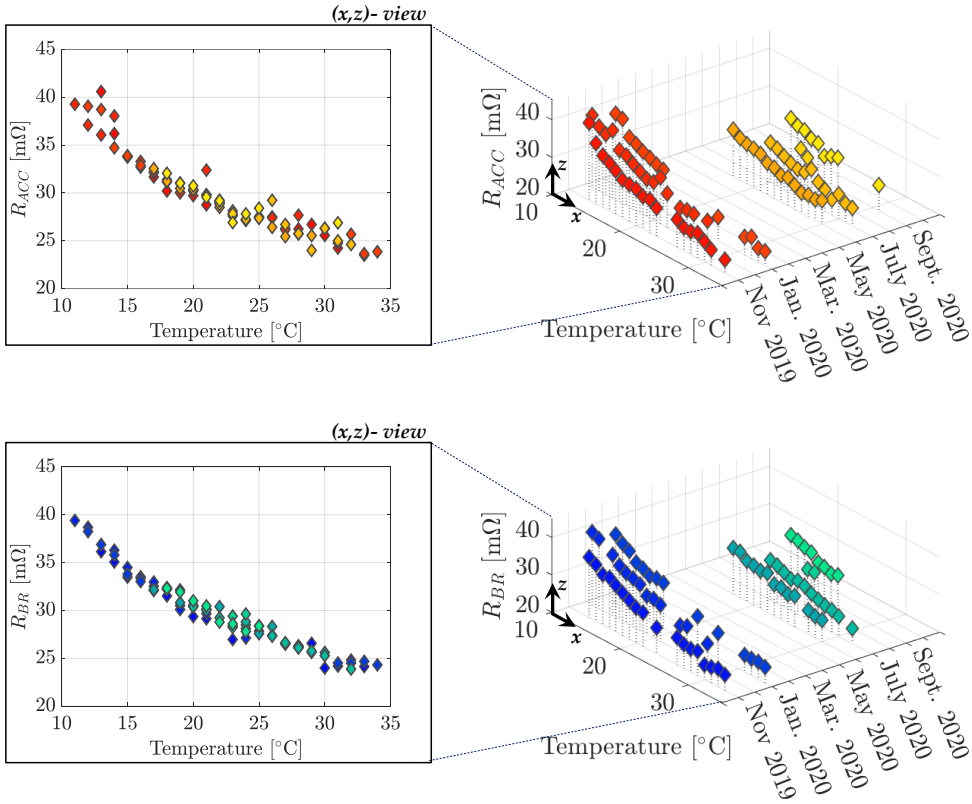

Fig. 6.8 High-frequency resistance in acceleration (on the top right) and braking (in the bottom right) as a function of time and pack temperature. On the left-hand side plots, the high-frequency resistance is shown to be negatively correlated with the pack temperature.

6.3.2 Charging Impedance

While current profiles during driving are based on decisions made by the user, battery charging operations are standardized. During charging events, the battery current is constant and is used in this work to compute the battery charging impedance as the change in voltage due to the applied constant current over a predefined time window Δt. The charging data is divided into 53 charging events by making the following assumptions: a profile is considered as a single charging event if it is separated from the previous and next charging events by at least 2 minutes. Moreover, if the average current is almost null, the charging event is discarded. As shown in Figure 6.10, the resulting charging events are divided into three different sets as a function of the C-rate: C/240, C/20, and C/2.

The charging impedance is introduced as a method to investigate the aging phenomena and capacity fade of the battery pack during charging events at a constant

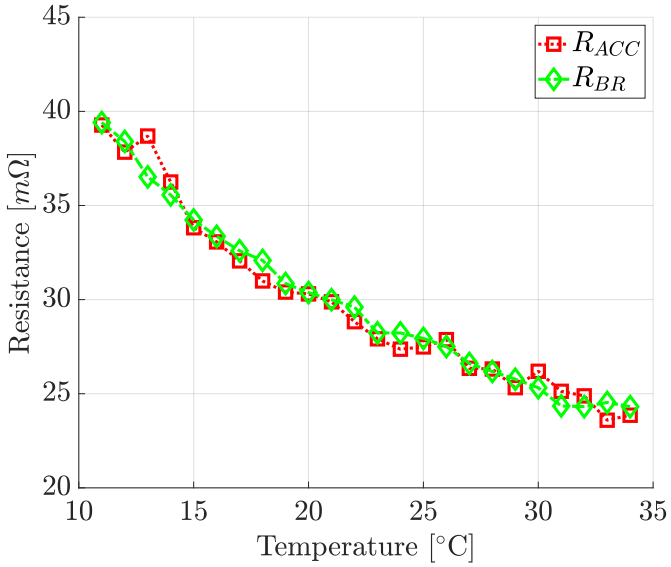

Fig. 6.9 High-frequency resistance plotted as a function of temperature: all the values are sorted into buckets of 1 [°C] and then averaged. A clear correlation between the resistance computed during acceleration and braking can be seen.

current. As shown in Figure 6.11, the charging impedance, measured in ohm, is computed by taking the ratio between the voltage difference and the applied current:

$$Z_{CHG} = -\frac{V(t_2) - V(t_1)}{I} = -\frac{\Delta V}{I} \tag{6.4}$$

where V is the battery pack voltage during charge measured at the time instants (carefully tuned by the user), t_1 and t_2, and the voltage difference ΔV is computed as the difference between $V(t_2)$ and $V(t_1)$. According to our convention, the current is negative during charge: the minus sign is used to ensure that $Z_{CHG} >= 0$.

The charging impedance curves depend on the C-rate. On the basis of a sensitivity analysis (not mentioned here for the sake of brevity), the C/20 charge events were chosen to compute the charging impedance, and a time window of $\Delta t = 100s$ was used. Moreover, the initial section of each charging profile (almost 1 hour) was discarded since the voltage profile features a different slope. Figure 6.12 shows the charging impedance profiles for all the C/20 charge events (after filtering via a moving average filter tuned at 500s to further reduce the noise).

The impedance variation over consecutive charging events can be remapped in the modifications of peaks and valleys in the Z_{CHG}-SoC plane. Notably, focusing

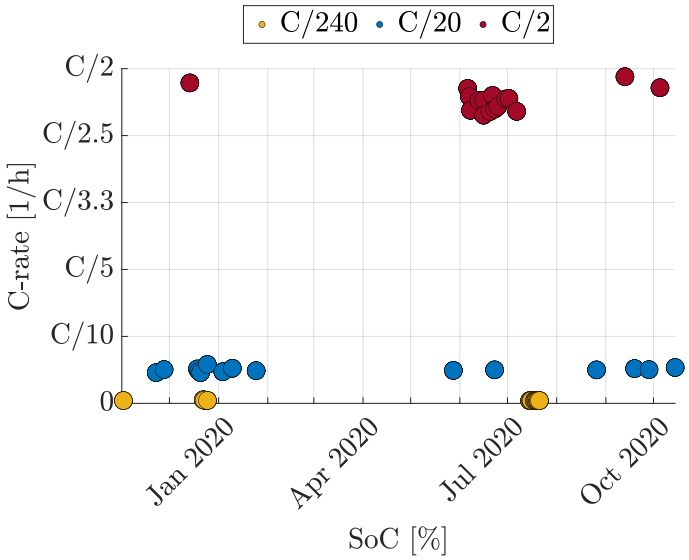

Fig. 6.10 The average charging rate used during the one-year period of data acquisition: C/240, C/20, and C/2.

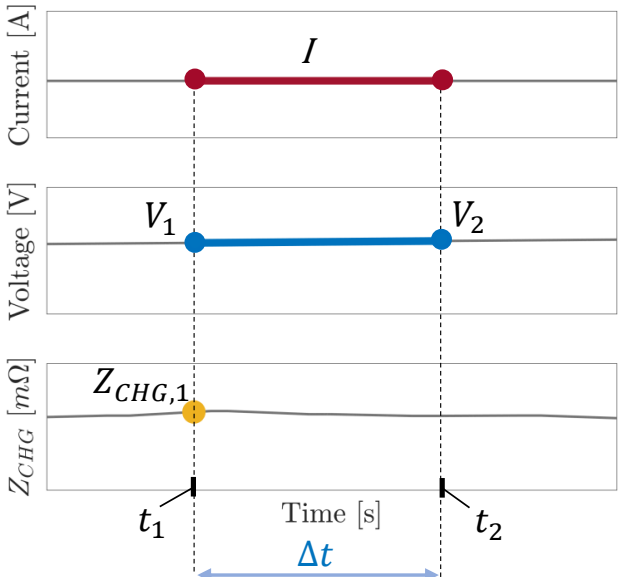

Fig. 6.11 Example of charging impedance computed during a charging event performed at constant current: it is computed by taking the ratio between the voltage difference and the applied current.

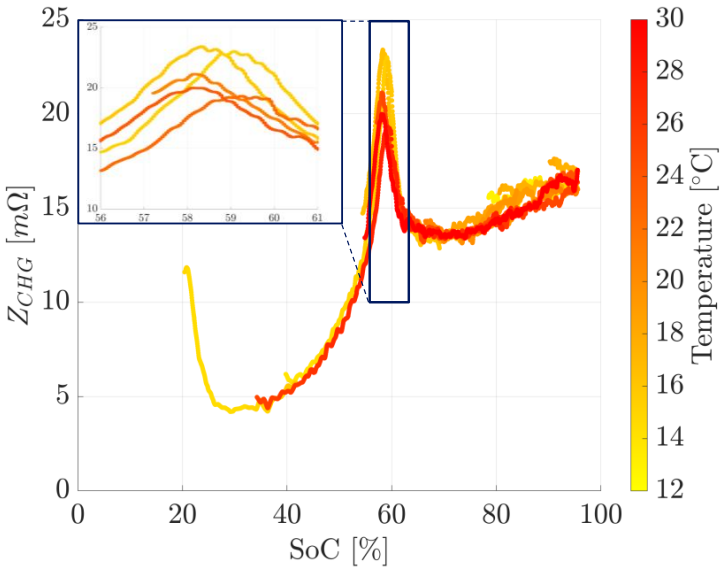

Fig. 6.12 Battery impedance plotted for all the charging events at C/20 as a function of SoC and temperature: curves are obtained considering $\Delta t = 100s$ and by filtering the signals obtained from Equation 6.4 via a moving average filter tuned at 500s. The black box shows a zoom in the SoC window 56-61%

on the SoC region between 50 and 60% (black box in Figure 6.12), it can be seen that the pack impedance peak is sensitive to temperature and decreases with it. The tracking of impedance peaks and valleys over time has striking similarities with DV and IC analyses (see Section 2.2.3). The following mathematical link between charging impedance and the DV curve can be provided:

$$Z_{CHG} = \frac{\Delta V}{\Delta Q}\Delta t = DV_{pack}\Delta t \tag{6.5}$$

where Δt represents a scaling factor. Since DV curves are generally defined at half-cell or full-cell level [44], when scaling up to pack-level, interconnection resistances must be taken into account [55]. In this framework, DV_{pack} blends information from the interconnected cells constituting the battery pack. This link provides a physical interpretation of the impedance curve and could enable its use as an on-board performance indicator of the battery pack.

6.4 Discussion

Section 6.3 developed tools to extract key information on battery pack performance using data collected from the BMS of an EV. The peak detection algorithm, to compute the high-frequency resistance during braking and acceleration events, and the impedance, computed during charging, rely on simple mathematical operations, which are computationally inexpensive and easily implementable on a BMS. These indicators have general applicability across chemistries and applications (EVs, fleets, grid storage, portable electronics, etc.), as they rely on measurements already available on-board during field operation.

The results showed in Section 6.3 reveal how convoluted time and temperature are when it comes to quantifying battery performance and degradation from field data. Unexpectedly, data collected over one year of EV operation shows that temperature has a dominant effect on PIs and outwins time. The coupling between battery performance and temperature makes the definition of reliable indicators challenging and, since current SoH algorithms are not developed to account for this convoluted behavior, it could also aggravate heterogeneities within the pack. The PIs proposed in this work – intrinsically accounting for temperature and time – could be used to decouple these effects, for example, by analyzing charging impedance profiles computed only at one specific temperature and tracking modifications of peaks and valleys over time. Finally, these indicators could be linked to capacity and power fade and used as features for ML models to complement current BMS strategies.

Chapter 7

Conclusions and Future Work

The demanding CO_2 targets are pushing the development of cost-effective solutions to improve powertrain efficiency. In this context, Electrified Vehicles (xEVs) represent a valuable solution to improve efficiency and reduce pollutant emissions of the current vehicle fleet. Among the xEVs, Hybrid Electric Vehicles (HEVs) and plug-in Hybrid Electric Vehicles (pHEVs) have been identified as key players since they can combine the desired features of an electric and a conventional powertrain. Nevertheless, they feature greater complexity, and an additional level, namely the Energy Management System (EMS), must be added to the vehicle control hierarchy to optimize the energy flows in the powertrain. Numerical simulation can play a significant role in the development of models for the investigation of different control strategies. Moreover, to obtain compelling and affordable xEVs featuring Li-ion batteries, an accurate State of Health (SoH) estimation is needed to characterize battery faults and update the Battery Management System (BMSs) algorithms. In parallel with the electrification trend, the growing connectivity level of the last-generation vehicles, as well as the exploitation of Artificial Intelligence (AI) techniques in the energy management of xEVs, have proved to be capable of effectively enhancing safety, traffic efficiency, and energy savings of the actual vehicle fleets.

In this framework, it is fundamental to develop multidisciplinary techniques and algorithms that can assess the increased opportunities for energy-efficient driving with the deployment of connected and electrified vehicles. This dissertation constitutes a feasibility study on some innovative methodologies that can support the design of these types of vehicles. In particular, Chapter 5 proposed some innovative methodologies for the energy management of HEVs that have been tested on a virtual test rig of a real case study. The data gathered from an extensive experimental cam-

paign performed on a commercially available pHEV were used to reverse engineer its control strategy and build a vehicle digital twin without having direct access to its EMS. After validating the virtual test rig against the experimental data, it was used to assess the theoretical benefits that the introduction of V2X communication can have in terms of energy and time savings in a real-world route. The vehicle digital twin was later used to assess the potentialities of an advanced energy management strategy that can exploit V2X information. Chapter 6 presented the second case study: BMS data from daily driving of an e-SUV were analyzed in order to define an innovative set of Performance Indicators (PIs), that are linked to battery health and can be easily extracted from real-world driving and charging events. The presented PIs, which can be linked to capacity and power fade, rely on simple mathematical operations, which are computationally inexpensive and easily implementable on a BMS. Therefore, they could also be adopted in the EMS of an HEV, like the first case study, in order to take into account also battery aging in the cost function and penalize the actions that could undermine battery health.

Future work will be aimed at achieving the targets discussed here below:

- The development of an integrated framework, exploiting a remote cloud computing environment, that can further enhance the fuel economy of an HEV over a given driving route through a synergistic optimization of both velocity profile and power split between the power actuators;
- Implementing real-time V2V and V2I information with the cloud-based optimization to recalculate the optimal velocity profile in real time in response to external traffic disturbances;
- Enhancing the energy management of the pHEV, presented in Chapter 5, by incorporating the defined PIs in its EMS in order to develop a comprehensive strategy that can take into account also battery aging.

Acknowledgements

At the end of this exciting experience, I feel obliged to express my heartfelt gratitude to the people who have supported me during these years. First of all, I would like to thank my supervisors, Prof. Federico Millo and Luciano Rolando: I feel extremely privileged to have collaborated with them since they were able to transmit to me part of their passion and boundless knowledge in this field. Then, I would like to thank Prof. Simona Onori for giving me the opportunity to join her lab at Stanford University. It has been a marvelous experience where I met bright students, researchers, and so many friends! I must thank my parents and brother for the tremendous support provided throughout the years. A special thanks also goes to my godmother Giorgia, and "American" mom Suzanne. They have always played important roles in my life. Then, I would like to say thanks to all my friends (now scattered all over the world) for their presence in my life, especially important when one lives far away from home. Finally, I want to thank Claudia, my girlfriend, whom I met by chance at Stanford but has already become so important in my life.

Appendix A

List of Publications and Patents

A.1 Publications

Year 2023

1. Pozzato, G., Allam, A., Pulvirenti, L., Negoita, A., Paxton, W., Onori, S., Analysis and key findings from real-world electric vehicle field data, Joule, 2023, https://doi.org/10.1016/j.joule.2023.07.018.

2. Pulvirenti, L., Rolando, L., Millo, F., Energy management system optimization based on an LSTM deep learning model using vehicle speed prediction, Transportation Engineering, 2023, https://doi.org/10.1016/j.treng.2023.100160.

3. Millo, F., Rolando L., Tresca, L., Pulvirenti, L., Development of a neural network-based energy management system for a plug-in hybrid electric vehicle, Transportation Engineering, 2023, https://doi.org/10.1016/j.treng.2022.100156.

4. Pulvirenti, L., Tresca, L., Rolando, L., Millo, F., Eco-Driving Optimization Based on Variable Grid Dynamic Programming and Vehicle Connectivity in a Real-World Scenario, Energies, 16(10), 4121, 2023, https://doi.org/10.3390/en16104121.

5. Galvagno, E., Rolando, L., Pulvirenti, L., Zerbato, L., Tresca, L., Synergic use of hybrid electric vehicle platoon control and optimal energy management system for fuel economy, safety, and dynamic performance, 2023 accepted at Proceeding of IFToMM WC2023.

Year 2022

1. Millo, F., Rolando, L., Pulvirenti, L., Di Pierro, G., A Methodology for the Reverse Engineering of the Energy Management Strategy of a Plug-In Hybrid Electric Vehicle for Virtual Test Rig Development, SAE International Journal of Electrified Vehicles - 11(1), 2022, https://doi.org/10.4271/14-11-01-0009.

Year 2021

1. Pulvirenti, L., Rolando, L., Millo, F., Energy Management System Optimization Based on V2X Connectivity, 2021 FISITA World Congress Proceedings, https://doi.org/10.46720/F2020-ADM-087.

A.2 Patents

Year 2022

1. Allam, A., Negoita, A., Onori, S., Paxton, W., Pozzato, G., and Pulvirenti, L., Battery management system for determining a health of a power source based on a impedance indicator, 2022, Joint invention Stanford – Volkswagen Group of America, Inc. Patent application pending with USPTO.

2. Allam, A., Negoita, A., Onori, S., Paxton, W., Pozzato, G., and Pulvirenti, L., Battery management system for determining a health of a power source based on driving events, 2022, Joint invention Stanford – Volkswagen Group of America, Inc. Patent application pending with USPTO.

3. Allam, A., Negoita, A., Onori, S., Paxton, W., Pozzato, G., and Pulvirenti, L., Battery management system for determining a health of a power source based on charging events, 2022, Joint invention Stanford – Volkswagen Group of America, Inc. Patent application pending with USPTO.

References

[1] Christoph R Birkl, Matthew R Roberts, Euan McTurk, Peter G Bruce, and David A Howey. Degradation diagnostics for lithium ion cells. *Journal of Power Sources*, 341:373–386, 2017.

[2] Gino Paganelli, Thierry-Marie Guerra, Sebastien Delprat, Jean-Jacques Santin, M. Delhom, and E. Combes. Simulation and assessment of power control strategies for a parallel hybrid car. *Int. J. of Automobile Engineering*, 214:705–717, 07 2000.

[3] Atriya Biswas and Ali Emadi. Energy management systems for electrified powertrains: State-of-the-art review and future trends. *IEEE Transactions on Vehicular Technology*, 68(7):6453–6467, 2019.

[4] Peng Bai, Daniel A Cogswell, and Martin Z Bazant. Suppression of phase separation in lifepo4 nanoparticles during battery discharge. *Nano letters*, 11(11):4890–4896, 2011.

[5] 2015 UNECE: Geneva, Switzerland. Unece global technical regulation no. 15 worldwide harmonized light vehicles test procedure. https://tinyurl.com/859eyr6c.

[6] UNECE. European green deal: commission proposes transformation of eu economy and society to meet climate ambitions," accessed october 2021. https://ec.europa.eu/commission/presscorner/detail/en/IP_21_3541., 2021, online documentation.

[7] IEA. Largest end uses of energy by sector in selected iea countries, 2019. https://www.iea.org/data-and-statistics/charts/largest-end-uses-of-energy-by-sector-in-selected-iea-countries-2019., 2022, online documentation.

[8] ACEA. Electric vehicles: tax benefits and purchase incentives. https://www.acea.auto/files/Electric_vehicles-Tax_benefits_purchase_incentives_European_Union_2020.pdf., 2021, online documentation.

[9] EEA. New registrations of electric vehicles in europe. hhttps://www.eea.europa.eu/ims/new-registrations-of-electric-vehicles., 2022, online documentation.

[10] IEA. Global electric car sales have continued their strong growth in 2022 after breaking records last year. https://rb.gy/3wf5c., 2022, online documentation.

[11] Lars-Henrik Björnsson and Sten Karlsson. Electrification of the two-car household: Phev or bev? *Transportation Research Part C: Emerging Technologies*, 85:363–376, 2017.

[12] Antonio Sciarretta and Lino Guzzella. Control of hybrid electric vehicles. *IEEE Control Systems Magazine*, pages 60–70, April 2007.

[13] Dai-Duong Tran, Majid Vafaeipour, Mohamed El Baghdadi, Ricardo Barrero, Joeri Van Mierlo, and Omar Hegazy. Thorough state-of-the-art analysis of electric and hybrid vehicle powertrains: Topologies and integrated energy management strategies. *Renewable and Sustainable Energy Reviews*, 119:109596, 2020.

[14] Fengqi Zhang, Lihua Wang, Serdar Coskun, Hui Pang, Yahui Cui, and Junqiang Xi. Energy management strategies for hybrid electric vehicles: Review, classification, comparison, and outlook. *Energies*, 13(13):3352, 2020.

[15] Sam Jaffe. Vulnerable links in the lithium-ion battery supply chain. *Joule*, 1(2):225–228, 2017.

[16] Anqi Zeng, Wu Chen, Kasper Dalgas Rasmussen, Xuehong Zhu, Maren Lundhaug, Daniel B Müller, Juan Tan, Jakob K Keiding, Litao Liu, Tao Dai, et al. Battery technology and recycling alone will not save the electric mobility transition from future cobalt shortages. *Nature communications*, 13(1):1–11, 2022.

[17] Antti Porvali, Miamari Aaltonen, Severi Ojanen, Omar Velazquez-Martinez, Emmi Eronen, Fupeng Liu, Benjamin P Wilson, Rodrigo Serna-Guerrero, and Mari Lundström. Mechanical and hydrometallurgical processes in hcl media for the recycling of valuable metals from li-ion battery waste. *Resources, Conservation and Recycling*, 142:257–266, 2019.

[18] European Commission. Directive (eu) 2010/40/eu of the european parliament and of the council of 7 july 2010 on the framework for the deployment of intelligent transport systems in the field of road transport and for interfaces with other modes of transport text with eea relevance. http://data.europa.eu/eli/dir/2010/40/oj.

[19] Alkis Papadoulis, Mohammed Quddus, and Marianna Imprialou. Evaluating the safety impact of connected and autonomous vehicles on motorways. *Accident Analysis & Prevention*, 124:12–22, 2019.

[20] Qiang Lu and Kyoung-Dae Kim. Autonomous and connected intersection crossing traffic management using discrete-time occupancies trajectory. *Applied Intelligence*, 49:1621–1635, 2019.

[21] Pete Olin, Karim Aggoune, Li Tang, Keith Confer, John Kirwan, Shreshta Rajakumar Deshpande, Shobhit Gupta, Punit Tulpule, Marcello Canova, and Giorgio Rizzoni. Reducing fuel consumption by using information from connected and automated vehicle modules to optimize propulsion system control. In *SAE Technical Paper 2019-01-1213*, page 15, 04 2019.

[22] Yang Zhou, Alexandre Ravey, and Marie-Cécile Péra. A survey on driving prediction techniques for predictive energy management of plug-in hybrid electric vehicles. *Journal of Power Sources*, 412:480–495, 2019.

[23] Peter Arthurs, Lee Gillam, Paul Krause, Ning Wang, Kaushik Halder, and Alexandros Mouzakitis. A taxonomy and survey of edge cloud computing for intelligent transportation systems and connected vehicles. *IEEE Transactions on Intelligent Transportation Systems*, 23(7):6206–6221, 2022.

[24] Shreshta Rajakumar Deshpande, Shobhit Gupta, Abhishek Gupta, and Marcello Canova. Real-time ecodriving control in electrified connected and autonomous vehicles using approximate dynamic programing. *Journal of Dynamic Systems, Measurement, and Control*, 144(1):011111, 2022.

[25] Forbes. What is the artificial intelligence revolution and why does it matter to your business? https://shorturl.at/qvxSY., 2022, online documentation.

[26] Kristen A Severson, Peter M Attia, Norman Jin, Nicholas Perkins, Benben Jiang, Zi Yang, Michael H Chen, Muratahan Aykol, Patrick K Herring, Dimitrios Fraggedakis, et al. Data-driven prediction of battery cycle life before capacity degradation. *Nature Energy*, 4(5):383–391, 2019.

[27] Muratahan Aykol, Chirranjeevi Balaji Gopal, Abraham Anapolsky, Patrick K Herring, Bruis van Vlijmen, Marc D Berliner, Martin Z Bazant, Richard D Braatz, William C Chueh, and Brian D Storey. Perspective—combining physics and machine learning to predict battery lifetime. *Journal of The Electrochemical Society*, 168(3):030525, 2021.

[28] Tristan Burton, Scott Powers, Cooper Burns, Graham Conway, Felix Leach, and Kelly Senecal. A data-driven greenhouse gas emission rate analysis for vehicle comparisons. *SAE International Journal of Electrified Vehicles*, 12(1), 2023.

[29] John B. Goodenough. The nobel prize in chemistry 2019. https://www.nobelprize.org/prizes/chemistry/2019/summary/. Accessed: 2022-02-07.

[30] John B. Goodenough and Kyu-Sung Park. The li-ion rechargeable battery: A perspective. *Journal of the American Chemical Society*, 135(4):1167–1176, 2013.

[31] Harikesh Arunachalam. *A New Multiscale Modeling Framework for Lithium-Ion Battery Dynamics: Theory, Experiments, and Comparative Study with the Doyle-Fuller-Newman Model*. PhD thesis, Clemson University, 2017.

[32] Jorn Reniers. *Degradation-aware optimal control of grid-connected lithium-ion batteries*. PhD thesis, University of Oxford, 2019.

[33] Gregory L. Plett. *Battery Management Systems*. Number v. 1 in Artech House power engineering and power electronics. Artech House, 2015.

[34] Peter G. Bruce. Energy storage beyond the horizon: Rechargeable lithium batteries. *Solid State Ionics*, 179(21):752–760, 2008. Solid State Ionics 16: Proceedings of the 16th International Conference on Solid State Ionics (SSI-16), Part I.

[35] Kirby W Beard. *Linden's handbook of batteries*. McGraw-Hill Education, 2019.

[36] Christian M Julien, Alain Mauger, Karim Zaghib, and Henri Groult. Comparative issues of cathode materials for li-ion batteries. *Inorganics*, 2(1):132–154, 2014.

[37] Maxwell D Radin, Sunny Hy, Mahsa Sina, Chengcheng Fang, Haodong Liu, Julija Vinckeviciute, Minghao Zhang, M Stanley Whittingham, Y Shirley Meng, and Anton Van der Ven. Narrowing the gap between theoretical and practical capacities in li-ion layered oxide cathode materials. *Advanced Energy Materials*, 7(20):1602888, 2017.

[38] Ephrem Chemali, Matthias Preindl, Pawel Malysz, and Ali Emadi. Electrochemical and electrostatic energy storage and management systems for electric drive vehicles: State-of-the-art review and future trends. *IEEE Journal of Emerging and Selected Topics in Power Electronics*, 4(3):1117–1134, 2016.

[39] Xiaosong Hu, Fei Feng, Kailong Liu, Lei Zhang, Jiale Xie, and Bo Liu. State estimation for advanced battery management: Key challenges and future trends. *Renewable and Sustainable Energy Reviews*, 114:109334, 2019.

[40] Ester Vasta, Alberto Lucifora, Luigi Danilo Tornello, Salvatore Foti, Mario Cacciato, Christian Pernaci, Salvatore De Caro, and Giacomo Scelba. State of charge estimation of battery energy storage systems in low voltage electric drive applications for hybrid and electric vehicles. In *2022 IEEE Energy Conversion Congress and Exposition (ECCE)*, pages 1–7. IEEE, 2022.

[41] Kotub Uddin, Surak Perera, W Dhammika Widanage, Limhi Somerville, and James Marco. Characterising lithium-ion battery degradation through the identification and tracking of electrochemical battery model parameters. *Batteries*, 2(2):13, 2016.

[42] Matthieu Dubarry, Arnaud Devie, and Bor Yann Liaw. The value of battery diagnostics and prognostics. *J. Energy Power Sources*, 1(5):242 – 249, 2014.

[43] Christopher Hendricks, Nick Williard, Sony Mathew, and Michael Pecht. A failure modes, mechanisms, and effects analysis (fmmea) of lithium-ion batteries. *Journal of Power Sources*, 297:113–120, 2015.

[44] Matthieu Dubarry, Cyril Truchot, and Bor Yann Liaw. Synthesize battery degradation modes via a diagnostic and prognostic model. *Journal of Power Sources*, 219:204–216, 2012.

[45] Jens Vetter, Petr Novák, Markus Robert Wagner, Claudia Veit, K-C Möller, JO Besenhard, Martin Winter, Margret Wohlfahrt-Mehrens, Christoph Vogler, and Abderrezak Hammouche. Ageing mechanisms in lithium-ion batteries. *Journal of power sources*, 147(1-2):269–281, 2005.

[46] C Pastor-Fernández, WD Widanage, Gael Chouchelamane, and James Marco. A soh diagnosis and prognosis method to identify and quantify degradation modes in li-ion batteries using the ic/dv technique. In *6th Hybrid and Electric Vehicles Conference (HEVC 2016)*, pages 1–6. IET, 2016.

[47] David Anseán, Víctor Manuel García, Manuela González, Cecilio Blanco-Viejo, Juan Carlos Viera, Yoana Fernández Pulido, and Luciano Sánchez. Lithium-ion battery degradation indicators via incremental capacity analysis. *IEEE Transactions on Industry Applications*, 55(3):2992–3002, 2019.

[48] Uwe Tröltzsch, Olfa Kanoun, and Hans-Rolf Tränkler. Characterizing aging effects of lithium ion batteries by impedance spectroscopy. *Electrochimica acta*, 51(8-9):1664–1672, 2006.

[49] Yu Merla, Billy Wu, Vladimir Yufit, Nigel P Brandon, Ricardo F Martinez-Botas, and Gregory J Offer. Novel application of differential thermal voltammetry as an in-depth state-of-health diagnosis method for lithium-ion batteries. *Journal of Power Sources*, 307:308–319, 2016.

[50] E Sarasketa-Zabala, Frederic Aguesse, Igor Villarreal, LM Rodriguez-Martinez, Carmen M López, and Pierre Kubiak. Understanding lithium inventory loss and sudden performance fade in cylindrical cells during cycling with deep-discharge steps. *The Journal of Physical Chemistry C*, 119(2):896–906, 2015.

[51] Jeff Dahn. Phase diagram of lic6. *Phys. Rev. B*, 44:9170–9177, Nov 1991.

[52] Martin Winter, Juergen Otto Prof Dr Besenhard, Michael E. Spahr, and Petr Novák. Insertion electrode materials for rechargeable lithium batteries. *Advanced Materials*, 10:725–763, 1998.

[53] Anup Barai, Kotub Uddin, Matthieu Dubarry, Limhi Somerville, Andrew McGordon, Paul Jennings, and Ira Bloom. A comparison of methodologies for the non-invasive characterisation of commercial li-ion cells. *Progress in Energy and Combustion Science*, 72:1–31, 2019.

[54] Carlos Pastor-Fernández, Kotub Uddin, Gael Chouchelamane, W.D. Widanage, and James Marco. A comparison between electrochemical impedance spectroscopy and incremental capacity-differential voltage as li-ion diagnostic techniques to identify and quantify the effects of degradation modes within battery management systems. *Journal of Power Sources*, 360:301–318, 08 2017.

[55] Theodoros Kalogiannis, Daniel Ioan Stroe, Jonas Nyborg, Kjeld Nørregaard, Andreas Elkjær Christensen, and Erik Schaltz. Incremental capacity analysis of a lithium-ion battery pack for different charging rates. *ECS Transactions*, 77(11):403, 2017.

[56] Valentin Sulzer, Peyman Mohtat, Antti Aitio, Suhak Lee, Yen T Yeh, Frank Steinbacher, Muhammad Umer Khan, Jang Woo Lee, Jason B Siegel, Anna G Stefanopoulou, et al. The challenge and opportunity of battery lifetime prediction from field data. *Joule*, 5(8):1934–1955, 2021.

[57] Jon P Christophersen. Battery test manual for electric vehicles, revision 3. Technical report, Idaho National Lab.(INL), Idaho Falls, ID (United States), 2015.

[58] Gabriele Pozzato, Anirudh Allam, and Simona Onori. Lithium-ion battery aging dataset based on electric vehicle real-driving profiles. *Data in Brief*, 41:107995, 2022.

[59] Nils J. Nilsson. *The Quest for Artificial Intelligence*. Cambridge University Press, 2009.

[60] Arthur L. Samuel. Some studies in machine learning using the game of checkers. *IBM Journal on Research and Development*, 3(3):210–229, 1959.

[61] Susmita Ray. A quick review of machine learning algorithms. In *2019 International Conference on Machine Learning, Big Data, Cloud and Parallel Computing (COMITCon)*, pages 35–39, 2019.

[62] Diksha Sharma and Neeraj Kumar. A review on machine learning algorithms, tasks and applications. *International Journal of Advanced Research in Computer Engineering & Technology (IJARCET)*, 6(10):2278–1323, 2017.

[63] Ajay Shrestha and Ausif Mahmood. Review of deep learning algorithms and architectures. *IEEE Access*, PP:1–1, 04 2019.

[64] Zhihang Chen, Yonggang Liu, Yuanjian Zhang, Zhenzhen Lei, Zheng Chen, and Guang Li. A neural network-based ecms for optimized energy management of plug-in hybrid electric vehicles. *Energy*, 243:122727, 2022.

[65] Zeyi Wei and Yahui Zhang. A real-time energy management strategy of hevs based on velocity prediction. In *2021 60th Annual Conference of the Society of Instrument and Control Engineers of Japan (SICE)*, pages 490–494, 2021.

[66] Mike Haußmann, Daniel Barroso, Carlos Vidal, Lucas Bruck, and Ali Emadi. A novel multi-mode adaptive energy consumption minimization strategy for p1-p2 hybrid electric vehicle architectures. In *2019 IEEE Transportation Electrification Conference and Expo (ITEC)*, pages 1–6, 2019.

[67] Frank Rosenblatt. The perceptron: a probabilistic model for information storage and organization in the brain. *Psychological review*, 65 6:386–408, 1958.

[68] Michael A Nielsen. *Neural networks and deep learning*, volume 25. Determination press San Francisco, CA, USA, 2015.

[69] Paul Werbos. *Beyond Regression: New Tools for Prediction and Analysis in the Behavioral Science*. PhD thesis, Appl. Math. Harvard University, 01 1974.

[70] Yann LeCun, Y. Bengio, and Geoffrey Hinton. Deep learning. *Nature*, 521:436–44, 05 2015.

[71] Yong Yu, Xiaosheng Si, Changhua Hu, and Jianxun Zhang. A review of recurrent neural networks: Lstm cells and network architectures. *Neural Computation*, 31(7):1235–1270, 2019.

[72] Sepp Hochreiter and Jürgen Schmidhuber. Long short-term memory. *Neural computation*, 9:1735–80, 12 1997.

[73] Juan A. Pérez-Ortiz, A. Gers, Felix, Douglas Eck, and Juergen Schmidhuber. Kalman filters improve lstm network performance in problems unsolvable by traditional recurrent nets. *Neural Networks*, 16(2):241–250, 2003.

[74] Yaoran Chen, Yan Wang, Zhikun Dong, Jie Su, Zhaolong Han, Dai Zhou, Yongsheng Zhao, and Yan Bao. 2-d regional short-term wind speed forecast based on cnn-lstm deep learning model. *Energy Conversion and Management*, 244:114451, 2021.

[75] A. Gers, Felix, Juergen Schmidhuber, and F. Cummins. Learning to forget: continual prediction with lstm. In *1999 Ninth International Conference on Artificial Neural Networks ICANN 99. (Conf. Publ. No. 470)*, volume 2, pages 850–855 vol.2, 1999.

[76] John Harding, Gregory H. Powell, Rebecca Yoon, Joshua Fikentscher, Charlene T Doyle, Dana Sade, Mike Lukuc, Jim Simons, and Jing Wang. Vehicle-to-vehicle communications: Readiness of v2v technology for application. In *Report No. DOT HS 812 014*. Washington, DC: National Highway Traffic Safety Administration, 2014.

[77] Slash Gear. The 2020 vw golf 8 could make smart cars mass-market. https://www.slashgear.com/2020-volkswagen-golf-8-car2x-v2v-smart-cars-mass-market-25597350/. Accessed: 2022-02-07.

[78] John Kenney. Dedicated short-range communications (dsrc) standards in the united states. *Proceedings of the IEEE*, 99:1162 – 1182, 08 2011.

[79] Xingqin Lin, Jeffrey G. Andrews, Amitabha Ghosh, and Rapeepat Ratasuk. An overview of 3gpp device-to-device proximity services. *IEEE Communications Magazine*, 52(4):40–48, 2014.

[80] Mario H. Castañeda Garcia, Alejandro Molina-Galan, Mate Boban, Javier Gozalvez, Baldomero Coll-Perales, Taylan Şahin, and Apostolos Kousaridas. A tutorial on 5g nr v2x communications. *IEEE Communications Surveys & Tutorials*, 23(3):1972–2026, 2021.

[81] Carlos Renato Storck and Fatima Duarte-Figueiredo. A survey of 5g technology evolution, standards, and infrastructure associated with vehicle-to-everything communications by internet of vehicles. *IEEE Access*, 8:117593–117614, 2020.

[82] Keyvan Ansari. Joint use of dsrc and c-v2x for v2x communications in the 5.9 ghz its band. *IET Intelligent Transport Systems*, 2020.

[83] Bassel Othman, Giovanni De Nunzio, Antonio Sciarretta, Domenico Di Domenico, and Carlos Canudas-De-Wit. *Handbook of Climate Change Mitigation and Adaptation*, pages 2337–2376. Springer New York, 03 2021.

[84] Russell Dicker. 3 new ways to navigate more sustainably with maps. https://blog.google/products/maps/3-new-ways-navigate-more-sustainably-maps/. Accessed: 2022-02-07.

[85] Shobhit Gupta, Daliang Shen, Dominik Karbowski, and Aymeric Rousseau. Koopman model predictive control for eco-driving of automated vehicles. In *2022 American Control Conference (ACC)*, pages 2443–2448. IEEE, 2022.

[86] Zhaoxuan Zhu, Nicola Pivaro, Shobhit Gupta, Abhishek Gupta, and Marcello Canova. Safe model-based off-policy reinforcement learning for eco-driving in connected and automated hybrid electric vehicles. *IEEE Transactions on Intelligent Vehicles*, 7(2):387–398, 2022.

[87] Qiangqiang Guo, Ohay Angah, Zhijun Liu, and Xuegang Jeff Ban. Hybrid deep reinforcement learning based eco-driving for low-level connected and automated vehicles along signalized corridors. *Transportation Research Part C: Emerging Technologies*, 124:102980, 2021.

[88] Lorenzo Serrao. *A comparative analysis of energy management strategies for hybrid electric vehicles*. PhD thesis, Ohio State University, 2009.

[89] Luciano Rolando. *An Innovative Methodology for the Development of HEVs Energy Management System*. PhD thesis, Politecnico di Torino, 2012.

[90] Dimitri Bertsekas. *Dynamic Programming and Optimal Control*. Athena Scientific, Belmont, MA, 1995.

[91] Bram De Jager, Thijs Van Keulen, and John Kessels. *Optimal control of hybrid vehicles*. Springer, 2013.

[92] Valerie Johnson, Keith Wipke, and David Rausen. Hev control strategy for real-time optimization of fuel economy and emissions. In *SAE Technical Paper 2000-01-1543*, 04 2000.

[93] Yuan Zhu, Yaobin Chen, Guangyu Tian, Hao Wu, and Quanshi Chen. A four-step method to design an energy management strategy for hybrid vehicles. In *Chinese Journal of Mechanical Engineering - CHIN J MECH ENG*, volume 1, pages 156 – 161 vol.1, 08 2004.

[94] Richard Bellman. *Dynamic Programming*. Dover Publications, 1957.

[95] H. Kaufman. The mathematical theory of optimal processes, by l. s. pontryagin, v. g. boltyanskii, r. v. gamkrelidze, and e. f. mishchenko. authorized translation from the russian. translator: K. n. trirogoff, editor: L.. w. neustadt. interscience publishers (division of john wiley and sons, inc., new york) 1962. viii 360 pages. *Canadian Mathematical Bulletin*, 7(3):500–500, 1964.

[96] Basil Kouvaritakis and Mark Cannon. *Model Predictive Control: Classical, Robust and Stochastic*. Springer, 01 2016.

[97] Johannes Van Der Wal. *Stochastic dynamic programming*. PhD thesis, Methematisch Centrum Amsterdam, The Netherlands, 1980.

[98] Theo Hofman, Maarten Steinbuch, Roell Van Druten, and Alex Serrarens. Rule-based energy management strategies for hybrid vehicle drivetrains: a fundamental approach in reducing computation time. *IFAC Proceedings Volumes*, 39(16):740–745, 2006. 4th IFAC Symposium on Mechatronic Systems.

[99] Philipp Valentin Elbert, Soeren Ebbesen, and Lino Guzzella. Implementation of dynamic programming for n-dimensional optimal control problems with final state constraints. *IEEE Transactions on Control Systems Technology*, 21, 2013-05.

[100] A. Brahma, Yann Guezennec, and Giorgio Rizzoni. Optimal energy management in series hybrid electric vehicles. In *American Control Conference, 2000. Proceedings of the 2000*, volume 1, pages 60 – 64 vol.1, 10 2000.

[101] Ilya A Kulikov, Elena E Baulina, and Andrey I Filonov. Optimal control of a hybrid vehicle's powertrain minimizing pollutant emissions and fuel consumption. In *SAE Technical Paper 2014-09-30*, page 4, 2014.

[102] Federico Millo, Luciano Rolando, Fabio Mallamo, and Rocco Fuso. Development of an optimal strategy for the energy management of a range-extended electric vehicle with additional noise, vibration and harshness constraints. *Proceedings of the Institution of Mechanical Engineers, Part D: Journal of Automobile Engineering*, 227(1):4–16, 2013.

[103] Chan-Chiao Lin, Jun-Mo Kang, J.W. Grizzle, and Huei Peng. Energy management strategy for a parallel hybrid electric truck. In *Proceedings of the 2001 American Control Conference. (Cat. No.01CH37148)*, volume 4, pages 2878–2883 vol.4, 2001.

[104] Domenico Bianchi, Luciano Rolando, Lorenzo Serrao, Simona Onori, Giorgio Rizzoni, Nazar Al-Khayat, Tung-Ming Hsieh, and Pengju Kang. Layered control strategies for hybrid electric vehicles based on optimal control. *International Journal of Electric and Hybrid Vehicles*, 3(2):191–217, 2011.

[105] Theo Hofman, Maarten Steinbuch, Roell Van Druten, and Alex Serrarens. Rule-based energy management strategies for hybrid vehicles. *International Journal of Electric and Hybrid Vehicles*, 1(1):71–94, 2007.

[106] Hans Geering. *Optima Control with Engineering Applications*. Springer, Berlin, 01 2007.

[107] Gino Paganelli. *Conception et commande d'une chaîne de traction pour véhicule hybride parallèle thermique et électrique*. Université de Valenciennes et du Hainaut Cambrésis, 1999.

[108] Luca Pulvirenti. *Development of an Equivalent Consumption Minimization Strategy (ECMS) for a High-Performance Hybrid Electric Vehicle*. PhD thesis, Politecnico di Torino, 2019.

[109] Lorenzo Serrao, Simona Onori, and Giorgio Rizzoni. Ecms as a realization of pontryagin's minimum principle for hev control. In *2009 American Control Conference*, pages 3964–3969, 2009.

[110] Cristian Musardo, Giorgio Rizzoni, Yann Guezennec, and Benedetto Staccia. A-ECMS: An adaptive algorithm for hybrid electric vehicle energy management. *European Journal of Control*, 11(4-5):509–524, 2005.

[111] Pierluigi Pisu and Giorgio Rizzoni. A comparative study of supervisory control strategies for hybrid electric vehicles. *Control Systems Technology, IEEE Transactions on*, 15(3):506–518, 2007.

[112] Fengqi Zhang, Junqiang Xi, and Reza Langari. Real-time energy management strategy based on velocity forecasts using v2v and v2i communications. *IEEE Transactions on Intelligent Transportation Systems*, 18(2):416–430, 2017.

[113] Simona Onori, Lorenzo Serrao, and Giorgio Rizzoni. Adaptive equivalent consumption minimization strategy for hybrid electric vehicles. In *Dynamic systems and control conference*, volume 44175, pages 499–505, 2010.

[114] N. Jalil, NA Kheir, and Mutasim Salman. A rule-based energy management strategy for a series hybrid vehicle. *Proceedings of the 1997 American Control Conference*, 1, 1997.

[115] Mutasim Salman, NJ Schouten, and NA Kheir. Control strategies for parallel hybrid vehicles. *Proceedings of the 2000 American Control Conference.*, 1(6):524–528, 2000.

[116] Chan-Chiao Lin, Huei Peng, JW Grizzle, and Jun-Mo Kang. Power management strategy for a parallel hybrid electric truck. *IEEE Transactions on Control Systems Technology*, 11(6):839–849, 2003.

[117] Antonio Sciarretta, Michael Back, and Lino Guzzella. Optimal control of parallel hybrid electric vehicles. *IEEE Transactions on Control Systems Technology*, 12(3):352–363, 2004.

[118] Domenico Bianchi, Luciano Rolando, Lorenzo Serrao, Simona Onori, Giorgio Rizzoni, Nazhar Al-Khayat, Tung-Ming Hsieh, and Pengju Kang. A rule-based strategies for a series-parallel hybrid electric vehicle: an approach based on dynamic programming. *Proceedings of The ASME Dynamic Systems and Control Conference, Cambridge, Massachusetts*, September 2010.

[119] Bin Xu, Dhruvang Rathod, Darui Zhang, Adamu Yebi, Xueyu Zhang, Xiaoya Li, and Zoran Filipi. Parametric study on reinforcement learning optimized energy management strategy for a hybrid electric vehicle. *Applied Energy*, 259:114200, 2020.

[120] Vinith Kumar Lakshmanan, Shobhit Gupta, Stefano D'Alessandro, Matteo Spano, Dennis Kibalama, Stephanie Stockar, Marcello Canova, Ouafae El Ganaoui-Mourlan, and Antonio Sciarretta. Predicting lead vehicle velocity for eco-driving in the absence of v2v information. Technical report, SAE Technical Paper, 2023.

[121] Shobhit Gupta, Shreshta Rajakumar Deshpande, Daniela Tufano, Marcello Canova, Giorgio Rizzoni, Karim Aggoune, Pete Olin, and John Kirwan. Estimation of fuel economy on real-world routes for next-generation connected and automated hybrid powertrains. In *SAE Technical Paper 2019-01-1213*, 04 2020.

[122] Lorenzo Brunelli, Alessandro Capancioni, Pierpaolo Gonnella, Rebecca Casadio, Alessandro Brusa, Nicolò Cavina, and Michele Caggiano. A hybrid vehicle hardware-in-the-loop system with integrated connectivity for ehorizon functions validation. *IEEE Transactions on Vehicular Technology*, 70(5):4340–4352, 2021.

[123] Lorenzo Brunelli, Alessandro Capancioni, Stella Canè, Giammarco Cecchini, Alessandro Perazzo, Alessandro Brusa, and Nicolò Cavina. A predictive control strategy based on a-ecms to handle zero-emission zones: Performance assessment and testing using an hil equipped with vehicular connectivity. *Applied Energy*, 340:121008, 2023.

[124] Lorenzo Serrao, Simona Onori, Antonio Sciarretta, Yann Guezennec, and Giorgio Rizzoni. Optimal energy management of hybrid electric vehicles including battery aging. In *Proceedings of the 2011 American control conference*, pages 2125–2130. IEEE, 2011.

[125] Gabriele Pozzato, Simone Formentin, Giulio Panzani, and Sergio M Savaresi. Least costly energy management for extended-range electric vehicles: An economic optimization framework. *European Journal of Control*, 56:218–230, 2020.

[126] Rui Xiong, Jiayi Cao, and Quanqing Yu. Reinforcement learning-based real-time power management for hybrid energy storage system in the plug-in hybrid electric vehicle. *Applied energy*, 211:538–548, 2018.

[127] Federico Millo, Luciano Rolando, and Maurizio Andreata. Numerical simulation for vehicle powertrain development. In Jan Awrejcewicz, editor, *Numerical Analysis*, chapter 24. IntechOpen, Rijeka, 2011.

[128] Arnulf Latz, Timo Danner, Birger Horstmann, and Thomas Jahnke. Microstructure- and theory-based modeling and simulation of batteries and fuel cells. *Chemie Ingenieur Technik*, 91, 04 2019.

[129] Marc Doyle, Thomas F. Fuller, and John Newman. Modeling of galvanostatic charge and discharge of the lithium/polymer/insertion cell. *Journal of The Electrochemical Society*, 140(6):1526, jun 1993.

[130] Harikesh Arunachalam, Simona Onori, and Ilenia Battiato. On veracity of macroscopic lithium-ion battery models. *Journal of The Electrochemical Society*, 162:1940–1951, 07 2015.

[131] Ernesto Martínez-Rosas, Ruben Vasquez-Medrano, and Antonio Flores-Tlacuahuac. Modeling and simulation of lithium-ion batteries. *Computers & Chemical Engineering*, 35(9):1937–1948, 2011.

[132] Anirudh Allam. *Holistic Battery Management System Design for Lithium-Ion Battery Systems via Physics-Based Modeling, Estimation, and Control*. PhD thesis, Stanford University, 2021.

[133] Gabriele Pozzato, Seong Beom Lee, and Simona Onori. Modeling degradation of lithium-ion batteries for second-life applications: preliminary results. In *2021 IEEE Conference on Control Technology and Applications (CCTA)*, pages 826–831, 2021.

[134] P Ramadass, Bala Haran, Parthasarathy M Gomadam, Ralph White, and Branko N Popov. Development of first principles capacity fade model for li-ion cells. *Journal of the Electrochemical Society*, 151(2):A196, 2004.

[135] Shriram Santhanagopalan, Qingzhi Guo, Premanand Ramadass, and Ralph E White. Review of models for predicting the cycling performance of lithium ion batteries. *Journal of power sources*, 156(2):620–628, 2006.

[136] Peter M Attia, Aditya Grover, Norman Jin, Kristen A Severson, Todor M Markov, Yang-Hung Liao, Michael H Chen, Bryan Cheong, Nicholas Perkins, Zi Yang, et al. Closed-loop optimization of fast-charging protocols for batteries with machine learning. *Nature*, 578(7795):397–402, 2020.

[137] Sheng Shen, Mohammadkazem Sadoughi, Meng Li, Zhengdao Wang, and Chao Hu. Deep convolutional neural networks with ensemble learning and transfer learning for capacity estimation of lithium-ion batteries. *Applied Energy*, 260:114296, 2020.

[138] Hicham Chaoui and Chinemerem Christopher Ibe-Ekeocha. State of charge and state of health estimation for lithium batteries using recurrent neural networks. *IEEE Transactions on vehicular technology*, 66(10):8773–8783, 2017.

[139] GAMMA TECHNOLOGY. *GT-Suite User Manuals*. GAMMA TECHNOLOGY.

[140] Olle Sundstrom and Lino Guzzella. A generic dynamic programming matlab function. In *2009 IEEE Control Applications, (CCA) & Intelligent Control, (ISIC)*, pages 1625–1630, 2009.

[141] Stanford university and sherlock hpc. https://www.sherlock.stanford.edu/.

[142] Federico Millo, Luciano Rolando, Luca Pulvirenti, and Giuseppe Di Pierro. A methodology for the reverse engineering of the energy management strategy of a plug-in hybrid electric vehicle for virtual test rig development. *SAE International Journal of Electrified Vehicles*, 11(14-11-01-0009):113–132, 2021.

[143] Luca Pulvirenti, Luigi Tresca, Luciano Rolando, and Federico Millo. Eco-driving optimization based on variable grid dynamic programming and vehicle connectivity in a real-world scenario. *Energies*, 16(10):4121, 2023.

[144] Federico Millo, Luciano Rolando, Luigi Tresca, and Luca Pulvirenti. Development of a neural network-based energy management system for a plug-in hybrid electric vehicle. *Transportation Engineering*, 11:100156, 2023.

[145] Luca Pulvirenti, Luciano Rolando, and Federico Millo. Energy management system optimization based on v2x connectivity. In *2021 FISITA World Congress Proceedings*, 2021.

[146] Luca Pulvirenti, Luciano Rolando, and Federico Millo. Energy management system optimization based on an lstm deep learning model using vehicle speed prediction. *Transportation Engineering*, 11:100160, 2023.

[147] Giuseppe DiPierro, Enrico Galvagno, Gianluca Mari, Federico Millo, Mauro Velardocchia, and Alessandro Perazzo. A reverse-engineering method for powertrain parameters characterization applied to a p2 plug-in hybrid electric vehicle with automatic transmission. *SAE International Journal of Advances and Current Practices in Mobility*, 3(2020-37-0021):715–730, 2020.

[148] 2015 UNECE: Geneva, Switzerland. 83–revision 5. uniform provisions concerning the approval of vehicles with regard to the emission of pollutants according to engine fuel requirements; unece: Geneva, switzerland, 2015. https://tinyurl.com/cxmdcdzy.

[149] European Commission. Commission regulation (eu) 2017/1151 of 1 june 2017 of the european parliament and of the council on type-approval of motor vehicles with respect to emissions from light passenger and commercial vehicles (euro 5 and euro 6) ... https://tinyurl.com/53ecjp7s.

[150] Media.daimler. Under the microscope: the intelligent operating strategy: Better electric performance. https://tinyurl.com/y37zrbn6.

[151] Gamma Technologies LLC. Vehicle driveline and hev application manual, 2021.

[152] Nassim A Samad, Jason B Siegel, and Anna G Stefanopoulou. Parameterization and validation of a distributed coupled electro-thermal model for prismatic cells. In *Dynamic systems and control conference*, volume 46193, page V002T23A006. American Society of Mechanical Engineers, 2014.

[153] Nassim A Samad, Youngki Kim, Jason B Siegel, and Anna G Stefanopoulou. Influence of battery downsizing and soc operating window on battery pack performance in a hybrid electric vehicle. In *2015 IEEE Vehicle Power and Propulsion Conference (VPPC)*, pages 1–6. IEEE, 2015.

[154] Janette Sadik-Khan. Urban street design guide. *New York: NACTO*, 2012.

[155] Philipp Elbert, Soren Ebbesen, and Lino Guzzella. Implementation of dynamic programming for n-dimensional optimal control problems with final state constraints. *IEEE Transactions on Control Systems Technology*, 21(3):924–931, 2013.

[156] EPA. Dynamometer drive schedules. https://www.epa.gov/vehicle-and-fuel-emissions-testing/dynamometer-drive-schedules.

[157] Report INRETS-LTE 0411. Institut national de recherche sur les transports et leur securite, “real-world driving cycles for measuring cars pollutant missions - part a: The artemis european driving cycles, 2004.

[158] DieselNet. Rts 95 cycle. https://dieselnet.com/standards/cycles/rts95.php.

[159] John A Hartigan, Manchek A Wong, et al. A k-means clustering algorithm. *Applied statistics*, 28(1):100–108, 1979.

[160] Hervé Abdi and Lynne J Williams. Principal component analysis. *Wiley interdisciplinary reviews: computational statistics*, 2(4):433–459, 2010.

[161] MATLAB. Experiment manager. https://it.mathworks.com/help/deeplearning/ref/experimentmanager-app.html, 2021b, online documentation.

[162] Gabriele Pozzato, Anirudh Allam, Luca Pulvirenti, Gianina Alina Negoita, William A Paxton, and Simona Onori. Analysis and key findings from real-world electric vehicle field data. *Joule*, 2023.

[163] Anirudh Allam, Alina Negoita, Simona Onori, William Paxton, Gabriele Pozzato, and Luca Pulvirenti. Battery management system for determining a health of a power source based on a impedance indicator. *Joint invention Stanford – Volkswagen Group of America, Inc. Patent application pending with USPTO*, 2022.

[164] Anirudh Allam, Alina Negoita, Simona Onori, William Paxton, Gabriele Pozzato, and Luca Pulvirenti. Battery management system for determining a health of a power source based on driving events. *Joint invention Stanford – Volkswagen Group of America, Inc. Patent application pending with USPTO*, 2022.

[165] Anirudh Allam, Alina Negoita, Simona Onori, William Paxton, Gabriele Pozzato, and Luca Pulvirenti. Battery management system for determining a health of a power source based on charging events. *Joint invention Stanford – Volkswagen Group of America, Inc. Patent application pending with USPTO*, 2022.